EFFECTS OF TWO-STEP ANNEALING ON COMPLEX PERMEABILITY OF Fe-Cu-Nb-Si-B NANOCRYSTALLINE SOFT MAGNETIC MATERIALS

BY
SAROAUT NOOR
ROLL NO. 0055506
SESSION: 2000-2001

ATHESIS SUBMITTED TO THE DEPERTMENT OF PHYSICS,
KHULNA UNIVERSITY OF ENGINEERING AND TECHNOLOGY
IN PARTIAL FULFILMENT OF THE REQUIRMENT FOR THE DEGREE OF
MASTER OF PHILOSOPY

DEPERTMENT OF PHYSICS
KHULNA UNIVERSITY OF ENGINEERING & TECHNOLOGY
KHULNA-920300, BANGLADESH

MARCH, 2005

KHULNA UNIVERSITY OF ENGINEERING & TECHNOLOGY
DEPARTMENT OF PHYSICS
CERTIFICATION OF THESIS WORK

A THESIS ON

Effects of two step annealing on Complex Permeability of Fe-Cu-Nb-Si-B Nanocrystalline Soft Magnetic Materials

By

SAROAUT NOOR

has been accepted as satisfactory in partial fulfillment for the degree of Master of Philosophy in Physics and certify that the student demonstrated a satisfactory knowledge on the field covered by this thesis in an oral examination held on 21 April, 2005.

Board of Examiners:

(1) Professor Dr. Shibendra Shekher Sikder
Department of Physics
Khulna University of Engineering & Technology
---------- Chairman.

(2) Head
Department of Physics
Khulna University of Engineering & Technology
---------- Member

(3) Dr. A. K. M. Abdul Hakim
Chief Engineer & Head
Magnetic Materials Division
Atomic Energy Centre
P.O. Box –164, Ramna, Dhaka-1000
---------- Co- supervisor

(4) Professor Dr. Md. Mahbub Alam
Department of Physics
Khulna University of Engineering & Technology
---------- Member

(5) Md. Abdullah Elias Akhter
Assistant Professor
Department of Physics
Khulna University of Engineering & Technology
---------- Member

(6) Professor Dr. Mominul Huq
Department of Physics
Bangladesh University of Engineering & Technology
Dhaka-1000
---------- Member (External)

CERTIFICATE

This is to certify that this thesis which the candidate has presented for M. Phil degree has been done by the candidate herself and does not contain any material extracted from elsewhere or from a work published by any body else. The work of this thesis has not been presented for another degree or diploma in any other University or Institute. No other person's work has been used without due acknowledgement.

Supervisor

Candidate

TO
MY LATE GRAND FATHER
AND
BELOVED PARENTS

Acknowledgement

I express with due respect my deep sense of sincere gratitude to my supervisor professor Dr. Shibendra Shekher Sikder, Head of the Department, Department of Physics, Khulna University of Engineering and Technology (KUET), for his continuous guidance, fruitful discussions, and encouragement for completion of this thesis work in time.

I am very much indebted to my Co-Supervisor Dr. A. K. M. Abdul Hakim, Chief Engineer, Magnetic Materials Division, AECD for his interest, excellent guidance and valuable assistance during the experimental work performed at the Magnetic Materials Division, Atomic Energy Centre, Dhaka. His rigorous expertise and intuition in experimental work and generous support has contributed substantially to the completion of the present work.

I am deeply grateful to Professor Dr. Md. Mahbub Alam, Department of Physics, Khulna University of Engineering and Technology (KUET), for his interest and encouragement in my thesis.

I would like to express my sincerest gratitude to Dr. D. K. Saha, P. S. O of MMD, AECD for his generous help in doing measurements and analysis of XRD results.

I am grateful to Dr. Abdul Gafur, S. O., BCSIR Laboratory, Dhaka for their generous help in doing the Differential Thermal Analysis.

I would like to extend my special thanks to Mr. A. K. M. Shamim, Associate Professor, Head of the Department, Department of Physics, Khulna Govt Mohila College, for his tireless co-operation in my thesis work.

I am thankful to Professor M. Aminul Islam, ProVice-Chancellor, National University for his helpful suggestions and inspiration.

My thanks are due to S. Manjura Hoque S. S. O of MMD, AECD, for providing me technical assistance time to time during my research work.

I gratefully acknowledge Jolly Sultana, Mr. Md. Abdullah Elias Akhter, Assistant Professor, Department of Physics in KUET, for their co-operation and inspiration during this work.

I am thankful to Alhamra Parvin, J. E. O. Anjumanara Begum, R. A. Arifa Sultana, SA-2. Rokeya Parvin, SA-2 of MMD, AECD for their constant help during my work.

I would like to thank Md. Mizanur Rahman, Mr. Zakir Hossen Khan, Khan Allal Uddin and Shaheena Parvin for their fruitful co-operation and assistance.

I am greatly indebted to my father, mother, brother and sisters for their consistent encouragement and inspiration.

My thanks are due to Director Atomic Energy Centre, Dhaka for his kind permission to use the Laboratory of Magnetic Material Division, Atomic Energy Center, Dhaka.

I also wish to thank the authority of Khulna University of Engineering and Technology (KUET), for providing me with the necessary permission and financial assistance for conducting this thesis work.

Abstract

The typical nanocrystalline alloy known as Finemet with the composition $Fe_{73.5}Cu_1Nb_3Si_{13.5}B_9$ has been studied for the soft magnetic properties. The crystalline phases that evolved after crystallization were studied by X-ray diffraction, crystallization temperature by DTA and magnetic properties by VSM and impedance analyzer. The change of magnetic properties with annealing temperature, T_a in the range 400-700°C and annealing time 1-60 minutes have been investigated. The effect of a two-step annealing on the permeability $Fe_{73.5}Cu_1Nb_3Si_{13.5}B_9$ alloy has been studied.

The grain size was determined from the line broadening of the fundamental peak using Scherrers method. Annealed at 555°C, the grain size, the solute silicon content of α-Fe(Si) grains and the improvement in magnetic softness saturate as a function of time. As compared to a nanocrystalline alloy obtained by conventional one-step annealing at around the crystallization temperature, the alloy subjected to preannealing at T_a = 400°C and subsequent high temperature annealing at T_a=555°C shows similar soft magnetic properties. An enhancement of initial permeability with increasing annealing temperature was observed until the annealing temperature T_a = 475°C and corresponds to the amorphous relaxed structure. An abrupt deteroriation of permeability takes place at the beginning of crystallzation beyond which permeability rises dramatically attaining a maximum value at T_a = 555°C which is attributed to the nanometri grain size effect as a result of averaging out of effective magnetic anisotropy by exchange interaction and decrease of magnetoelastic energy. A sharp decrease of permeability above 580°C is assumed to be connected with iron-boride phase at the beginning of second crystallization stage. The initial permeability for the optimum annealed sample has been found to be 20786 as compared with 284 for its amorphous counterpart. The behavior of very high permeability is explained on the basis of random anisotropy model. From the temperature dependence of magnetization the Curie temperature of the amorphous state and crystallized ferromagnetic phases like Fe(Si) and iron-boride phases and the onset of crystallization temperatures of these phases have been determined. Saturation magnetization measured on the amorphous and annealed samples at different annealing temperature gradually increases with T_a and show a maximum at the medium stage of nanocrysallization at T_a=525°C beyond which magnetization decreases. The results are interpreted on the basis of irreversible structural relaxation as well as enrichment of the nanograins with Si.

Table of Contents

Chapter-4 Experimental Details

Chapter-5 Results and Discussions

List of the figures

List of symbols

T_m	=	Melting temperature
T_g	=	Glass transition temperature
T_x	=	Crystallization temperature
λ	=	Wave length of the X-ray
[hkl]	=	Index of the peak
I	=	X-ray beam of intensity
μ_m	=	Mass absorption coefficient
μ_a	=	Absorption coefficient
TM	=	Transition melt
TM-M	=	Transition melt material
VSM	=	Vibrating Sample Magnetometer
DTA	=	Differential Thermal Analysis
XRD	=	X-ray Diffraction
FWHM	=	Full Width at Half Maximum
a_0	=	Lattice parameter
D_g	=	Grain size
b	=	Si(at.%)
μ'	=	Real part of the complex permeability
μ''	=	Imaginary part of the complex permeability
Q	=	Loss factor
$Q\mu'$	=	Relative quality factor
T_c	=	Curie temperature
M_s	=	Saturation magnetization

Chapter-1

Introduction

1.1 Introduction

The anocrystalline soft magnetic materials constitute a new class of condensed matter having interesting properties, which are mostly microstructure dependent. These materials are first formed into amorphous ribbons and then annealed above the crystallization temperature to form the nanocrystalline microstructure that consists of bcc Fe(Si) nanograins embedded on amorphous matrix. Excellent soft magnetic properties can be found in these nanocrystalline materials obtained by the controlled crystallization of Fe-Si-B amorphous ribbons containing 1 at.% Cu and 3 at.% Nb. The composition of these novel materials with the trade name Finemet is $Fe_{73.5}Cu_1Nb_3Si_{13.5}B_9$. The crystallization of bcc Fe(Si) solid solution from amorphous state takes place according to the basic scheme characteristic to the hypo-eutectic glasses [1.1]: $am_1 \rightarrow Fe(Si) + am_2$, where am_1 and am_2 are the initial amorphous precursor and the remainder amorphous phase respectively. Though this reaction takes place within few seconds as thermal effect, the excellent soft magnetic properties to evolve only gradually until the final volume fraction and the appropriate concentration and distribution of the components between the nanograins and the intergranular amorphous shell is reached. There are mainly two phases in the alloys with optimum magnetic properties: a bcc Fe-Si solid solution and some residual amorphous phase. The average grain size of the bcc Fe (Si) phase is about 10-12nm. The addition of Cu and Nb result in the formation of an ultrafine grain structure. The ultrafine grain structure of these alloys give rise to excellent soft magnetic properties that are superior to those of Co-based amorphous alloys. Soft magnetic properties of nanocrystalline alloys are strongly dependent on the grain size and grain boundary structure. The soft magnetic properties have been successfully addressed by the random anisotropy model by Herzer [1.2]. The magnetocrystalline anisotropy of the small randomly oriented grains are substantially reduced by exchange interaction due to the strong magnetic coupling among the nanograins.

Herzer explained the grain size dependence of the coercivity based on random anisotropy model considering the nanocrystalline materials as a single phase magnetic system. Hernando *et. al.* [1.3] extended this model for two phase materials and was able to explain the thermal dependence of the coercivity [1.4-1.6]. The early explanation of the soft

magnetic properties of these nanocrystalline alloys was based on the random anisotropy model and was established by Herzer[1.7]. It is related to the ratio of the exchange correlation length of the orientation fluctuation of randomly distributed local easy axes, or in other words, the ratio of the domain wall thickness to the mean crystallite size. This model explained the main feature of the dependence of coercivity on the grain size [1.8-1.9]. Recently experiments showed that magnetic hardening takes place at the very beginning of nanocrystallization [1.10-1.13] which falls out of the capabilities of Herzer's description.

Recently, a generalization of the random anisotropy model, taking into account the two phase character of nanocrystalline materials, has been developed [1.14] and it explains the previously mentioned hardening as well as other features which could not be understood without the generalization. Since the unique properties of nanostructured materials are dictated by the dimensions of the crystallites, it is very advantageous to control the size of the particles by controlling the annealing temperature of the specimens. The magnetic softness or hardness in respect of permeability is determined by the grain size, grain distribution and the volume fraction, which are developed on the amorphous matrix in the nanostructured system. The single domain permanent magnets, as theoretically proposed by Stoner and Wohlfarth [1.15], have no domain walls, because the wall energy increases as the square of the radius of the grains while the magnetic anisotropy energy increases as the cube of the radius. However, by reducing the size of the magnetic particles much below the critical size as defined by Stoner-Wahlfarth which is normally in the range extremely soft magnetic properties can be achieved.

Nanocrystalline materials differ between the one and the two phase model only at very low crystallized volume fraction or at temperature close to the Curie temperature of the amorphous phase. Thus, as a function of measuring temperature, a single sample combines a variety of phenomena ranging from soft to hard and finally to superparamagnetic behavior [1.16], depending on the ratio of the exchange correlation length to the average crystallite size and also on the crystallized volume fraction. Moreover, low magnetoelastic contributions to the macroscopic anisotropy due to the low or vanishing average saturation magnetostriction for a determined crystallized fraction must be considered. The crucial role

of the exchange interaction becomes most evident when the measuring temperature approaches the Curie temperature of the integranular amorphous phase T_c^{amor}~200-300°C, which is much lower than that of the bcc Fe (Si) grain (T_c~600°C) and the exchange coupling between the crystallites is largely reduced. While the temperature variation of the magnetic properties at temperature below T_c^{amor} is minor and smooth, the initial permeability above the T_c^{amor} drops down by almost two orders of magnitude and the coercivity increases correspondingly [1.17-1.19]. It is thus important to maintain an efficient exchange coupling between the grains by appropriate alloy design such that the Curie temperature of the residual amorphous matrix is clearly higher than application temperature. For example, too high addition of Nb, although favorable for grain refinement, can be disadvantageous because they decrease the Curie temperature of the amorphous matrix considerably.

One further advantage of this novel magnetic system is that one can play with different compositions and annealing temperatures to control the grain size and their distribution and thereby tailor the magnetic properties of this new material. In choosing the composition one has to consider the magnetic components like Fe, Co, Ni, etc, the crystallizing component such as Cu and the component Nb for stabilizing the nanocrystals by inhibiting their growth and glass forming materials like silicon, carbon, boron etc. Nanocrystalline materials are more complex compared to conventional materials because it contains nanocrystalline magnetic grains embedded in an amorphous matrix and as such represents surface, interfacial and bulk magnetic particles. The nanosized magnetic particles are coupled by exchange force and are susceptible to intergranular distance, grain size and their distributions. Crystallization behavior and grain size are very much correlated with the magnetic properties.

Amorphous ferromagnetic materials based on Fe-Si-B show good soft magnetic properties when they are heat treated below their crystallization temperature. Extraordinary high permeability, two order of magnitude higher than their conventional Fe-Si-B alloys, was developed after partial crystallization $Fe_{73.5}Cu_1Nb_3Si_{13.5}B_9$ subjected to heat treatment just above the crystallization temperature for a specific time. As a result of heat treatment, the annealed nanometric grain size of ≈ 4-30nm is developed in the residual amorphous

matrix. Best magnetic properties are obtained when the grain size is ≈ 10-12nm. Good magnetic properties are obtained when D<< L_{ex}, where L_{ex} is the ferromagnetic exchange length[1.20-1.21] and D is the average grain size. According to calculation, for Fe(Si) alloy, L_{ex} ≈ 35 nm [1.22]. Responds of nanostructured magnetic materials to the frequency of the external field can be controlled by varying the grain sizes and their distributions.

Long-term thermal stability of the magnetic properties is a further requirement for application, in particular at elevated operation temperatures. Empirically, thermally induced aging of the magnetic properties is the more critical the better these properties. Apart from temperature and time, the aging behavior also depends on the magnetizing conditions during operation whose limiting cases are the remanent or demagnetized state and the ferromagnetically saturated state, respectively. The thermal stability of the nanocrystalline material surface by far that of amorphous alloys and oven that of permalloys. The mechanism of thermal aging, in principal are the same as those which are used to tailor the magnetic properties during annealing but a reduced kinetics due to the comparably lower operation temperature. A dominant contribution arises from the formation of the locally field induced uniaxial anisotropy along the magnetization vectors within the ferromagnetic domains. The reduced degrees of freedom for anisotropy formation due to the super lattice structure together with the high Curie temperature allow to stabilize very small induced anisotropies and, hence, high permeabilities at annealing temperature much higher than it is possible for highly permeable amorphous alloys or permalloy. This essentially reduces the kinetics for anisotropy changes at application temperatures. In comparison with amorphous metals, the thermal stability is additionally improved by the more stable crystalline structure.

The great scope of technical applications of this material $Fe_{73.5}Cu_1Nb_3Si_{13.5}B_9$ arises from this freedom of tailoring the magnetic properties [(1.23-1.26)]. The present work is therefore mainly aimed at for the enhancement of the initial permeability of the initial permeability of the optimum crystallized samples. Crystallization kinetics by differential thermal analysis and ferromagnetic transition temperatures measured by temperature dependence magnetization curve of the composition $Fe_{73.5}Cu_1Nb_3Si_{13.5}B_9$. It has been determined important to study crystallization behavior, grain size, crystallization onset

temperature, nanocrystalline state to intermediate state transition temperature, change of Si content and lattice parameter of the nanocrystals etc before going to measure the magnetic properties of this nanocrystalline composition. In the present study amorphous ribbon of the composition prepared and studied in detail the above mentioned properties by X-ray diffraction (XRD) method after heat treatment at different temperatures.

1.2 Organization of the work

The preparation procedures are described in chapter-2. The theoretical aspects of the stability of amorphous alloys, theories of X-ray diffraction permeability and magnetization are described in chapter-3, chapter-4 contains the experimental details including Differential Thermal Analysis (DTA), Vibrating Sample Magnetometer (VSM), X-ray Diffractometer and Impedance Analyzer.

The details of the results regarding DTA, X-ray diffraction (XRD) method after heat treatment of the samples at different temperatures, step annealing on frequency dependence of initial permeability, anneal effect on magnetization curve and temperature dependence magnetization are discussed in chapter-5. It also contains comments on the suitability of the specimens studied, in respect of relative quality factor, loss factor and the frequency range in which these materials can be used. Chapter- 6 obtains conclusions, achievement of works and future suggestions of this work.

Chapter-2

Preparation of Nanocrystalline Amorphous Ribbon by Rapid Quenching Method

2.1 Introduction

A new class of iron based alloys exhibiting superior soft magnetic properties has been behavior has been discovered by Yoshizawa [2.1]. The composition of the alloy was $Fe_{73.5}Cu_1Nb_3Si_{13.5}B_9$ and has been given the trade name FINEMET. An appropriate heat treatment above the crystallization temperature produces ultra fine microstructure of bcc Fe(Si) with typical grain sizes of 10-15 nm embedded in the residual amorphous matrix. As a result the magnetic characteristics of nanocrystalline materials are controlled by both the nanocrystallites and the amorphous medium in which these crystallites are developed.

The crystallization of amorphous metals optimized for the soft magnetic application was rather known to deteriorate the properties significantly and resulted a relatively coarse microstructure with grain sizes of about 0.1-1 μm. Only partially crystallized amorphous Fe-base alloys were seen to offer eventual benefits over the amorphous state for certain high frequency applications [2.2-2.3]. The combination of small grain size and soft magnetic properties is surprising and fascinating from the classical point of view in magnetic engineering. Yet, this possibility was principally known from amorphous materials and the theoretical interpretation of their soft magnetic properties was given by Alben, *et. al.*[2.4]. Accordingly, magnetic softening should also occur as soon as the structural correlation length or grain size becomes smaller than the ferromagnetic exchange length which is in the order of the domain wall width. In this case the local anisotropies are randomly averaged out by exchange interaction so that is no anisotropy net effect on the magnetization process. The optimum alloy composition originally proposed $Fe_{73.5}Cu_1Nb_3Si_{13.5}B_9$ (at. %) and can be considered as a typical Fe-Si-B metallic glass composition with small addition of Cu and Nb. The alloy system has a good glass forming ability and is easily accessible by rapid quenching techniques.

2.2 An overview of Nanocrystalline Amorphous Ribbon

Nanocrystalline amorphous ribbons can be considered as an off-shoot of amorphous materials. In fact nanocrystalline amorphous ribbon is a composite material where nanocrystals are embedded in an amorphous matrix. Nanocrystalline materials

represent one of the most active research item in recent times for the atomic tailoring of materials with specific properties and property combinations. However, it is still in its infancy since its emergence as a major materials science has just began at this stage of development, there have been glimpses of exciting new properties like super plasticity, giant magnetoresistance (GMR), transparency in opaque ceramics, enhanced homogeneity, unusual soft ferromagnetic and giant magnetocaloric effects, possessed by material which has been reduced to nanometer dimension. In addition to the understanding of the unusual properties possessed by nano phase materials, there are three other associated areas, which need serious attention.

1. Identification and development of suitable preparation methods, especially those, which are capable of providing large industrial quantities of nanometer scale materials.
2. Development of processing methods for manufacturing these materials into useful size and shapes without losing there desirable nanometer size feature and
3. Identification of proper characterization methods, where the nanometer size range of these materials falls just below or at the resolution limit of the conventional tools.

Nanocrystalline soft magnetic alloys have received considerable attention due to their excellent soft magnetic properties [2.5]. Small addition of Cu and Nb into Fe-Si-B amorphous materials changes considerably their crystallization process, which is executed under appropriately controlled conditions.

1. The element Cu is used for helping the formation of nuclei of ultrafine grains.
2. The element Nb is used to impede the growth of the crystallites.

In this material, the nanocrystalline state is composed of a fine structure of α-Fe (Si) nanocrystallites embedded in an amorphous matrix. The average size of α-Fe (Si) is usually around 10 nm. For such an average grain size the exchange interaction dominates the

magnetic behavior of randomly oriented crystallites guided by random anisotropy [2.6]. The relation between alloy components and the rotating speed is of importance in fabricating the high quality product. This new magnetic material of high quality is called Finemet.

2.3 Conditions for the Formation of Nanocrystalline State

The nanocrystalline state is achieved by annealing at temperatures typically between 500°C and 600°C, which leads to primary crystallization of bcc Fe. The resulting microstructure is characterized by randomly oriented, ultrafine grains of bcc Fe-Si, 20 at.% with typical grain size of 10-15 nm embedded in a residual amorphous matrix which occupies about 20- 30% of the volume and separates the crystallites at a distance of about 1-2 nm. These features are basis for the excellent soft magnetic properties indicated by the high values of the initial permeability of about 10^5 and correspondingly low coercivities of less than 1A/m. The nanocrystalline microstructure and the accompanying soft magnetic properties are rather insensitive to the precise annealing conditions within a wide range of annealing temperature, $T_a \approx$ 525-580°C. They develop in a relatively short period of time (about 10-15 minute) and do not much latter even after prolonged heat treatment of several hours [2.7]. A typical heat treatment like 1h at 540°C in most cases yields a nanocrystalline microstructure to the quasi-equilibrium state and characteristic for the individual alloy composition.

Only annealing at more elevated temperatures above about 600°C leads to the precipitation of small fractions of boride compounds like Fe_2B or Fe_3B. The formation of the particular nanocrystalline structure is essentially related to the combined addition of Cu and Nb and their low solubility in bcc Fe. Copper enhances the nucleation of the bcc grains while niobium impedes coarsening and, at the same time, inhibits the formation of boride compounds. The microstructure evolution is schematically illustrated in fig. 2.1 and can be summarized as follows.

The phase separation tendency between Cu and Fe leads to the formation of Cu rich clusters, about 5 nm in size and probably still amorphous, in the initial stage of

annealing before the onset of the primary crystallization of the bcc Fe-Si phase [2.8-2.9]. The presence of Nb, hereby seems to promote the formation of these Cu rich clusters on a much finer scale than in an Nb free alloy composition [2.10]. This cluster formation causes a concentration fluctuation of Fe, since Cu substitutes for Fe. Thus, the regions in between the Cu-rich clusters provide a significantly increased density of nucleation sites for the crystallization of bcc Fe. The consequence is an extremely fine nucleation of bcc Fe-Si crystallites at a high rate which subsequently grow in a diffusion controlled process [2.11] as the annealing proceeds further. As the bcc Fe- Si phase forms, Nb and B are excluded from the crystallites because of their low solubility in bcc Fe and are enriched in the residual amorphous matrix. At the same time effectively all Si tends to be partitioned into the bcc Fe-Si phase [2.12-2.13]. The enrichment with B and in particular, with Nb increasingly stabilizes the residual amorphous matrix and, thus, hinders coarsening of the bcc grains. The presence of Nb at the same time inhibits the formation of Fe boride compounds. The transformation finally ceases in a meta- stable two-phase microstructure of bcc Fe-Si embedded in an amorphous Fe-Nb-B matrix.

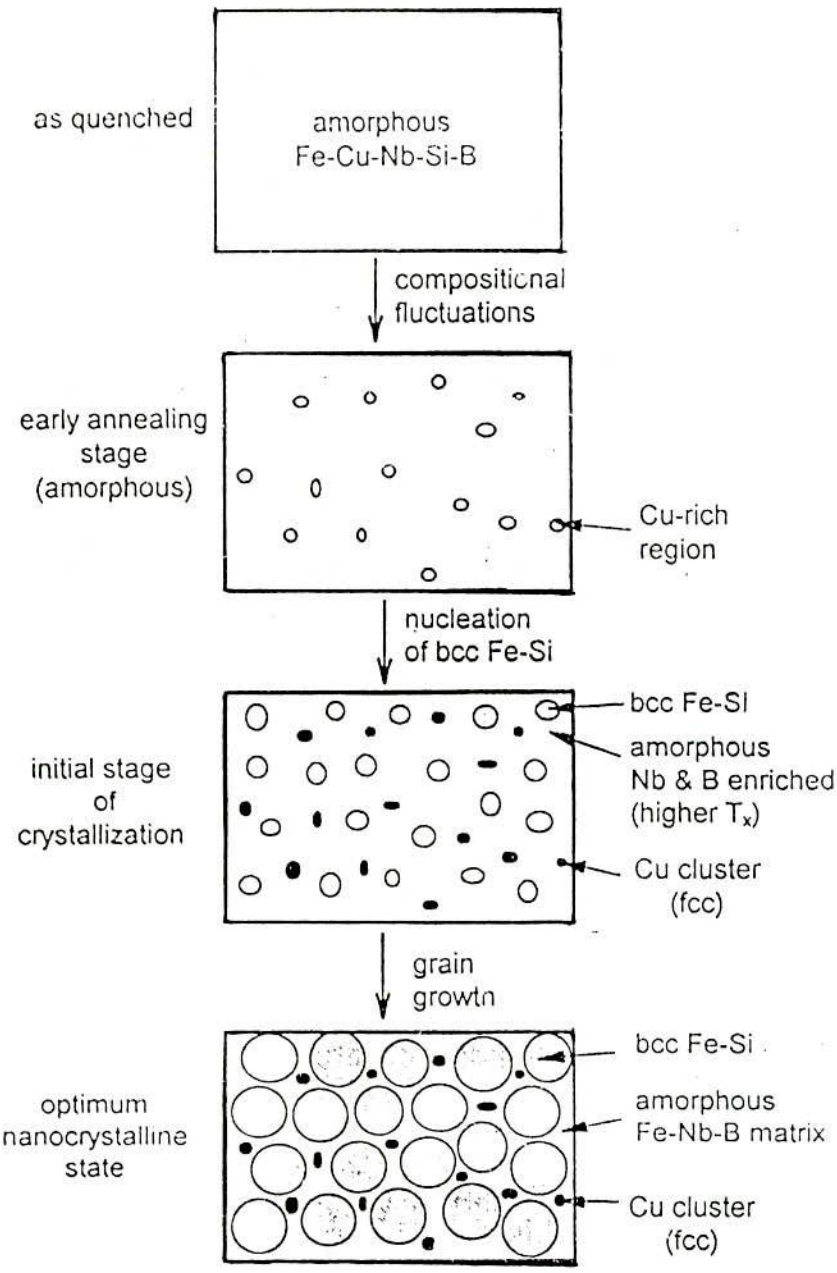

Fig . 2.1. - Schematic illustration of the formation of the nanocrystalline structure in Fe-Cu-Nb-Si-B alloys based on atom probe analysis results and transmission electron microscopy obsrvation (2.8 - 2.9)

2.4 Viscosity Condition for the Formation of Metallic Glass

In terms of viscosity and diffusion co-efficient we find the condition for formation of glass.

[1] The metals atomic bonding is metallic, the viscosity is lower than the diffusion co-efficient and mobility is high.

[2] In the amorphous state viscosity becomes high and the diffusion co-efficient decreases. Atomic bonds tend to be covalent as in the case of silicate (SiO_2).

2.5 Conditions Necessary for Preparing Nanocrystalline Materials

The necessary conditions for preparing nanocrystalline materials are:

[1] The magnetic properties are highly dependent on grain size; if the grain size is longer, the magnetic anisotropy would be very high, which in turn will have diverse effect on the soft magnetic properties specially the permeability.

[2] There should be nucleation centers initiated for the crystallization process to be distributed throughout the bulk of the amorphous matrix.

[3] There must be a nucleation for stabilizing the crystallites.

[4] Nanocrystalline materials obtained from crystallization must be controlled so that the crystallites do not grow too big. The grain growth should be controlled so that the grain diameter is within 15-20 nm.

[5] The size of the grains can be limited to nanometer scale by doping group – II metals etc.

→ Cu(Au.....)

→ Nb, W, Mo, Cr, Ta etc.

[6] The stability must be lower and the crystallization temperature must be higher.

2.6 Preparation Technique of Nanocrystalline Amorphous Materials

There are various techniques in use to produce a metallic alloy in an amorphous state where the atomic arrangements have no long-range periodicity. The different experimental techniques developed to amorphous metallic glass can be classified into two groups:

[1] The atomic deposition method.

[2] The fast cooling of the melt.

2.6.1 The Atomic Deposition Method

Deposition can be described in terms of whether the added atom is prevented from diffusing more than an atomic distance before it is fixed in position due to cooling and associated increased viscosity. The atomic deposition methods include condensation of a vapor on a cooled substrate by

[1] Vacuum deposition

[2] Sputter deposition

[3] Electro deposition

[4] Chemical deposition

2.6.2 The Fast Cooling of The Melt

The molten alloy must be cooled through the temperature range from the melting temperature (T_m) to the glass transition temperature (T_g) very fast allowing no time for crystallization. The factors controlling T_g and crystallization are both structural and kinetic. The structural factors as discussed by Turnbull [2.13] are the nucleation, crystal growth rate and diffusion rate compared to the cooling rate. The interest in this method originates from the wide variety of alloys that can be made as well as from the potential low preparation

cost. In the pioneering work of Duwez et.al.[2.14], a number of devices have been reported for obtaining the necessary high quenching rates and for producing continuous filaments. The methods using the principle of fast cooling of melt techniques are:

[1] The gun techniques

[2] Single roller rapid quenching techniques

[3] Double roller rapid quenching techniques

[4] Centrifuge and rotary splat quencher techniques

[5] Torsion catapult techniques

[6] Plasma - jet spray techniques

[7] Filamentary casting techniques

[8] Melt extraction techniques

[9] Free jet spinning techniques

[10] The melt spinning techniques

Although the different methods for reparation of amorphous metallic ribbons are mentioned here only the single roller rapid quenching technique was used to prepare the specimens for the present work.

2.6.3 Rapid Quenching Method

As shown in a schematic diagram in fig. 2.2, the rapid quenching technique apparatus consists mainly of a copper roller, an induction heater and a nozzle. A variable speed motor drove the roller via a tooth belt. The angular velocity was 2000 rev / min. Use of log wheel rotation enabled us to very the surface velocity in the range of 20 to 30 m / s. The diameter of the copper roller was 10 cm. The use of copper for the roller material was chosen for its good conductivity and mechanical softness, which allowed cleaning and polishing to be carried out easily.

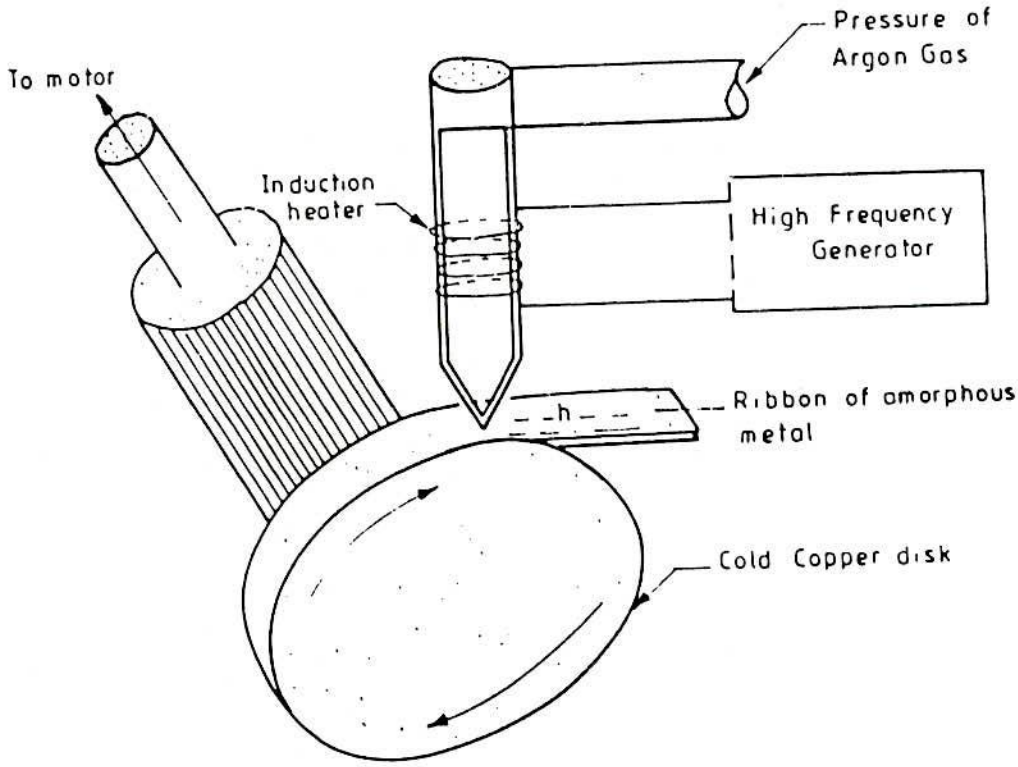

Fig. 2.2 Thin layer of molten alloy intimate contract with the outer surface of metallic rottor is quenched in to amorphous ribbon

In this process one has to consider that vibration of the roller should be well below the high frequency vibration of the melt puddle to avoid any influence of it on the geometry and uniformity of the ribbon. One has to be careful and see that the ribbon does not remain in contact with surface of the roller for a whole revolution and be hit, from the back. A bigger diameter is thus preferred for the roller. The induction heater coil is made of hollow copper tubing which is cooled simultaneously by circulating water through its inner hole. The shape and diameter of the induction heater as also its winding is to be adjusted to produce proper temperature gradient. This is to avoid sudden cooling of the melt in its way out of the crucible and blocking the nozzle. The quartz tubing having outer diameter 20 mm which is narrowed down conically to 1 mm with a whole for the nozzle 0.1 to 0.2mm.

The nozzle geometry is selected to minimize the contraction in the cross - sectional area of the molten jet as it leaves the nozzle orifice. Quartz tube is suitable for repeated use in several successful runs and should be transparent to make the melting process visible. It should withstand the sudden fast changes in temperature.

2.7 Experimental Details of the Preparation of Nanocrystalline Amorphous Ribbons

The component elements of the alloys are first melted in a furnace and then cooled. Thus resultsin a button shaped specimens. The buttons prepared are about 50 grams each. Care is taken to ensure through mixing and homogeneity of the alloy composition, by turning over and remelting each button few times. The mother alloys which are formed in the form of buttons in a furnace is then cut into small pieces and is introduced in the quartz tube. The quartz tube is connected from the top by rubber "O" rings and metal rings to the argon cylinder through a valve and a pressure gauge. After proper cleaning of the roller surface and adjusting its speed to the desired value, as measured by stroboscope the induction furnace is powered using high frequency generator. When the melting temperature is produced as observed through a protective spectacle, the injection pressure is applied by opening the pressure valve. To avoid the turbulence of the wind, arising from the high speed of the roller in disturbing the melt puddle, cotton pad and metallic shield are usually used

just beneath the roller. To avoid oxidation of the ribbon during its formation an inert atmosphere can be created around the roller by a slow stream of helium or argon gas .The speed of the roller, the volumetric flow rate, the diameter, the substrate orifice distance, the injection angle etc, are adjusted by trial and error to get the best result in respect of the quality and the geometry of the ribbon.

2.7.1 Important Factors to Control the Thickness of Ribbons

[1] Rotating speed

(a) Angular velocity ω = 2000 rev / min

(b) Surface velocity v = 20 m /s

[2] Gap between nozzle and rotating copper drum h = 100 to150 μm.

[3] Oscillation of the rotating copper drum both static and dynamic have maximum displacement 1.5 to 5 μm.

[4] Pressure = 0.2 to 0.3 argon atmosphere.

[5] Temperature of molten metals $T_m \cong 1500°$ C; other wise quartz tube would be melted.

[6] A steady flow of the molten metal on the surface of the rotating drum needs to be ensured.

2.8 Examining the Amorphousity of the Nanocrystalline Materials

To check the amorphousity of the Nanocrystalline sample, X-ray diffraction pattern for $Fe_{73.5}Cu_1Si_{13.5}Nb_3B_9$ are taken with Cu-K_α radiation using Philips (PW 3040) X' Pert PRO XRD system located at Atomic Energy Centre, Dhaka (AECD). Fig. 2.3 shows the X-ray diffraction pattern of the sample. No peak is observed within the scanning

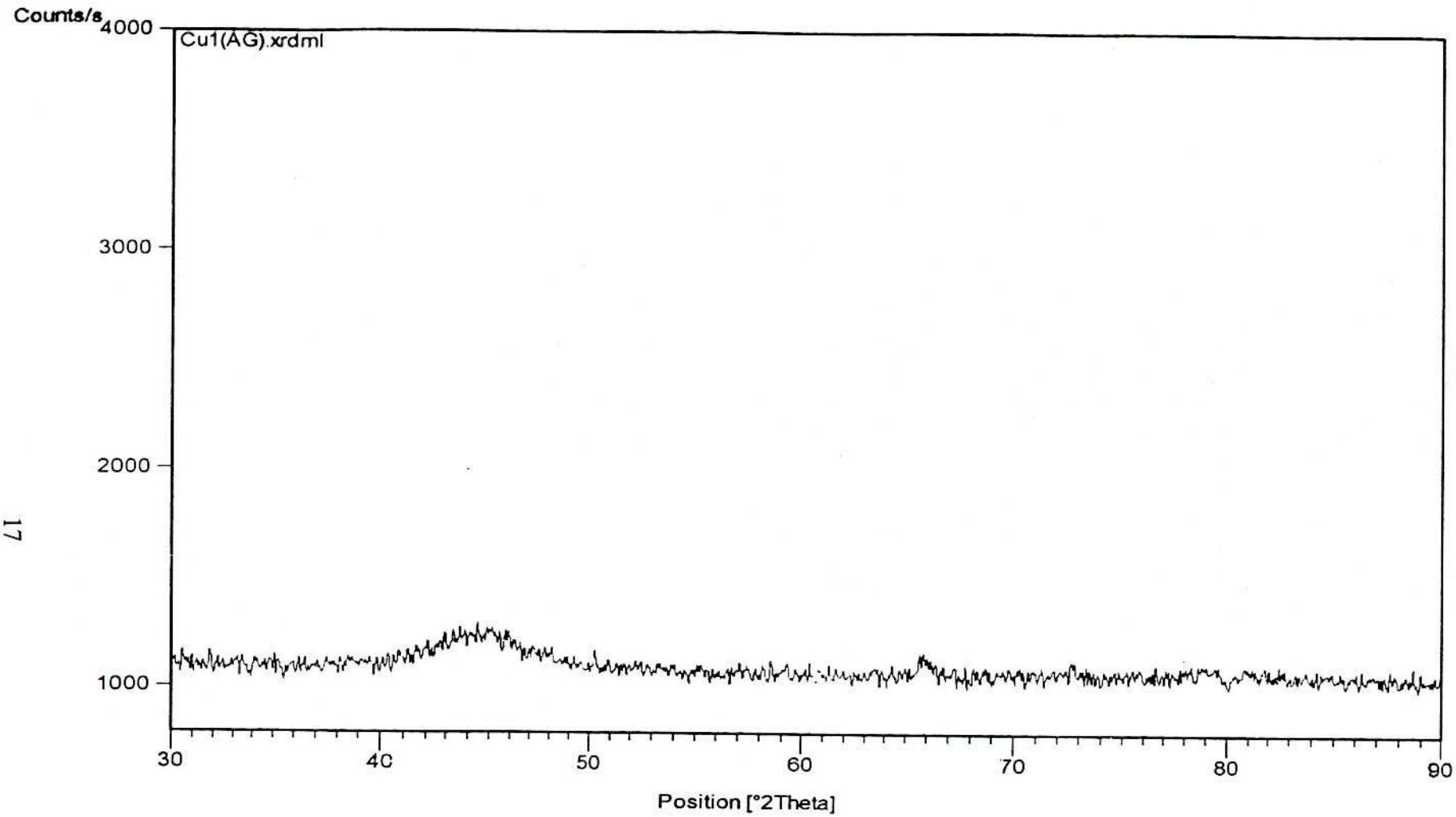

Fig. 2.3 X-ray diffraction of as-cast Nanocrystalline amorphous ribbon with composition $Fe_{73.5}Cu_1Nb_3Si_{13.5}B_9$

range of 30 to 90 degree and hence the amorphousity of the samples are confirmed. Although there are few small humps in the diffraction pattern, there is no reason to believe that those humps are due to existence of crystalline pocket. The average pattern of the X-ray diffraction shows the amorphous phase of the sample.

Chapter-3

Theoretical Aspects

3.1 Stability of Amorphous Nanocrystalline Materials

There are three kinds of stability of significance for amorphous magnetic alloys; their resistance to the initiation of crystallization, structural relaxation effects and the relaxation or reorientation of directional order. Actually, controlled crystallization from the amorphous state seems to be the only method presently available to synthesize nanocrystalline alloys with attractive soft magnetic properties. The amorphous nanocrystalline ribbon is prepared by rapid solidification from the melt - a meanwhile well stabilished technique for large scale production of amorphous alloys. Amorphous alloys are in a metastable state and tend to transform into stable crystalline phases. At temperature below the crystallization temperature, structural relaxation effects take place and are caused by atomic rearrangements. The formation and resultant stability of amorphous alloys are important topic both for theoretical understanding and technical application. From the thermodynamic view point [3.1-3.2], the ability of an alloy to be quenched into the glassy state is generally measured by the magnitude of the quantity,

$$\Delta T_g = T_m - T_g \quad , \tag{3.1}$$

where T_m and T_g are the melting and glass transition temperatures respectively. In a similar manner the stability of the glass after formation is generally measured by the magnitude of the quantity,

$$\Delta T_x = T_x - T_g \quad , \tag{3.2}$$

where T_x is the temperature for the onset of crystallization. As the temperature decreases from T_m, the rate of crystallization will increase rapidly but then fall rapidly as the temperature decreases below T_g. Thus if one quenched a molten alloy rapidly enough to a temperature below T_g a quasi-equilibrium amorphous phase is obtained. There is no direct relation between the case of formation and the resultant stability of an amorphous alloy. The amorphous alloy composition most favorable for glass formation is near the eutectic i.e. the composition in which the transformation from the liquid state to solid state takes place instantaneously with passing through liquid plus solid mixed phase. The deeper the eutectic the better is the glass formation ability [3.3]. At such a point the liquid is particularly stable

against crystallization. There have been three approaches for relating the stability of the glass, i.e., its microstructure.

[*i*] Bernal's model of randomly packed hard sphere's [3.4]: The metal atoms are assumed to from a random network of close packed hard spheres and the smaller metalloid atoms fill the holes inherent in such a structure.

[*ii*] The effect of atomic sizes and interatomic interactions [3.5], i.e. chemical bonding and suggested that it is chemical bonds which are the dominating factor in glass formation and stability.

[*iii*] The third approach [3.6] is based on the role of the electron gas and showed that under certain circumstances a nearly free electron gas will produce a barrier against crystallization.

The crystallization is associated with nucleation and growth process. Since the formation of an amorphous alloy depends on the absence of long-range order, change of composition is expected to affect T_g and T_x. This is because the long range ordering of atoms depends on the free energy difference between the crystalline state and the amorphous state. The change of composition affects the growth kinetics in a complicated way, which can only be determined experimentally. The transition to the glassy state and the crystalline state is accompanied by an exothermic heat effect giving rise to a sharp peak in temperature dependence of the exothermic heat. Therefore, differential thermal analysis (DTA) is a widely used technique to study thermally induced transformations in amorphous alloys and to determine T_g and T_x. The magnitude of T_g and T_x are very different for amorphous materials and depend strongly on composition. The activation energy ranges typically between 2 and 6 eV.

The difference of T_g on the heating rate $S = \frac{dT}{dt}$ can be used to determine the activation energy of crystallization [3.8]. Considering the fraction x of amorphous material transformed in to the crystalline state in time t and at temperature T, one obtains for the first order rate process.

The incubation time therefore implies that no stable sized nuclei exist in the as-quenched ribbon. Equation (3.7) can be derived from transformation theory, where ΔE_x is the activation energy for viscous flow; and other terms have been omitted because they have an insignificient temperature dependence in this region of temperature. Correlations between thermal stability as measured by ΔT_x and ΔE_x were discussed experimentally and theoretically [3.9], but using the fine of transformation to the peak in the exotherm, rather than to the start of the exotherm, to obtain ΔE_x. The effect of this difference in measurement on ΔE_x appears to be small.

3.2 Theory of X-ray powder Method

A single crystal with a particular set of atomic planes oriented toward the X-ray beam will diffract X-ray at an angle θ determined by the Bragg equation.

$$2d \sin\theta = \lambda , \qquad (3.8)$$

where λ is the wavelength of X-ray, d is distance between the planes. Most materials are not single crystals but are composed of billons of very small crystallite. This type of material is referred to as a powder or polycrystalline aggregate. In these materials, there are a great number of crystalline in all possible orientations. Thus, when a powder is placed in an X-ray beam all possible inter atomic planes will be seen by the beam but diffraction from each different type of plane will only occur at its characteristics diffraction angle θ. Thus, instead of a dot pattern, a powder pattern is a series of concentric rings.

The powder diffraction patterns can be recorded on a strip of film surrounding the sample. The camera which carries out this diffraction pattern is called a Debye- scherred camera. Today most patterns are obtained from powder diffractometer.

Each peak in pattern shown in fig. 3.1 corresponds to diffraction from a particular set of interatomic planes, whose spacing d_{hkl} may be calculated from the Bragg equation. We use X-ray of known wavelength and the value of θ can be measured directly on the diffraction pattern. Further, we can find the index $[hkl]$ of each peak that means to define

the inter atomic plane corresponds to the peak. After index we can define the type of the structure of the crystallographic cell, calculate the crystallographic parameter. The calculation mentioned above depends on the symmetry of the crystal. For the cubic system, the index is following

We have,

$$\frac{1}{d_{hkl}^2} = \frac{1}{a^2}(h^2 + k^2 + l^2) \qquad (3.9)$$

and from the Bragg equation ,

$$d_{hkl} = \frac{\lambda}{2\sin\theta} \qquad (3.10)$$

So $\sin^2\theta = \frac{\lambda^2}{4a^2}(h^2 + k^2 + l^2)$ (3.11)

or , $\sin\theta = \frac{\lambda}{2a}\sqrt{h^2 + k^2 + l^2}$ (3.12)

or, $y = Kx$

For every plane (every set of $[hkl]$) $K = \sqrt{h^2 + k^2 + l^2}$ is an integer and is constant. So $y = \sin\theta$ is linear function of $x = \frac{\lambda}{2a}$.

We can draw graphics y = K.x with different value of as shown in fig. 3.2.

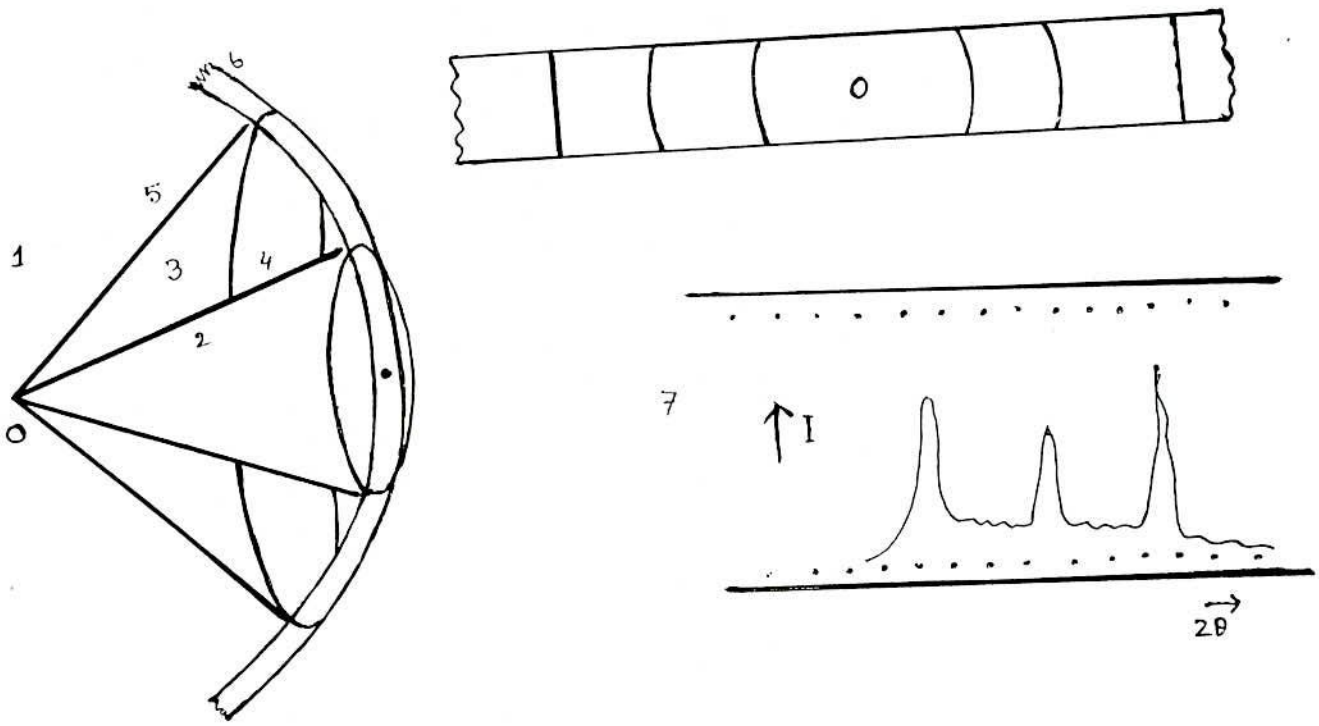

Fig. 3.1.

1 : Ewald sphere
2, 3 : Sphere of $\vec{G}$ extremities
4, 5 : Cone of diffraction directions
6 : Diffraction lines on the strip of film around the sample
7 : Diffractionn diagram from diffractometer

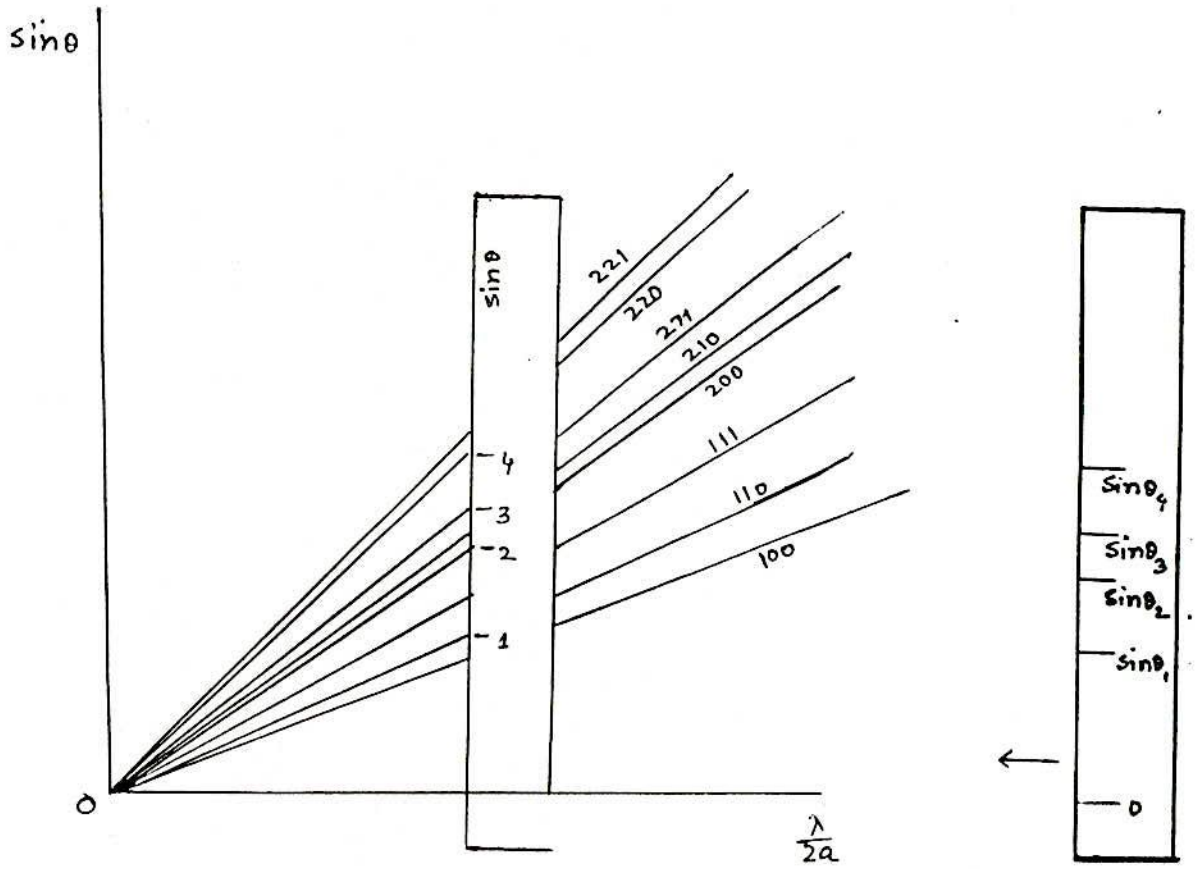

Fig . 3.2 Index diffraction lines (cube system)

Every set of the values sinθ from the diffraction pattern corresponds to the value y = sinθ on the graphic at a definite value x = $\frac{\lambda}{2a}$. We can find this value if we mark on the strip of paper all values sinθ calculated from the diffraction pattern and move the strip parallel to the abscises (fig. 3.2) until all the marks coincides with the value y = sinθ on the graphics. So we can define $\frac{\lambda}{2a}$ and the index h, k, l of every peak is found directly on the graphic.

In comparison with the graphic, may be there are not equivalent marks on the strip of paper, that means these reflections indirect structure factor ($[hkl] = 0$).

So after index, we can define the type of the cell (simple cubic, fcc, bcc, diamond)

Because

$$a = d_{hkl}\sqrt{h^2 + k^2 + l^2} = \frac{\lambda}{2\sin\theta}\sqrt{h^2 + k^2 + l^2} \quad , \qquad (3.13)$$

the value λ is given with high accuracy . So,

$$\left|\frac{\Delta a}{a}\right| = \cot\theta \times \Delta\theta \qquad (3.14)$$

$\cot\theta$ decrease to 0, when θ increase to 90° . This is the reason why for measuring a, we have to choose some peaks corresponds to the large θ and make an extrapolation to $\theta = 90°$.

3.2.1 Effect of Fine particle Size

The width of the diffraction curve of fig. 3.3 increases as the thickness of the crystal decreases, because the angular range ($2\theta_1 - 2\theta_2$) in cases as in decreases.

The width β is usually measured in radians, an intensity equal to half the maximum intensity. As a rough measure of β, we can take half the difference between the

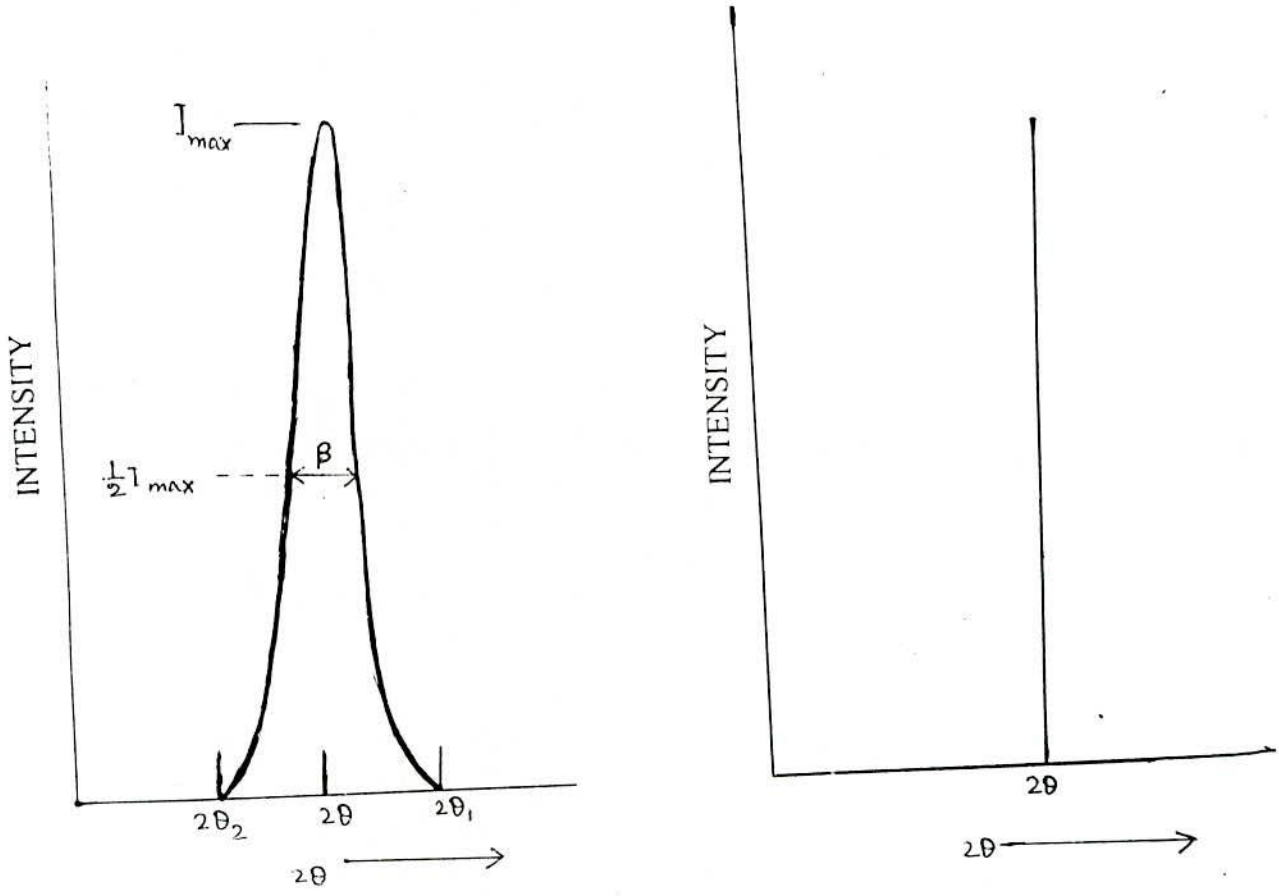

Fig. 3.3 Effect of fine particle size on diffraction curves (schematic)

two extreme angles at which the intensity is zero, which amounts to assuming that the diffraction line is triangular in shape. Therefore,

$$\beta = \frac{1}{2}(2\theta_1 - 2\theta_2) = \theta_1 - \theta_2 \qquad (3.15)$$

We now write path difference equations for these two angles, related to the entire thickness of the crystal rather then to the distance between adjacent planes.

$$2D_g \sin\theta_1 = (m+1)\lambda \qquad (3.16)$$

$$2D_g \sin\theta_2 = (m-1)\lambda \qquad (3.17)$$

By subtraction we find.

$$D_g(\sin\theta_1 - \sin\theta_2) = \lambda$$

$$D_g.2\cos(\frac{\theta_1+\theta_2}{2})\sin(\frac{\theta_1-\theta_2}{2}) = \lambda \qquad (3.18)$$

But θ_1 and θ_2 are both very nearly equal to θ , so that

$$\theta_1 + \theta_2 = 2\theta \quad \text{(approx)}$$

and $$\sin\left(\frac{\theta_1-\theta_2}{2}\right) = \left(\frac{\theta_1-\theta_2}{2}\right) \quad \text{(approx).}$$

Therefore equation (3.18) can be written as.

$$2D_g Cos\theta.\left(\frac{\theta_1-\theta_2}{2}\right) = \lambda \qquad (3.19)$$

equation (3.15) and equation (3.19) we get

$$\beta.D_g \, Cos\theta = \lambda$$

$$\therefore D_g = \frac{\lambda}{\beta\cos\theta} \qquad (3.20)$$

A more exact treatment of the problem given

$$D_g = \frac{0.9\lambda}{\beta \cos\theta} \quad , \tag{3.21}$$

which is known as the Scherrer formula .It is used to estimate the particle size of very small crystals from the measured width of their diffraction curves

3.2.2 Effect of Particle Size on Different Parameters

The smallness of the size of the crystallite will cause a broadening of the interference function which obviously means that the corresponding Laue-Bragg conditions will be modified as

$$a_1.s = h_i + u_i \tag{3.22}$$

Where h_i's are integer and u_i' s are fraction less than unity. This signifies that the intensity will not be sharply concentrated at the corresponding Bragg angle θ. In terms of reciprocal lattice, there will be a speed of intensity around the reciprocal lattice point h_i corresponding to θ, and the spread which will be dependent on crystalline size is a measure of the smallness of the size provided there is no other defect in the sample under study. Let us now discuss one by one the effect and relationship of particle size with different line broadening parameters as defined earlier.

3.2.3 Intensity Factors

Powder diffraction intensity depends on the following factors

(a) Structure factor

(b) Multiplicity factor

(c) Lorentz – polarization factor

(d) Absorption factor

(e) Temperature factor

(a) Structure Factor

Any scattered wave in the complex exponential for

$$Ae^{i\phi} = fe^{2\pi i(hu+kv+lw)} \tag{3.23}$$

The resultant wave scattered by all the atoms of the unit cell is called the structure factor, because it describes how the atom arrangement, given by u v w for each atom, affects the scattered beam. The structure factor, designated by the symbol F is obtained by simply adding together all the waves scattered by the individual atoms .If a unit cell contains atoms 1, 2, 3, ---------, N with fractional co-ordinates [u_1 v_1 w_1], [u_2 v_2 w_2], [u_3 v_3 w_3] ----------, and atomic scattering factors f_1, f_2, f_3--------- ,then the structure factor for the $[hkl]$ reflection given by

$$F = f_1 e^{2\pi i(hu_1+kv_1+lw_1)} + f_2 e^{2\pi i(hu_2+kv_2+lw_2)} + f_3 e^{2\pi i(hu_3+kv_3+lw_3)} + \text{-------} \tag{3.24}$$

This equation may be written more compactly as

$$F_{hkl} = \sum_{n=1}^{N} f_n e^{2\pi(hu_n+kv_n+lw_n)}, \tag{3.25}$$

where the summation extends over all the N atoms of the unit cell. F is, in general, a complex number, and it expresses both the amplitude and phase of the resultant wave, its absolute value $|F|$ gives the amplitude of the resultant wave interms of the amplitude of the wave scattered by a single electron.

Like the atomic scattering factor f, $|F|$ is defined as a ratio of amplitudes,

$$|F| = \frac{\text{Amplitude of the wave scattered by all the atoms of a unit cell}}{\text{Amplitude of the wave scattered by one election}}$$

The intensity of the beam diffracted by all the atoms of the unit cell in a direction predicted by the Bragg law is proportional simply to $|F|^2$, the square of the amplitude of the resultant beam, and $|F|^2$ is obtained by multiplying the expression given for F in equation (3.25) by its complex conjugate equation (3.25) is therefore a very important relation in

X-ray crystallography, since it permits a calculation of the intensity of any $[hkl]$ reflection from a knowledge of the atomic positions.

(b) Multiplicity Factor

Relative proportion of planes contributing to the same reflection enters the intensity equation as the quantity multiplicity factor (p), which may be defined as the number of different planes in a form having the same spacing. Parallel planes with different planes in a form having the same spacing. Parallel planes with different Miller indices, such as (100) and $(\bar{1}00)$, are counted separately as different planes, yielding numbers which are double these given in the preceding paragraph. Thus the multiplicity factor for the $\{100\}$ planes of a cubic crystal is 6 and for the $\{111\}$ planes 8. The value of multiplicity factor depends on the crystal system: in a tetragonal crystal, the (100) and (001) planes do not have the same spacing, so that the value of multiplicity factor for $\{100\}$ planes is reduced to 4 and the value for $\{001\}$ planes to 2. Values of the multiplicity factor as a function of [hkl] and crystal system.

c) Lorentz-Polarization Factor

The Thomson equation for the scattering of an X-ray beam by a single crystal. The intensities of two scattered components

$$I_p = I_0 \frac{k}{r^2}\left(\frac{1+Cos^2 2\theta}{2}\right) \qquad (3.26)$$

The intensity of the scattered beam is only a minute fraction of the intensity of the incident beam; the value of $k = 7.94\times10^{-30} m^2 and \frac{I_p}{I_o} = 7.94\times10^{-26}$ in the forward direction at 1 cm from the electron. The last factor of equation (3.26) i.e. $\frac{1}{2}(1+\cos^2 2\theta)$ is called the polarization factor.

The breadth of the diffraction curve varies in the opposite way, being larger at large values of 2θ, where the half maximum breadth to be proportion to $\frac{1}{\cos\theta}$. The integrated intensity of the reflections is given by the area under the diffraction curve and is proportional to $\left(\frac{1}{Sin\theta}\right)\left(\frac{1}{Cos\theta}\right)$ or $\frac{1}{\sin 2\theta}$. Thus as a crystal is rotated through the Bragg angle, the integrated intensity of a reflection, which is the quantity of most experimental interest turns out to be greater for large and small values of 2θ than for intermediate values, other things being equal. The number of crystals favorably oriented for reflection is thus proportional to cosθ and is quite for reflections in the backward direction . The relative intensity per unit length of line is proportional to $\frac{1}{\sin 2\theta}$.

In intensity calculations, the three factors just combined into one and called the Lorentz factor.

$$\text{Lorentz factor} = \left(\frac{1}{Sin2\theta}\right) Cos\theta \left(\frac{1}{Sin2\theta}\right)$$

$$= \frac{1}{4\sin^2\theta\cos\theta} \qquad (3.27)$$

The combined Lorentz - polarization factor, which, with a constant factor $\frac{1}{8}$ omitted, is given by

$$\text{Lorentz - Polarization factor} = \frac{1+\cos^2 2\theta}{\sin^2\theta\cos\theta} \qquad (3.28)$$

The over all effect of these geometrical factors is to decrease the intensity of reflection at intermediate angles compared to those in forward or backward directions.

d) Absorption Factor

X-ray are attenuated when passing through matter. This loss of electromagnetic energy is due to two effects, conversion of energy to thermal energy and scattering X-ray beam of intensity I that changes to I + dI by passing through a thickness dx of a material. The law which holds good is

$$\frac{-dI}{I} = \mu x \qquad (3.29)$$

By integration and putting $I = I_0$ when $x = 0$,

We get

$$I = I_0 e^{-\mu x} \quad , \qquad (3.30)$$

an expression called Bear's law . The factor μ has the dimension of a reciprocal length and depends on the state of the material. It is called the linear absorption coefficient.

In addition to the linear absorption coefficient, two further types of absorption coefficients are used. The first, denoted by μ_m, is the ratio of μ and the density d , and is called the mass absorption coefficient

$$\mu_m = \frac{\mu}{d} \qquad (3.31)$$

Unlike linear absorption coefficient, mass absorption coefficient is independent of the physical and chemical state of the material. Hence the mass absorption coefficient of a substance consisting of several elements can be calculated by simple addition of the mass absorption coefficients of the individual elements with proper weightages. The 2nd is called the atomic absorption coefficient, which is defined for a material of single element as

$$-\frac{dI}{I} = \mu_a dx \quad , \qquad (3.32)$$

where dx is the number of atoms in the path of the beam per unit area and μ_a is the atomic absorption coefficient. The value of μ_a depends on the element. For a given element, μ_a (and also $\frac{\mu}{d}$), depends on wavelength. Sharp discontinuities occur at particular value of λ. These discontinuities are called absorption edges, found one in the K-series, and there in the L- series. They can be understood in terms of electronic structure of the atoms. When an X-ray quanta has energy less than the energy to remove an electron, their photoelectrical absorption is possible and the quanta interact with the whole atom increasing in energy which is equivalent to increasing its temperature. If the critical energy is E_k and absorption edge attains the corresponding magnitude $\lambda_k = \frac{hc}{E_k}$, the electron in K- shell is ejected .

Therefore μ_a increases discontinuously at λ_k. Between the absorption edges, μ_a is given by

$$\mu_a = eZ^4 \lambda^{\frac{5}{2}}, \qquad (3.33)$$

where Z is the atomic number of the material and e is a constant . The value of e depends on the nature of two flanking absorption edges.

e) Temperature Factor

A crystal is a collection of atoms located at fixed points in the lattice. Actually the atoms undergo thermal vibration about their mean positions even at the absolute zero of temperature, and the amplitude of this vibration increases as the temperature increases. In aluminum at room temperature, the average displacement of an atom from its mean position is about 0.17A°, which is by no means negligible, being about 6 percent of the distance of closest approach of the mean atom positions in this crystal. Increased thermal vibration of the atoms, as the result of an increase in temperature, has three main effects.

(i) The unit cell expands, causing changes in plane spacing d and therefore in the 2θ positions of the diffraction lines. If the positions of one or more lines are measured as a function of temperature the thermal expansion coefficient of the specimen can be determined by X-ray diffraction.

(ii) The intensities of the diffraction lines decrease.

(iii) The intensity of the background scattering between lines increases.

Here we are usually interested not in intensity changes with temperature, but in variations in intensity with 2θ of constant temperature (usually room temperature).

3.3 Initial Permeability of Nanocrystalline Alloys

Low effective magnetocrystalline anisotropy and low or vanishing magnetostriction are the key to superior soft magnetic properties. The nanocrystalline alloys offer the highest saturation induction, B_s and simultaneously, the highest level of permeability (μ'). Typical commercial grades by now available under the tradenames FINEMET[3.10] and VITROPERM[3.11] are of the compositions $Fe_{\sim 74}Cu_1Nb_3Si_{13\sim 16}B_{6\sim 9}$ and offer a saturation induction of typically B_s = 1.2–1.3 T and initial permeability $\mu_i \approx 150\times10^3$. Highest permeabilities are required for magnetic cores in ground fault interrupters or common mode chokes.

The complex magnetic properties of initial permeability (μ_i) may be strongly affected by the presence of an electric current, particularly in ac condition. Moreover, the effects are rather different in as quenched amorphous nanocrystalline ribbons. The measurement of magnetic properties as a function of frequency and its analysis by means of the complex permeability formalism has recently led to the resolution of several aspects of magnetizations process [312-314]. The measurement of complex permeability gives as valuable information about the nature of the domain wall and their movements. Low losses, good high frequency behavior, favorable temperature dependence and high thermal stability of the soft magnetic properties are requirements fulfilled by the nanocrystalline alloy. In dynamic measurements the eddy current loss is very important which occurs due to

irreversible domain wall movements that are frequency dependent. The only draw-back of the nanocrystalline material seems to be the severe embrittlement upon crystallization which requires final shape annealing and restricts their application mainly to toroidally wound cores. The present goal of most of the recent nanocrystalline amorphous ribbons researches is to fulfill this requirement. Before going into the complexity of initial permeability measurement, we discuss in short the theories and mechanism involved in frequency spectrum of initial permeability and also affected by annealing.

3.3.1 Theories of Permeability

The primary requirement is the highest possible permeability, together with low losses in the frequency range of interest. The initial permeability μ_i is defined as the derivative of induction **B** with respect to the initial field **H** in the demagnetization state.

$$\mu_i = \frac{d\mathrm{B}}{d\mathrm{H}}, \mathrm{H} \to 0, \mathrm{B} \to 0 \qquad (3.34)$$

At microwave frequency, and also in low anisotropic amorphous materials, dB and dH may be in different directions, the permeability thus has a tensor character. In the case of amorphous materials containing a large number of randomly oriented magnetic atoms the permeability will be scalar. As we have

$$\mathrm{B} = \mu_0 (\mathrm{H} + \mathrm{M}), \qquad (3.35)$$

and susceptibility ,

$$\chi = \frac{dM}{dH} = \frac{d}{dH}(\frac{B}{\mu_o} - H) = \frac{1}{\mu_o}(\mu - 1) \qquad (3.36)$$

The magnetic energy density

$$\mathrm{E} = \frac{1}{\mu_0} \int \mathrm{H}.d\mathrm{B} \qquad (3.37)$$

For time harmonic fields $\mathrm{H} = \mathrm{H}\sin\omega t$, the dissipation can be described by a phase difference δ between **H** and **B.** In the case of permeability, defined as the proportional constant between the magnetic field induction **B** and applied intensity **H** ;

$$B = \mu H \tag{3.38}$$

This naive definition needs further sophistication. If a magnetic material is subjected to an ac magnetic field as we get,

$$B = B_0 e^{i\omega t} \tag{3.39}$$

Then it is observed that the magnetic flux density B experiences a delay. This is caused due to the presence of various losses and is thus expressed as,

$$B = B_0 e^{i(\omega t - \delta)} \quad , \tag{3.40}$$

where δ is the phase angle and marks the delay of **B** with respect to **H**, the permeability is then given by

$$\mu = \frac{B}{H}$$
$$= \frac{B_0 e^{i(\omega t - \delta)}}{H_0 e^{i\omega t}}$$
$$= \frac{B_0 e^{-i\delta}}{H_0}$$
$$= \frac{B_0}{H_0}\cos\delta - i\frac{B_0}{H_0}\sin\delta$$

$$\mu = \mu' - i\mu'', \tag{3.41}$$

where

and
$$\mu' = \frac{B_0}{H_0}\cos\delta \tag{3.42}$$

and
$$\mu'' = \frac{B_0}{H_0}\sin\delta \tag{3.43}$$

The real part μ' of complex permeability μ as expressed in equation (4.41) represents the component of **B** which is in phase with **H**, so it corresponds to the normal permeability. If there are no losses, we should have $\mu = \mu'$. The imaginary part μ'' corresponds to that part of **B** which is delayed by phase δ from **H**. The presence of such a

component requires a supply of energy to maintain the alternating magnetization, regardless of the origin of delay. It is useful to introduce the loss factor or loss tangent (tanδ). The ratio of μ'' to μ' ,as is evident from equation gives ,

$$\frac{\mu''}{\mu'} = \frac{\frac{B_0}{H_0}\sin\delta}{\frac{B_0}{H_0}\cos\delta} = \tan\delta \qquad (3.44)$$

This tanδ is called the loss factor .The Q – factor or quality factor is defined as the reciprocal of this loss factor i.e.

$$Q = \frac{1}{\tan\delta} \qquad (3.45)$$

And the relative quality factor $= \frac{\mu'}{\tan\delta}$. The behavior of μ' and μ'' versus frequency is called the permeability spectrum .The initial permeability of a ferromagnetic substance is the combined effect of the wall permeability and rotational permeability mechanisms.

3.3.2 High Frequency Behavior and Losses

The frequency dependence of the absolute value of complex permeability and its imaginary part μ'' are expressed in terms of the relative loss factor $\frac{\mu''}{|\mu|^2}$. The later is directly related to the cycle losses at constant induction amplitude B by

$$\frac{P}{f} = \frac{\pi B^2 \mu''}{\mu_0 |\mu|^2} \tag{3.46}$$

The frequency dependence of permeability and the core losses of the nanocrystalline Fe-Cu-Nb-Si-B alloys are comparable to those of amorphous Co-based alloys and pass by the properties of conventional materials, even that of ferrites, over the whole frequency range up to several 100KHz.

The favorable high frequency behavior is essentially related to (1) the thin ribbon gauge of d $\approx$ 20 μm inherent to the production technique and (ii) to a relatively high electrical resistivity of typically $\rho \approx 115 \mu\Omega$ - cm related to the high Si content in the bcc grains [3.15] and the intergranular amorphous phase. Both parameters are comparable to amorphous metals and yield low eddy current losses P_e, which in thin sheets at a frequency f and a induction level B are given per volume by [3.16]

$$P_e = \frac{3\sinh x - \sin x}{x\cosh x - \cos x} \frac{(\pi d f B)^2}{6\rho}$$

$$P_e \underset{x \langle\langle 1}{\approx} \frac{(\pi d f B)^2}{6\rho}, \tag{3.47}$$

with

$$x = 2\sqrt{\frac{f}{f_w}}$$

where

$$f_w = \frac{4\rho}{\pi \mu_o \mu_i d^2}, \tag{3.48}$$

is the limiting frequency above which the exciting magnetic field no longer fully penetrates the specimen and, accordingly, the permeability decreases as a function of the frequency.

3.4 Magnetization of the Amorphous Ribbons

The saturation magnetization of material at a temperature of 0°K is one of its basic properties. Measurements are usually expressed as average moment per magnetic atom in units of Bohr magneton, μ_B or as specific saturation magnetization for the amorphous alloy, σ_s, in units of Am^2/Kg. The moments of most amorphous alloys are lower than those of the crystalline transition metals, which they contain. However the direct effect of the structural disorder on the moments is very small. This points out the importance of chemical instead of structural disorder. The reduction is least in B-based glass and highest in P-based glass. The observed moments on TM-M glasses can approximately fitted to a formula

$$\mu = \frac{\mu_{TM} C_{TM} - C_B - 2C_{si} 3C_p}{C_{Tm}} \quad , \tag{3.49}$$

where μ_{TM} is the magnetic moment of TM-M atoms, taken as 2.6, 1.6 and 0.6 respectively in Bohr magneton for Fe, Co and Ni, C's are respective concentrations. This clearly demonstrates the charge transfer from metalloid to d-band of transition metal and seems to suggest that 1, 2 or 3 electrons are transferred from each of B, Si (C, Ge) or P atom. The relative number of electrons donated can be listed as $-P_{13}C_7\rangle - S_{15}B_{10}\rangle - P_{16}B_6Al_3\rangle - P_{14}B_6\rangle - Si_9B_{13}\rangle - B_{20}$ based on the relative magnitudes of M_s. Amorphous alloys are rather poor conductors but their 3d-electrons are just as "itinerant" as in the crystalline transition metal alloys. Only itinerant exchange between 3d moments is of importance in the metal-metalloid alloys. Itinerant exchange arises because single site exchange taken together with the inter site electron hopping terms produce a correlation between moments on different sites. This mechanism depends on the band structure and can lead to ferromagnetism, antiferromagnetism or complex spin arrangements. The theoretical treatment of spin ordering in amorphous solids is a much

more difficult problem than the regular crystalline lattices and has not been satisfactorily solved. If the molecular field approximation (MFA) is used, even though its use is doubtful, the paramagnetic Curie temperature can be expressed as

$$T = \frac{2S(S+1)}{3k} \times \sum_{ij} j_{ij} \qquad (3.50)$$

Where S is the spin number k is the Boltzmann's constant and j_{ij} is the exchange interaction between atoms at the position r_i and r_j and can be expressed in terms of the radial distribution function .

In first case, a unique constant exchange interaction between the magnetic atoms is assumed and the amorphous nature of the alloy is taken into account by calculating a random distribution of he local anisotropy field [3.17]. In the second approach to treat this problem a distribution of exchange integrals is assumed in order to reflect the structural fluctuation in the amorphous alloy [3.18]. Both approaches predict that the M vs. T curve will fall below that for the crystalline counter part. The first model however predicts that amorphous alloys should exhibit a structure less Mössbauer spectrum, contrary to the observed spectra. Thus the second approach is preferred of the various theories based on the molecular approach (MFA) and mean field theories.

3.4.1 Low Temperature Behavior of M_s of Amorphous Ribbons

The mean field theories do not account for local magnetic excitations and thus can not provide an accurate description of the low temperature behavior of the magnetic properties. In the quasicrystalline approximation and the long wavelength limit, the spin-wave energy can be expressed by Keffer[3.19].

$$E_k = E_0 + DK^2 + FK^4 + \text{----------} , \qquad (3.51)$$

where K is the wave vector of the spin-wave and D and F are the spin stiffness constants. The presence of spin waves gives rise to a reduction of the average magnetization, leading to a temperature dependence of the from

$$M_s(T) = M_s(o)\left[1 - BT^{\frac{3}{2}} - CT^{\frac{3}{2}} + ...\right] \quad , \tag{3.52}$$

where $M_s(0)$ is the saturation moment. The coefficients B and C are related to the spin-wave Stiffness constant D by

$$B = \xi\left(\frac{3}{2}\right)\left(\frac{g\mu_B}{M_s(0)}\right)\left(\frac{K_B}{4\pi D}\right)^{\frac{3}{2}} \text{ and} \tag{3.53}$$

$$C = \frac{3}{4}\pi\left\langle r^2\right\rangle\xi\left(\frac{5}{2}\right)\left(\frac{g\mu_B}{M_s(o)}\right)\left(\frac{K_B}{4\pi D}\right)^{\frac{5}{2}} \quad , \tag{3.54}$$

where g is the g-factor (~ 2.1), μ is the Bohr magneton , $\xi\left(\frac{3}{2}\right) = 2.612$ and $\xi\left(\frac{5}{2}\right) = 1.341$ are zeta functions and $\left\langle r^2\right\rangle$ represents the average mean-square range of the exchange interaction . D is directly proportional to the exchange constants. The $T^{\frac{3}{2}}$ terms comes from quadratic dependence of spin-wave vector on wave vector. With increasing exchange strength, the slope of $M_s(T)$ versus $T^{\frac{3}{2}}$ decrease are expected in experimental results of alloys with increasing T_c.

3.4.2 High Temperature Behaviour of M_s of Nanocrystalline Amorphous Ribbons

The overall temperature behavior of reduced magnetization $m = \frac{M_s(T)}{M_s(0)}$ in TM-M glass goes to zero quite sharply at critical temperature T_c and in many glasses the phase transition is as sharp as in crystalline system. Near T_c ,

$$M_s(T) = (T_c - T)^{\beta} \quad , \tag{3.55}$$

where the β is a critical exponent. At intermediate temperature there is flattening, which is found in almost all TM-M glasses studied . The effect of high temperature has been

treated in two different approaches. The first approach is given by Harris *et.al.*[3.20] . He considers a constant exchange interaction between magnetic atoms and a random distribution of the local anisotropy field which changes with temperature . The other approach is to consider a distribution of exchange integral in order to take into account the fluctuation in the amorphous alloys as taken by Handrich [3.18]. Both the approach are unrealistic and infact no rigorous theory of high temperature behavior for amorphous materials has been developed. We have determined the experimental power law from the temperature variation of magnetization in the high temperature range.

Chapter-4

Experimental Details

4.1 The Differential Thermal Analysis

4.1.1 Introduction

The technique of differential thermal analysis is an important tool to study the structural change occurring both in solid and liquid materials under heat treatment. These changes may be due to dehydration transition from one crystalline variety to another, destruction of crystalline lattice, oxidation, decomposition etc. The principle of differential thermal analysis (DTA) consists in measuring the heat changes associated with the physical or chemical changes occurring when a standard substance is gradually heated. This technique has been used in determining the glass transition temperature (T_g) and crystallization temperature ($T_{x)}$ of our nanocrystalline soft magnetic material. The glass transition temperature T_g is defined as the temperature at which the alloy passes from the solid to the liquid state .For our purposes it is sufficient to describe T_g as the temperature at which atomic mobility is great enough to allow diffusive atomic rearrangement to occur in a matter of minutes. The crystallization temperature T_x defined as the temperature at which crystallization occurs with long range ordering and is usually determined by DTA technique by heating at the rate of $\approx 10°C/\min$. The DTA technique has been used in determining T_g and T_x of our nanocrystalline amorphous soft magnetic material with the compositions

$Fe_{73.5}Cu_1Nb_3Si_{13.5}B_9$.

4.1.2 The Principle of Differential Thermal Analysis

The DTA technique was first suggest by Le Chatelier [4.1] in 1887 and was applied to the study of clays and ceramics. DTA is the process of accurately measuring the difference between a thermocouple embedded in a sample and a thermocouple in a standard

temperature inert material such as aluminium oxide while both are being heated at uniform rate.

These differences of temperature arise due to the phase transitions or chemical reactions in the sample involving the evolution of heat or absorption of heat. The exothermic and endothermic reactions are generally shown in the DTA trace as positive and negative deviations respectively from a base line. So DTA gives a continuous thermal record of reactions occurring in a sample. When a sample and reference substance are heated or cooled at a constant rate under identical environment, their temperature differences are measured as a function of time or temperature as shown by the curve in Fig. 4.1(a) and fig. 4.2(b). The temperature of the reference substance, which is thermally inactive, rises uniformly when heated, while the temperature of a sample changes anomalously when there is a physical and chemical change of the active specimen at a particular temperature. When there is an exothermic reaction there is a peak in the temperature versus time curve, heat supplied from outside is consumed by the reaction. And when the reaction is over, the sample temperature is different from the ambient, and it rises rapidly to catch it up, and then it begins to change uniformly. The temperature difference ΔT is detected, amplified and recorded by a peak as shown in Fig. 4.1(a). The temperature in the sample holder is measured by a thermo-couple, the signal of which is compensated for the ambient temperature and fed to the temperature controller. This signal is compared with the program signal and the voltage impressed to the furnace is adjusted. Thus the sample and reference substance are heated or cooled at a desired rate. The temperature in the sample holder is digitally displayed on the DTA – 50 (Differential Thermal Analyzer, Shimadzu Corporation, Kyoto, Japan) and is also recorded on the recorder.

4.1.3 Apparatus

The apparatus of the differential thermal analysis consists of a thin walled refractory specimen holder made of sintered alumina with two adjacent cubical compartments of exactly the same size, 1 cm in length, as shown in fig. 4.2 of which one is for the inert reference material and the other for the test material. The compartments are

separated by a 1 mm wall .The specimen holder is placed in the cavity of the heating block, which is operated in the center of the cylindrical refractory tube of an electrical furnace. This supplies a uniform heating rate. The furnace (9″× 6″× 9″ deep) is peaked with calcined china clay. The input of current into the furnace is secured through the secondary of a variable transformer, which controls the current. Fine chromelalumel wires (28 gauge) are used for thermocouples. A cold junction is used for thermocouples leads and the e.m.f is recorded almost continuously, while the temperature of the inert material is measured at 3 minutes interval.

It is essential to use perfectly dry materials, as otherwise errors will be introduced in the analysis. Approximately 0.1gm anhydrous alumina is used in the reference cup and the sample weight varies over a range 0.05 to 0.125 gm; depending on there packed density. An average heating rate of 10^0 C per minute of the furnace is maintained which gave satisfactory results in most cases. A block diagram of DTA is shown in Fig. 4.3. The thermal analysis runs generally for 1 to 1.5 hrs. Thermal analysis curves are obtained by plotting heating temperature and the difference between the temperatures of the test and reference substances. From these plots the reaction temperature could be determined. Under standard conditions of the experiment, characteristics curves for different composition $Fe_{73.5}\,Cu_1\,Nb_3\,Si_{13.5}\,B_9$ amorphous ribbon were obtained. A sharp exothermic peak indicates Glass transition and crystallization temperature points, usually. Exothermic peaks similarly give the temperatures of decomposition of phases and in cases typical endothermic curves afford useful information about the structural changes taking place in the compound.

All experiments are run at atmospheric pressure in a continuous flow of a purified inert gas usually argon, Nitrogen or helium. Gases are normally purged into the furnace chamber at the lower and through a purification train in which oxygen and water are removed by heated copper wool and exhausted from the top into a condensed trap for collecting the condensable volatile products.

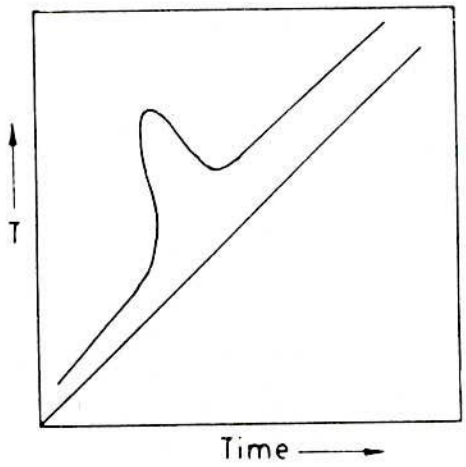

Fig. 4.1(a) Heating curve of sample and reference substance

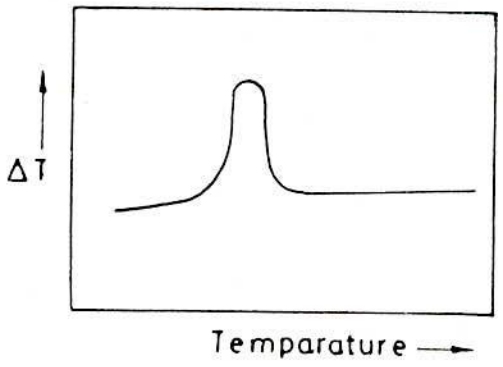

Fig. 4.1(b) DTA curve

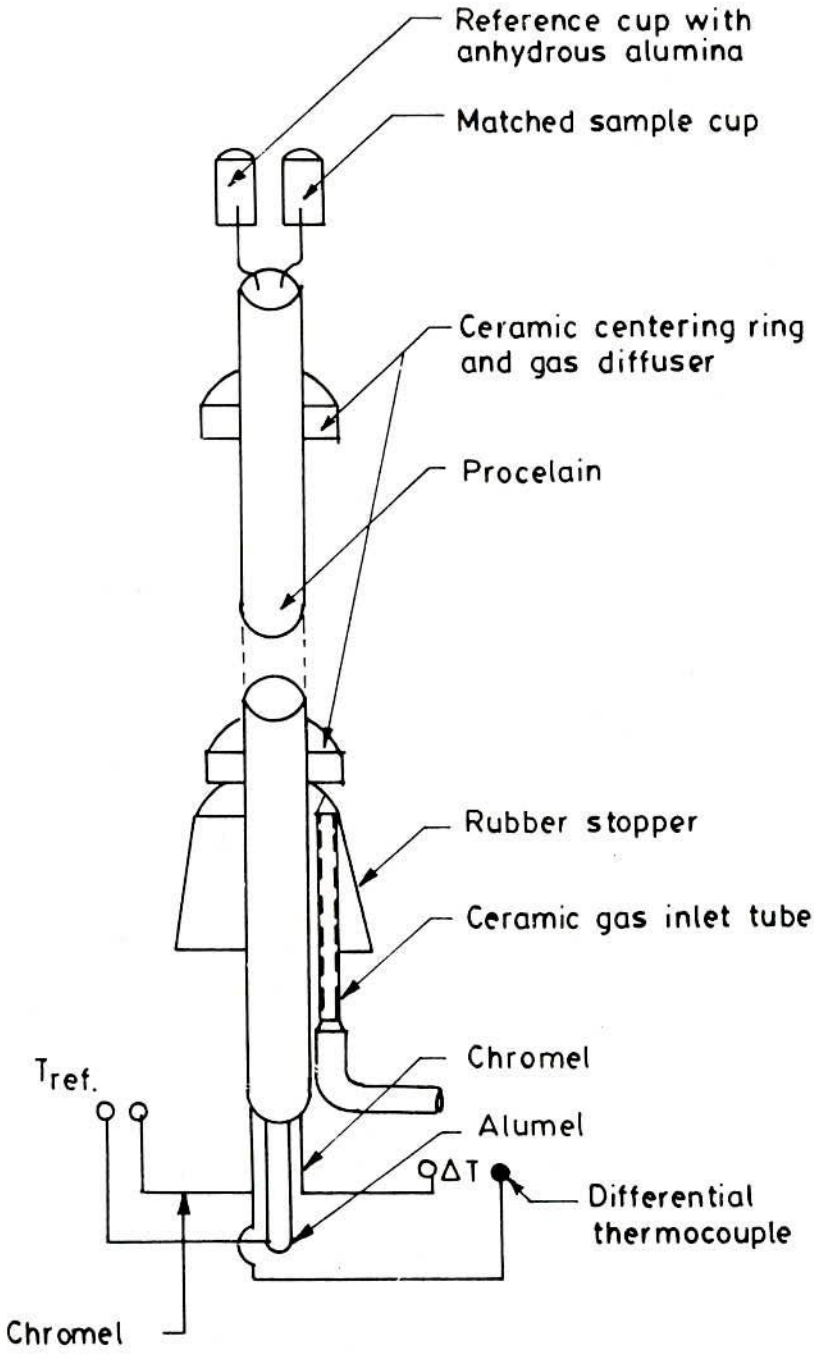

Fig. 4.2. DTA Thermocouple assembly

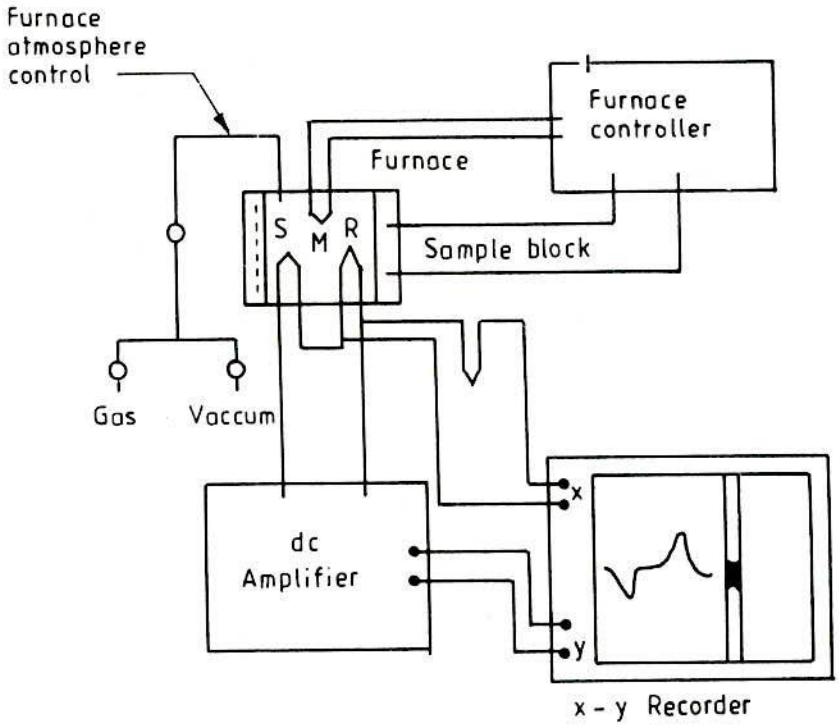

Fig.-4.3. Block diagram of a differential analysis equipment, (S) sample thermocouple, (R) reference thermocouple, (M) monitor thermocouple.

4.2 Experimental Techniques for X-ray Diffraction

X-ray diffraction (XRD) is a versatile non-destructive analytical technique for identification and quantitative determination of various crystalline phases of powdered or solid samples of any compound. A PHILIPS X´Pert PRO X-ray diffraction system was used to get X-ray data for the samples at the Magnetic Material Division, Atomic Energy centre, Dhaka, which is a sophisticated X-ray diffractometer installed very recently, shown in Fig. 4.4 and Fig. 4.5. The powder diffraction technique was used with a primary beam power of 40 kV and 30mA for Cu radiation. A nickel filter was used to reduce Cu-K_β radiation and finally Cu-K_α radiation was only used as the primary beam. A (θ - 2θ) scan was taken from 20^0 to 120^0 to get possible fundamental peaks of the sample with the sampling pitch of 0.02^0 and time for each step data collection was 1.0 sec. Both the programmable divergence and receiving slits were used to control the irradiated beam area and output intensity from the sample, respectively. An anti scatter slit was used just after the sample holder to reduce air scattering. Two solar stills were used just after the tube and in front of the detector to get parallel beam only. All the data of the samples were stored in the computer memory and later analyzed them using computer soft ware "X´PERT HIGHSCORE''.

For each set of composition, ribbons are cut into several pieces, each of length 20 mm. Heat treatment was performed on the amorphous ribbons using a carbolite furnace, where each piece of ribbon was wrapped by aluminum foil separately. After heat treatment, samples were removed from the aluminum foil carefully and kept separately for XRD experiment. For XRD experiment each sample was set on a glass slide and fixed the sample by putting adhesive tape at the two ends of the sample.

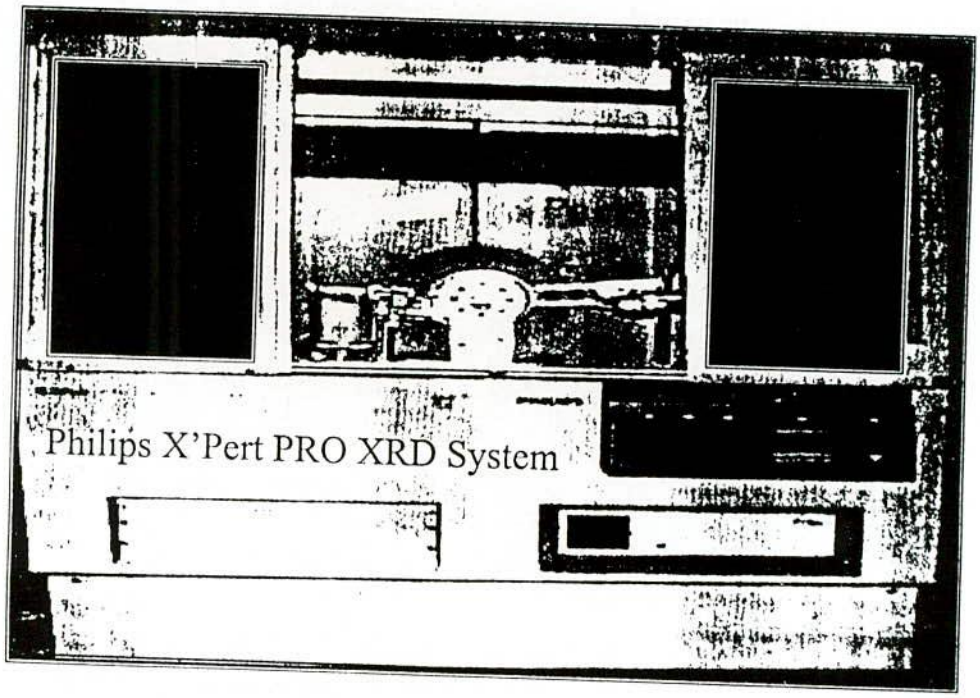

Fig. 4.4 Phlips (PW 3040) X' Pert PRO XRD system

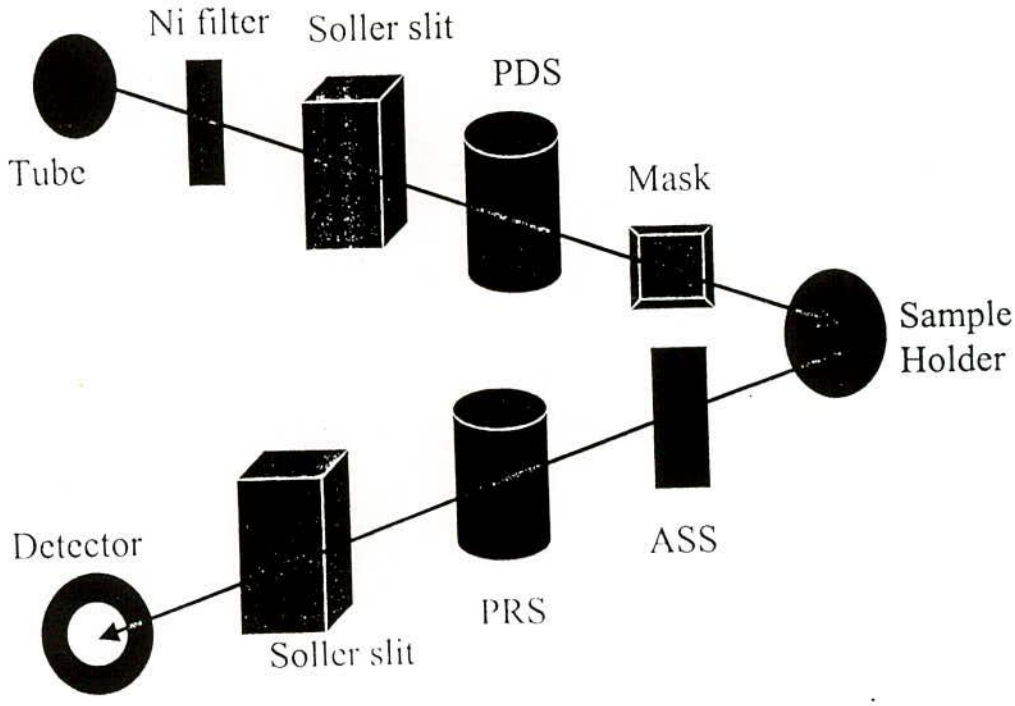

Fig. 4.5 Block diagram of Phlips (PW 3040) X' Pert PRO XRD system

4.2.1 Interpretation of the XRD Data

The XRD data consisting of θ_{hkl} and d_{hkl} values corresponding to the different following structural information of the nanocrystalline ribbon sample.

a) Identification of phases.

b) Lattice parameter determination.

c) Average grain size determination

d) Si - content determination in nanograins.

4.2.1 (a) Identification of phases

X-ray diffractometer has become a very popular and useful instrument for routine X-ray analysis of ribbon samples. In fact the diffractometric technique is often preferred to Debye-Scherrer technique owing to its several inherent merits. The most striking difference between the two methods is in the use of different intensity detection and measuring devices. XRD pattern of as-cast indicates just amorphous pattern of said composition. The XRD patterns were identified as bcc α-Fe-Si solid solution, which were developed on the amorphous ribbon after heat treatment. The peak pattern was observed for all the samples at different heat treatment temperatures indicating the bcc α-Fe-Si phase, which was developed on amorphous ribbons after heat treatment. Present experiment revels that 450^0C is not sufficient temperature to start forming of crystalline nanograins of bcc Fe-Si on the amorphous ribbon of said alloy composition.

4.2.1(b) Lattice Parameter Determination

Lattice parameter of crystalline bcc Fe – Si nanograins was determined for all the two different amorphous compositions at different heat treatment temperatures. Normally, lattice parameter of an alloy composition is determined by the Debye-Scherrer method after extrapolation of the curve. In this method, at least five fundamental reflections are required to determine lattice parameter. In the present case, only one reflection (110) is prominent in all XRD patterns and we would like to understand how the value of lattice parameter

changes with annealing temperature. We have, therefore, determined the lattice parameter using only that particular reflection using equation $2d\sin\theta = \lambda$ and $a_0 = d\sqrt{2}$, where $\lambda = 1.54178\,\overset{0}{A}$ for Cu-k_α radiation and a_0 is the determined lattice parameter with in an error estimated to be $\pm 0.0001\,\overset{0}{A}$.

4.2.1 (c) Grain Size Determination

The main aim of the present study was to determine the nanocrystalline grain size for all the heat treatment samples of the alloy composition which was determined using Scherrer method. The XRD pattern of $[110]$ reflection for different steps of heat treatment temperature of the alloy composition was used to calculate grain size. Grain size was determined using the formula,

$$D_g = \frac{0.9\lambda}{\beta\cos\theta} \quad , \tag{4.1}$$

where $\lambda = 1.54178\,\overset{0}{A}$ for Cu-k_α radiation and $\beta = \text{FWHM}$ (full width at half maximum) of the peak in radian . Considering β in degree we get the relation,

$$D_g = \frac{79.5}{\beta\cos\theta} \tag{4.2}$$

All the values of grain size for every steps of heat treatment temperature of the alloy composition were determined. The FWHM of the peak is large at the initial temperature and with the increase of heat treatment temperature the value of FWHM getting smaller.

4.2.1 (d) Si - Content in Nanograins

Crystalline nanograins were formed on the ribbon in the process of heat treatment with the alloy composition of Fe- Si. It is, therefore important to determine the concentration of Fe and Si in the nanograin. As because the alloy nanograins are consists of Fe and Si and we have experimentally determined the lattice parameter of the alloy

nanograin for the two compositions at different temperatures. It is easy to calculate the Si content in the nanograins from Pearsons hand book relationship [4.2]. From the relationship, we have constructed a simple equation to calculate Si content from lattice parameter. The equation is

$$X = \frac{(a_0 - 2.8812)}{0.0022} \qquad (4.3)$$

where X is at.% Si in the nanograins, a_0 is the determined lattice parameter of nanograins. Si contents for the nanograins develop during the isothermal annealing at various temperatures have been calculated.

4.3 Experimental Determination of Complex Permeability

4.3.1 Real and Imaginary Components of Complex Permeability

Determinations of permeability normally involve the measurements of the change in self inductance of a coil in the presence of magnetic core. The behavior of a self inductance can now be described as follows. If we have an ideal loss less air coil of inductance L_0 , on insertion of magnetic core with permeability μ, the inductance became μL_0 .The complex impendence Z of this coil can then be expressed as

$$\begin{aligned} Z &= R + iX = i\omega L_o \mu \\ &= i\omega L_o (\mu' - i\mu'') \\ &= \omega L_o \mu'' + i\omega L_o \mu' \end{aligned} \qquad (4.4)$$

Where the resistive part is

$$R = \omega L_0 \mu'' \quad , \qquad (4.5)$$

and the reactive part is

$$X = \omega L_0 \mu' \qquad (4.6)$$

The r.f permeability can be derived from the complex impendence of a coil in equation (4.4). The core is taken in the toroidal form to avoid demagnetizing effects. The quantity L_0 is described geometrically as shown in section 4.3.3.

4.3.2 Preparation of the Samples for Complex Permeability

The amorphous ribbons were wound in to toroidal cores having outer and inner diameters 13 to 15 mm and with the ratio of outer and inner diameters always kept less than 1.2 in order to improve the homogeneity of the applied field, as also to reduce the possibility of an inhomogeneous inductance response. Toroids were wound with 10 turns around to apply ac magnetic fields over a wide range of amplitudes. While measuring the permeability of the amorphous ribbon cores at high frequency, the high electric resistance of these materials generally precludes the trouble some skin effect found in ribbons. However, the cross-section of the amorphous ribbon core to be measured may have to be kept small in order to avoid dimensional resonance phenomena .To avoid an increase in resistance owing to skin effect, braided copper wire is used at frequencies higher than 100 kHz.

At higher frequencies the capacitance arising from winding gives inaccurate values of R and L_s. It is, therefore, necessary to keep the capacitance of the winding as low as possible. Frequency response characteristics were then investigated on these ring shaped specimens as a function of frequency.

4.3.3 Frequency Characteristics of Nanocrystalline Materials

The frequency characteristics of the amorphous ribbons samples i.e the permeability spectra, were investigated using an impedance analyzer (LCR bridge), Wayne Kerr 3255B model, Atomic energy Centre, Dhaka. The measurement of inductances were taken in the frequency range 1kHz to 500 kHz. The values of measured parameters obtained

as a function of frequency and the real and imaginary parts of permeability and the loss factor μ' is calculated by using the following formula.

$$L_s = L_0 \mu'$$

$$\mu' = \frac{L_s}{L_0} \qquad (4.7)$$

and

$$\tan\delta = \frac{\mu''}{\mu'} \quad , \qquad (4.8)$$

$$\mu'' = \mu' \tan\delta$$

where L_s is the self-inductance of the sample core and

$$L_0 = \frac{\mu_0 N^2 S}{d} \quad , \qquad (4.9)$$

where L_0 is the inductance of the winding coil without the sample core , N is the number of turns of coil and S is the area of cross section as given below

$$S = dh \ , \qquad (4.10)$$

where

$$d = \frac{d_2 - d_1}{2} \qquad \text{and h is height.} \qquad (4.11)$$

and $\bar{d}$ is the mean diameter of the sample given as follows :

$$\bar{d} = \frac{d_2 + d_1}{2} \qquad (4.12)$$

The relative quality factor is determined for the ratio $\frac{\mu'}{\tan\delta}$.

4.4 Experimental Set-up for Measurements of Magnetization

4.4.1 The Principles of Vibrating Sample Magnetometer

All magnetization measurements have been made on EG and G Princeton Applied Research Co. make vibrating sample magnetometer (VSM) [4.3-4.4]. The principle of VSM is as follows: When the sample of a magnetic material is placed in a uniform magnetic field , a dipole moment proportional to the product of the sample susceptibility times the applied field is induced in the sample . If the sample is made to under go a sinusoidal motion, an electrical signal is induced in suitably located stationary pick-up coils. This signal which is at the vibrating frequency is proportional to the magnetic moment, vibration amplitude and vibration frequency. In order to obtain the reading of the moment only, a capacitor is made to generate another signal for comparison, which varies in its moment, vibration amplitudes and vibration frequency in the same manner as does the signal from the pick-up coil. These two signals are applied to the inputs of a differential amplifier, and because the differential amplifier passes only difference between the two signals, the effect of vibration amplitude and frequency changes are cancelled. Thus only the moment determines the amplitude of the signal at the output of the differential amplifier. This signal is in turn applied to a lock-in amplifier, where it is compared with the reference signal which is at its internal oscillator frequency and is also applied to the transducer which oscillates the sample rod. Thus the output of the Lock-in amplifier is proportional to the magnetic moment of the sample only avoiding any noise of frequency other that of the signal. The Lock-in action yields an accuracy of 0.05% of full scale. The absolute accuracy of this system is better than 2% and reproducibility is better than 1%. Least measurable moment is $5X10^{-4}$ emu.

Variable magnetic field is achieved with a Newport Electromagnet Typen 177 with 17.7 cm diameter pole pieces .The magnet is mounted on graduated rotating base. The standard model is modified to provided an adjustable pole gap in order that the highest possible field strength is available. The field can be varied from 0 to 9 kG. The field is measured directly by using Hall probe.

4.4.2 Mechanical Design of the V.S.M.

The various mechanical parts of the magnetometer are shown in the Figure 4.6. The base B of the V.S.M. is a circular brass plate of 8mm thickness and 250mm diameter. A brass tube T of 25mm outer diameter and 0.5 mm thickness runs normally through the base such that the axis of the tube and the center of the plate coincide. The base and the tube are joined together by soft solder. The tube extends 60mm upward and 24mm downward from the base. There is a vacuum port on the lower part of the tube 120mm below.

Electrical connections from the audio amplifier to the speaker and from the reference coil system to the phase-shifter are taken via the perspex feed-through. By connecting the vacuum port of the tube T to a vacuum pump the sample environment can be changed. The speaker SP is fitted 25mm above the tube T with the help of our brass stands. The lower ends of the stands are screwed to base plate while the rim of the speaker is screwed on the tops of the strands. The speaker has a circular hole of 10mm diameter along the axis of it. An aluminium disc having female threads in it is fitted to the paper cone with araldite. The aluminium connector having male threads on it and attached to the drive rod assembly fits in the aluminium disc and thus the drive rod assembly is coupled to the speaker. The drive rod assembly consists of two detachable parts which are joined together by means of aluminium threaded connectors. Each part is a thin pyrex glass tubing of 4mm diameter. The upper part has a small permanent magnet P situated 100mm below the aluminium connector attached to it. At the lower end of the drive rod assembly a perspex sample holder having quite thin wall can be fitted tightly with the sample in it. A few perspex spears are also attached to the driver rod throughout its length. The spacers guide the vibration of the sample only in the vertical direction and stops sidewise vibration or motion. The total length of the drive rod assembly is 920mm up to the base. The lower end of the tube T is joined to a brass extension tube L by a threaded coupling and an O'ring seal. Another thin tube K made of german silver and of 8 mm inner diameter runs through the extension tube L from the coupling point C to about 50mm below the sample position. Above the base there is hollow brass cylinder M of 180 mm length and 130mm inner diameter, having 40mm wide collars at its both ends. The lower collar seats on an O'ring

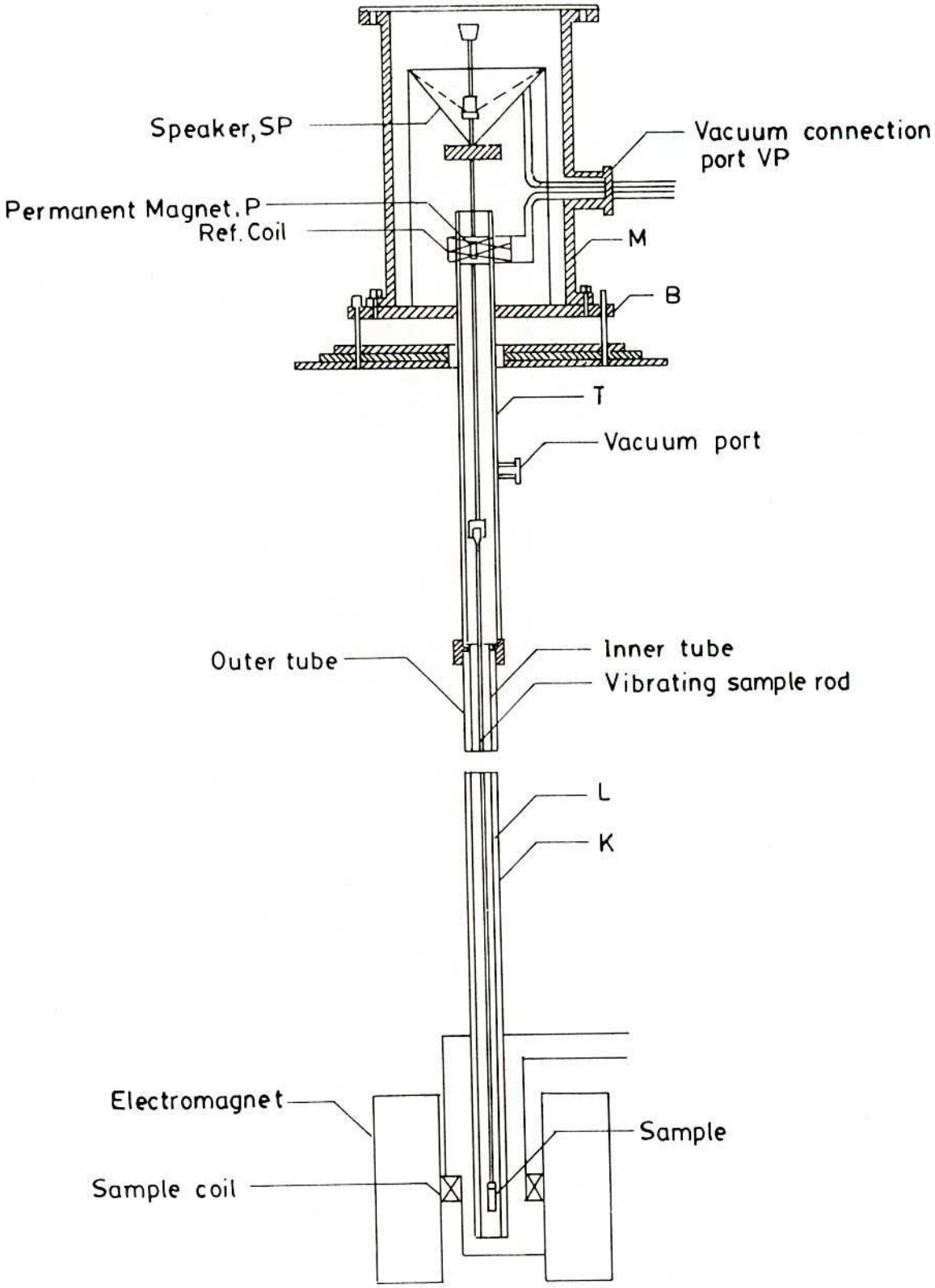

Fig.-4.6. Mechanical construction of the vibrating sample magnetometer.

seal which is situated in a circular groove in the base plate. On the upper collar, there rests an aluminium top N with an O'ring seal. The brass cylinder M has a side port VP. This is again a brass tube of 41mm diameter and 43mm length. The port has a collar at the end away from the cylinder. A perspex vacuum feed through is fitted at its end with O' ring seal. This port is connected to the cylinder by soft solder.

The base plate of the V.S.M. rests on three leveling screws above a brass frame, which in turn rests on an iron angle bridge. The bridge is rigidly fitted to the sidewall of the room. The brass frame is provided with arrangements with the help of which it can be moved in two perpendicular directions in the horizontal plane.

The levelling screws are used to make the drive rod vertical and to put the sample at the center of the pole-gap between the sample coils. The travelling screws can also move up and down the sample.

4.4.3 Electronic Circuits of the V.S.M.

The function of the associated electronic circuits are:

(i) To permit accurate calibration of the signal output obtained from the detection coils .

(ii) To produce a convenient AC output signal which is directly related to the input and which can be recorded.

(iii) To produce sufficient amplification for high sensitivity operation.

The block diagram of the electronic used for the V.S.M. consists of a mechanical vibrator, a sine wave generator, an audio amplifier, a ratio transformer, a phase-shifter, a lock in amplifier, a pick-up coil system, a reference coil system and an electromagnet as shown in Fig. 4.7. The sample magnetized by the electromagnet generates an e.m.f in the pick-up coils PC. The strength of this signal is proportional to the magnetization of the sample. The vibrating permanent magnet also generates an e.m.f. of fixed amplitude in the surrounding reference coils. This signal is stepped down with the help of a ratio transformer

so that its amplitude is equal to that of the sample signal. The two signals are then brought in phase and put to the Lock-in amplifier. The Lock-in amplifier works as a null detector. The ratio transformer reading is calibrated using spherical shape sample S of 99.99% pure nickel.

4.4.3.1 Sensitivity Limits

Limits of sensitivity are determined by signal to noise at the input circuit, where noise is defined as any signal not arising from the magnetic moment of the sample.The major sources of noise are the Johnson noise of the wire used for the pick-up coils, and the magnetic responses of the sample holder, which superimposes undersigned signals in phase with the wanted signal. Use of a minimum mass of weakly diamagnetic material for a sample holder, carefully checked to contain no ferromagnetic impurities, is essential to minimize this coherent noise contribution. Corrections for the small magnetic contribution of the sample holder can then be made by measurements with the sample removed. This correction is much less than the equivalent case with moving coil system. Our standard sample used for calibration was shaped specimens of mass 0.0584gm. The different field susceptibility $\Delta\chi \cong 5\times10^{-10}$ could be observed after synchronous phase detection with bandwidth $\cong 2\times10^{-2}$ cps . The other tests used was small current at 81 Hz or an alternating current 81 Hz passed through the coil which remained stationary.

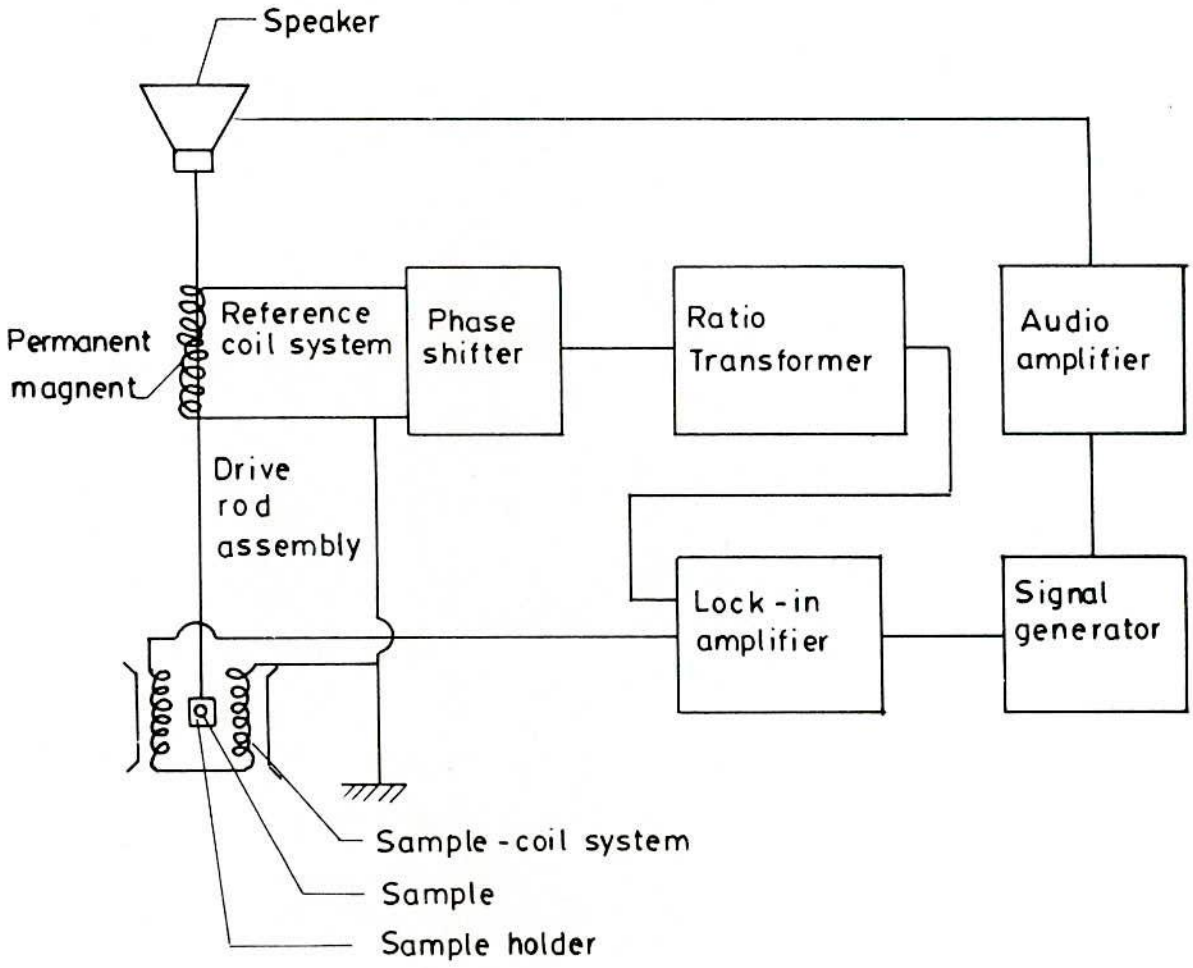

Fig.-4.7. Schematic diagram of the electronic system of the V.S.M.

4.4.3.2 Stability Tests Differential Measurements

With only the Lock-in amplifier and the oscilloscope as a null detector, it was found that the 0.0584 gm Ni-sample signal could be balanced reproducibly. Such that the long time drifts caused by the combined effects of vibration, amplitude changes, and frequency changes in the bridge sample position and other effects were negligible. Chosen synchronous phase detector added differential changes about one-tenth the size that recorded reproducibly.

4.4.3.3 Vibration Amplitude

The pick-to-pick vibration amplitude has been varied from less than 0.1mm up to 1.0mm in order to examine errors caused by amplitude change. Such tests show that the measured magnetic moment varied less than 0.5% over these range of amplitude, although at higher variation of amplitudes, because of the larger signals involved.

4.4.3.4 Image Effects

Image effects were also examined with a small vibrating coil carrying a dc current. The image effect was no grater than ±1% for fields up to 5kG produced in an air gap of 3.6cm.Undoubtedly, there is an image induced in the magnet poles. It appears, however, that when the sample is vibrated, eddy current shielding reduces the effective image vibration.

4.4.3.5 Vibration Frequency

The vibration frequency is not critical. High frequency operation is limited by the driving mechanism and capacitive shunting in the detection coils. Frequencies of 100 Hz or less permit the use of inexpensive components and minimize eddy currents shielding by the vacuum chamber. The measurements are completely independent of eddy currents in the in the surrounding parts, if measurements and calibration are made at the same temperature.

The thickness of conducting parts has been minimized, so that the temperature dependence of penetration depth is less than 1%

4.4.3.6 Vibration Problems

Mechanical coupling between the vibrating system and the fixed detection coils must be avoided. Although the coils are arranged for minimum sensitivity to external vibration, a noticeable background signal is obtained when the vacuum chamber contacts the detection coils. Such mechanical effects are difficult to eliminate electronically, because the spurious background signal has the same frequency as the sample signal and maintains a constant phase difference with respect to the sample signal. Usually the magnetometer and detection coils are both supported by the magnetic coupling, so that some mechanical coupling may be noticed at highest sensitivity.

4.4.4 Calibration of the V.S.M.

There are usually two methods of calibration of a vibrating sample magnetometer (V.S.M)

(i) by using a standard sample and

(ii) by using a coil of small size whose moment can be calculated from the magnitude of the d.c. current through it .

We have calibrated our V.S.M. using a 0.0584 gm spherical sample of 99.99% pure nickel. The sample was made spherical with the help of a sample-shaping device. The saturation magnetic moment of the sample has been calculated using the available data. The ratio transformer reading is obtained by actual measurement from the relation

$$M = K K' \qquad (4.13)$$

where M is magnetic moment , K' is saturation ratio transformer reading and K is V.S.M. calibration constant . But

$$M = m\sigma \quad , \qquad (4.14)$$

where σ is the specific magnetization and m is the mass of the sample . From Equation 4.13 and Equation 4.14 calibration constant is given by

$$K=\frac{m\sigma}{K'} \qquad (4.15)$$

The accuracy of this calibration, however, depends on the reliability of the standard nickel sample; the accuracy of the ratio transformer and the gain of amplifier. The equipment has been operated repeatedly with the same standard sample and stability has been found to be within 1 part in 100.

The absolute accuracy of the instrument depends on the knowledge of the magnetic properties of the calibration standard and reproducibility of the sample position. When the substitution method of calibration is used the major error 1% is introduced by the estimation of standard nickel sample. The relative accuracy of this instrument depends on accurate calibration of the precision resistor divider network. The total error here can be kept less than 0.5 %. A typical calibration curve of magnetic field versus ratio transformer reading is shown in fig. 4.8

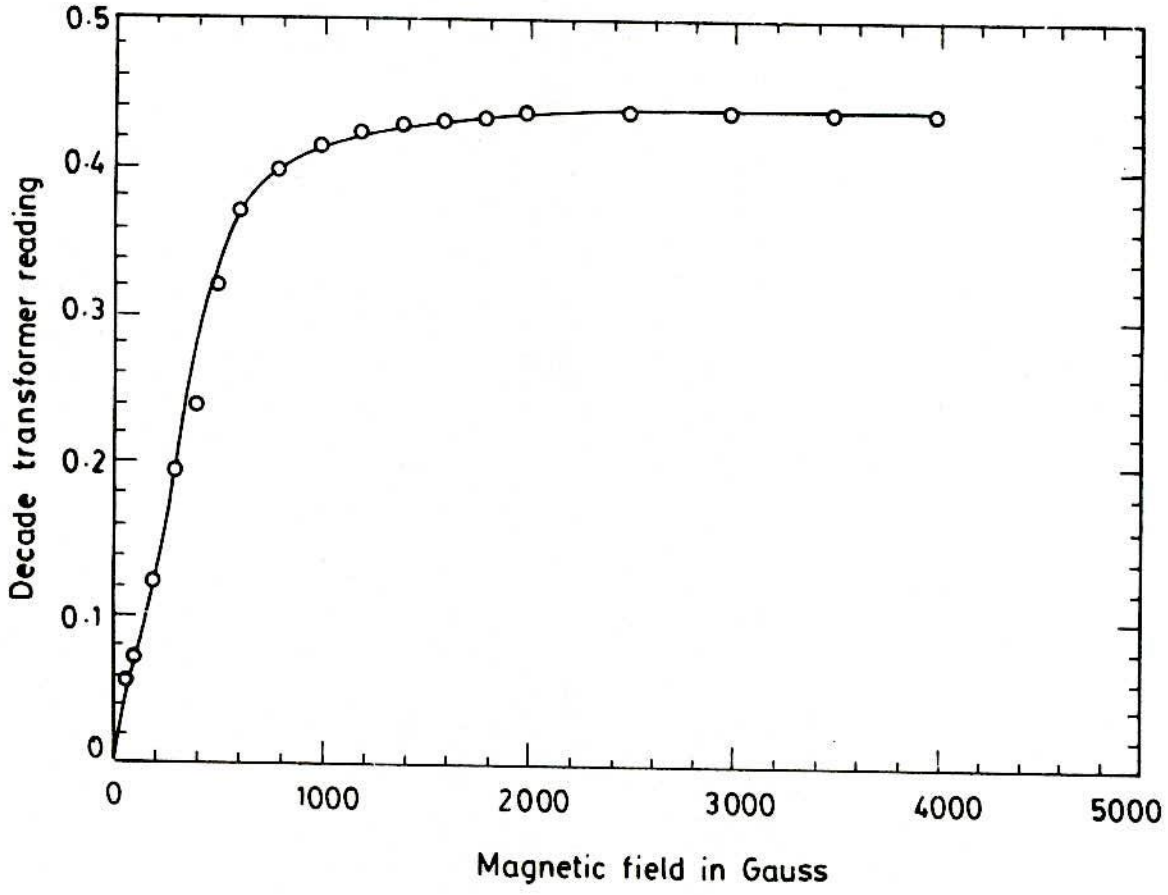

Fig.-4.8. Calibration curve of magnetic field Vs. decade transformer reading (V.S.M.)

Calibration Data:

(i) Reference signal with phase shifter and decade transformer in connection:

$$V_{ref_1} = \frac{1}{0.01} \times \frac{10\mu V}{20} \times 19 = 9.5\mu V \times 100 = 0.95mV \qquad (4.16)$$

(ii) Reference signal with decade transformer in connection:

$$V_{ref_2} = \frac{1}{0.01} \times 11\mu V = 1.1mV \qquad (4.17)$$

(iii) Reference signal with direct connection:

$$V_{ref_3} = 13 \times 0.1mV = 1.3mV \qquad (4.18)$$

- Saturation decade transformer reading for pure Ni at 20° C is given as K= 0.4386.
- Specific magnetization for pure Ni at 20° C is given by $\sigma_s = 54.75 Am^2 / Kg$.
- Mass of the pure Ni-sample m =0.0584 X10^{-3} Kg.
- Magnetic moment M = m σ = 3.1975× 10^{-3} Am^2
- And hence V.S.M. calibration constant is found as

$$K = \frac{m\sigma}{K'} = 7.29 \times 10^{-3} Am^2 \qquad (4.19)$$

4.4.5 High Temperature Magnetization Measurements

Magnetization measurements at temperature above room temperature were done using a high temperature oven assembly (EG and G. Princeton Applied Research Co.). The oven consists of an electrically heated outer tube assembly with vacuum and reflective thermal insulation. The heater consists of an integral bifilar wounding heating coil with a resistance of 80 ohms. The winding is therefore non inducting. The sample holder consists of a quartz tube extension attached to a sample cup. During operation of the high temperature assembly evacuation is accompained by continuous flow of nitrogen gas to eliminate reaction of the sample with oxygen. A chromel-alumel thermocouple is used as a temperature sensor and the highest temperature that can be achieved is 800° C

All the measurements of temperature dependence of magnetization were plotted using LISEIS make X-Y Recorder model LY 18100. The magnetic moment from V.S.M. and temperature from the potential differences in volts taken from panel meter are plotted on X-Y recorder. Magnetic moment can be plotted as a function of time. A graph paper remains struck on an electrically charged plate during the plotting in X and Y scales are calibrated and can be reduced or enlarged as per need.

Chapter-5

Results and Discussions

5.1 Differential Thermal Analysis Results

Nanocrystalline amorphous ribbons prepared by rapid quenching method have been subjected to differential thermal analysis (DTA) using a Shimadzu thermal analyzer. Fig. 5.1 shows the DTA curve of the as-cast $Fe_{73.5}Nb_3Cu_1Si_{13.5}B_9$ with the scan of a thin ribbon produced at a wheel speed of 20 m/s. DTA is a direct and effective technique for analyzing the kinetics of amorphous materials with respect to crystallization processes. It is noticed that three exothermic peaks have appeared at T_{x1}~542°C, T_{x2} ~686°C and the T_{x3} ~ 726°C, the first one corresponds to the crystallization of bcc α-Fe(Si) and the second one are related to the appearance of Fe-B type of phases.

It is observed that the onset of crystallization of bcc Fe(Si) takes place at much lower temperature at least 25°C lower than the peak temperature of 542°C as mentioned before. Therefore the start temperature for crystallization may be assumed to be around 515°C.

The long range ordering of atoms depends on the free energy difference between the crystalline and amorphous state. The change of composition affects the growth kinetics in a complicated way, which can only be determined experimentally. The composition of the alloy affects both the primary and secondary crystallization phases, because the time needed for the constituent atom to have long range order depends on their bond energies [5.1-5.2]. Crystallization phases are affected by the heating rate as well as by composition. The formation of nucleation centers and there growth need to be inhibited to avoid crystallization on the stability of the crystalline amorphous state is thus studied by keeping the heating rate constant. It should be stressed again that good soft magnetic properties require not only a small grain size but at the same time the absence of boron compounds. For the fig. 5.1 the crystallization temperature for primary and secondary crystallization occurs at temperature 542°C and 686°C. Normally Cu and Nb are hardly soluble in bcc Fe phase at 542°C. Rapid quenching technique forces the Cu and Nb elements in to the atomic matrix. At high concentration in α-Fe, which leads to a segregation of Fe and Cu atoms and results in forming Fe-rich and Cu-rich regions. In the Fe-rich region the crystallization temperature is low, so that the nuclei of crystallization can easily be created when the ribbons are thermally

annealed. The behavior of the onset of crystallization with temperature shows that a basic condition for the formation of a typical nanocrystalline structure is the primary crystallization processes before any stable or meta-stable inter metallic phases are formed. The secondary crystallization temperature corresponds to the formation of Fe-B type of phases. As a result of doping of Cu and Nb, ultra fine grains are formed which are homogeneously distributed on the matrix of the residual amorphous phase. This corresponds with the previous finding [5.3].

The primary crystallization peak temperature is quite prominent. This peak is quite broad indicating that the crystallization takes place over a wide range of temperature. Both the peaks, which correspond to release of heat at these temperatures, are associated with the ordering of atoms. By repeating the DTA of the samples after crystallization it was observed that the results are not reproduceable. This is quite expected because the specimens were subjected to irreversible transformations.

Fig- 5.1(a) shows DTA diagrams of $Fe_{73.5}Nb_3Cu_1Si_{13.5}B_9$ amorphous ribbons measured in nitrogen atmosphere with continuous heating at the rate of 10-50°C/min at step of 10°C. Three exothermic peaks in the curve indicate three distinct crystallization temperatures, the first one corresponds to the crystallization of Fe(Si) phase, the 2nd and 3rd are related to the crystallization of iron-boride. It is observed that the crystallization of each phase has occurred over a wide range of temperatures that the peak temperature shifts to higher values with the increasing of heating rate. From these DTA curves crystallization activation energy of Fe(Si) and Fe-B phases can be calculated using heating rate and crystallization peak temperature. The activation energy of crystallization of α-Fe(Si) and Fe-B, (2nd and 3rd peaks) phases have been calculated using Kissinger equation:

$$\ln\left(\frac{\gamma}{T_p^{\,2}}\right) = -\frac{E}{kT_p};$$

Where γ is the heating rate, T_p is the crystallization peak temperature, E is the crystallization energy and k is the Boltzmann constant. The activation energy of α-Fe(Si), 1st peak, 2nd and 3rd peak are found to be 3.21eV, 3.81eV and 6.16eV respectively shown in Fig. 5.1(b,c,d)

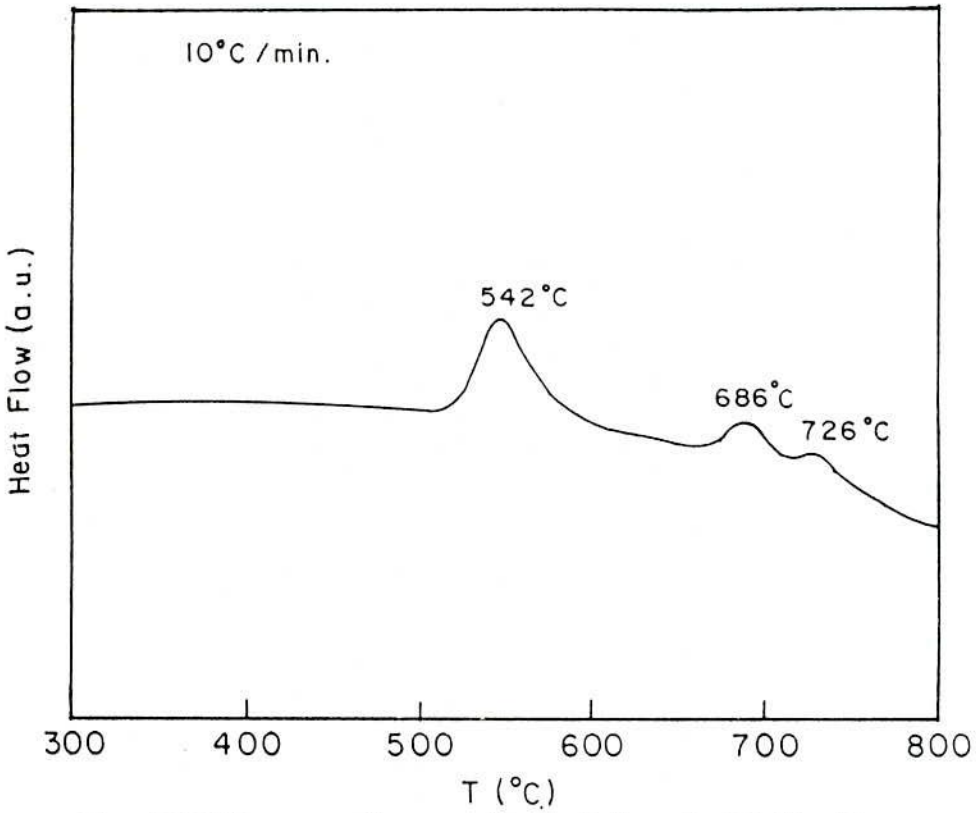

Fig. 5.1 DTA curve of as-cast ribbon of $Fe_{73.5}Cu_1Nb_3Si_{13.5}B_9$

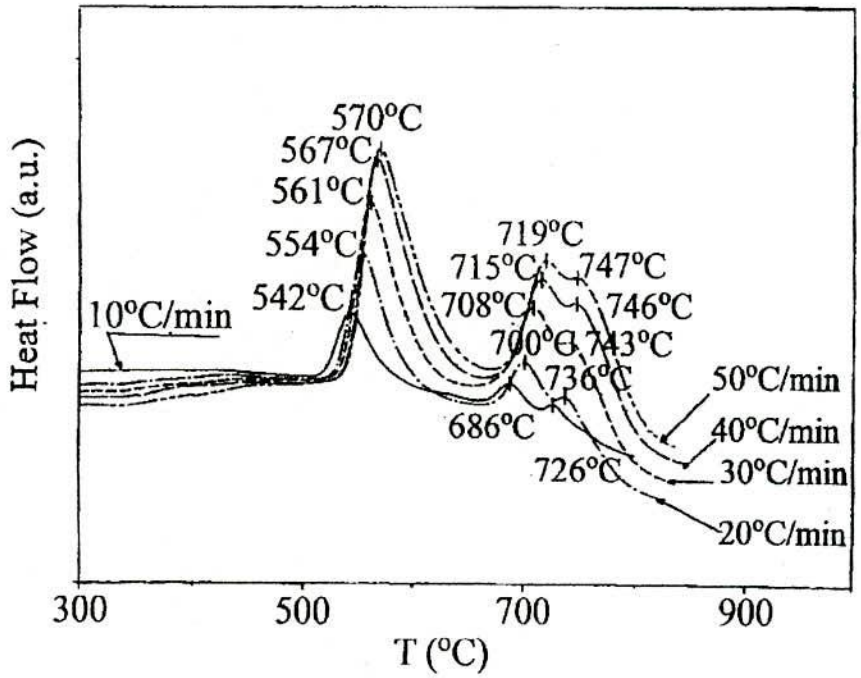

Fig. 5.1 (a) Effects on heating rate on DTA graph of the nanocrystalline amorphose ribbon with composition $Fe_{73.5}Cu_1Nb_3Si_{13.5}B_9$

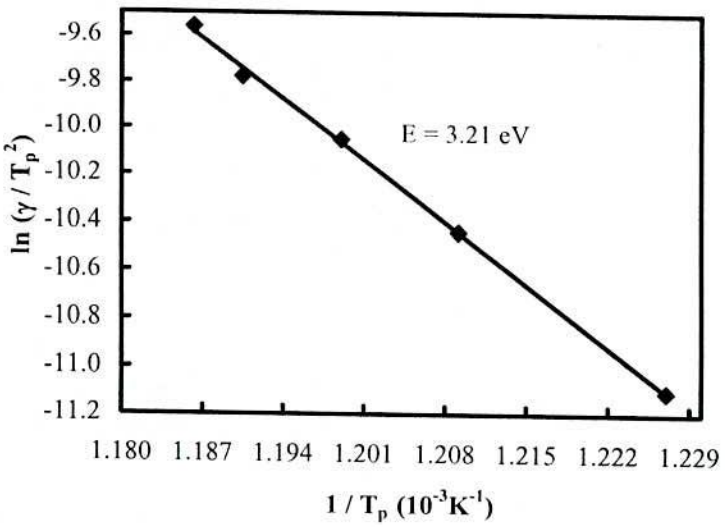

Fig. 5.1 (b)

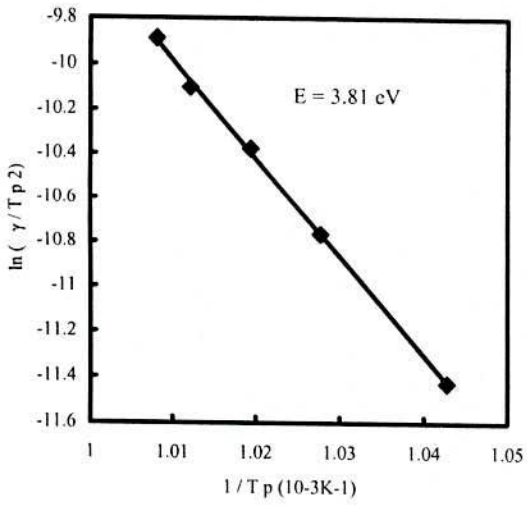

Fig.5.1 (c)

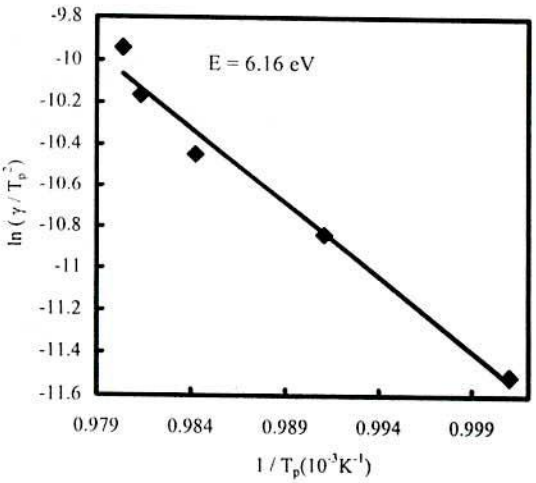

Fig. 5.1 (d)

Fig. 5.1 (b,c,d) Kissinger plots

5.2 XRD Analysis

$Fe_{73.5}Nb_3Cu_1Si_{13.5}B_9$ nanocrystalline ribbon is a typical example of alloys because it exhibits the best soft magnetic properties. However, the appearance of the best properties is sensitive to the alloy's annealing temperature. This nanocrystalline amorphous alloy ribbons were prepared by rapid quenching technique and the amorphous state was confirmed by X-ray diffraction and thermal analysis. In the present work, structure of the $Fe_{73.5}Nb_3Cu_1Si_{13.5}B_9$ alloys, annealed at temperatures from 475°C to 700°C, are investigated by the X-ray diffraction method. Fig. 5.2 is the X-ray diffraction spectra of quenched alloy and the alloy annealed at different temperatures for one hour. In the figure, the indices of the reflecting planes are shown in the parenthesis X-ray diffraction results indicate that no α-Fe phases are present in the alloys annealed below 475°C for 1 hour. When the alloys were annealed at or above 475°C, crystalline phase is developed on the amorphous ribbon.

Fig. 5.3 shows typical XRD patterns of bcc α-Fe(Si) phase for the samples of composition $Fe_{73.5}Nb_3Cu_1Si_{13.5}B_9$ after heat treatment (1hour) at different temperatures. Pattern of T_a = 475°C indicates the amorphous nature after heat treatment the sample 475°C for 1 hour. Pattern of T_a = 500°C indicates a clear bcc α-Fe(Si) of said composition after heat treatment at 500°C for 1 hour. The same pattern was observed for all the samples at different heat treatment temperatures indicating the bcc α-Fe(Si) phase, which was developed on amorphous ribbons after heat treatment. Present experiment reveals that 475°C is not sufficient heat treatment temperature to start forming of crystalline nanograins of bcc Fe-Si on the amorphous ribbon of said alloy composition. Moreover, the bcc Fe phase is a unique crystalline of the alloys annealed at 475 – 700°C, the variation of intensity of the diffraction lines in patterns obtained under the same conditions, reveals that the peak of the bcc Fe phase in the alloys is increased with increasing of the annealing temperature of the crystalline nanograins of bcc Fe-Si phase. All the results of θ, d-values, FWHM at different annealing temperatures of composition are listed in Table-5.1. Rapid quenching technique forces the Cu and Nb elements to solute at high concentration in α-Fe, which leads to a

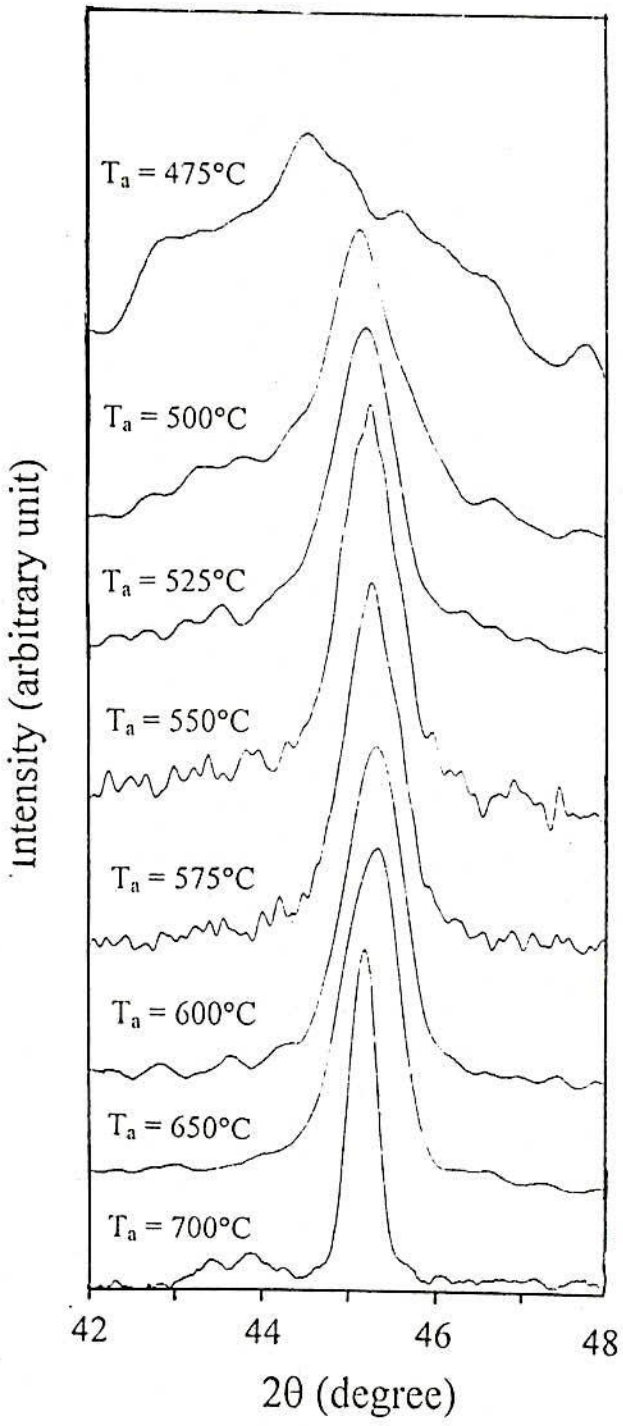

Fig. 5.2 X-ray diffraction (XRD) patterns of 110 reflection for different steps of heat treatment temperatures of the ribbon composition of $Fe_{73.5}Cu_1Nb_3Si_{13.5}B_9$

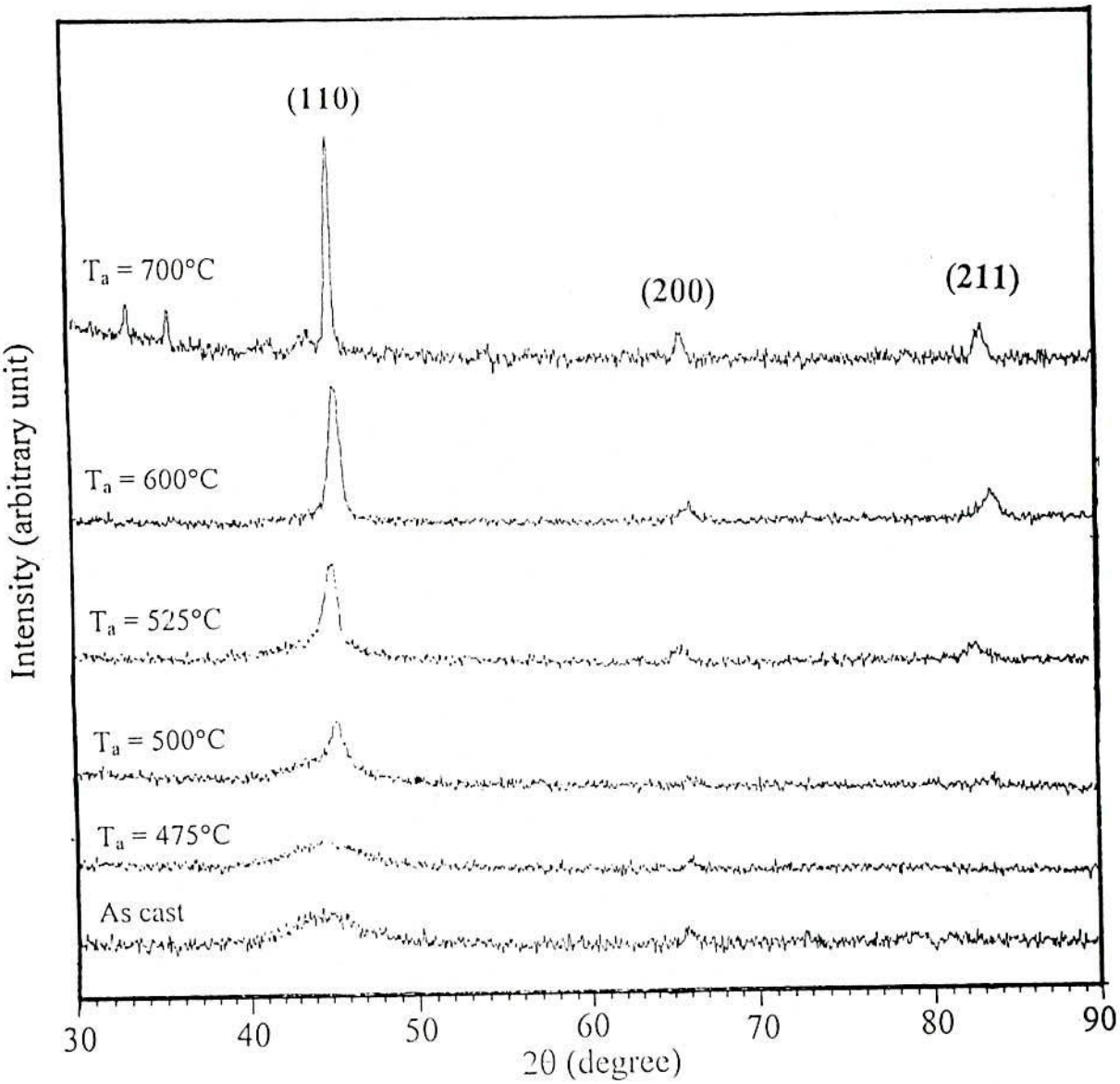

Fig. 5.3 X-ray different spectra of $Fe_{73.5}Cu_1Nb_3Si_{13.5}B_9$ alloys of as-cast annealed at different heat treatment temperatures

segregation of Fe and Cu atoms and results in forming Fe-rich and Cu-rich regions. In the Fe-rich regions the crystallization temperature is low, so that crystallization nuclei are very easy to be created when the ribbon being thermally annealed. The presence of Nb, however, creates around the α-Fe Nb-rich regions with higher crystallization temperature, which suppress the growth of the grains depends on the annealing time. Fig. 5.4 shows typical XRD patterns of bcc α-Fe (Si) phase for the sample of $Fe_{73.5}Nb_3Cu_1Si_{13.5}B_9$ annealed at T_a = 555°C with different annealing time. Thus the crystallization peak intensity slightly shift with increasing annealing time in the ribbon. It is also surprising remark that the peak intensity increases with increasing annealing time. It was also observed from the X-ray spectra that the onset of crystallization takes place within 3 minutes of annealing at 555°C with the manifestation of sharp peak, corresponding to the crystalline phase. Fe-Si phase formation for different annealing time of composition is listed in Table-5.2.

5.2.1 Lattice Parameter Determination

Lattice parameter of crystalline bcc Fe-Si nanograins was determined at different annealing temperatures. Normally, lattice parameter of an alloy composition is determined by the Debye-Scherrer method after extrapolation of the curve. Generally for an accurate determination of the lattice parameter, a number of fundamental peaks are required but in this type of tailored materials upon crystallization only major fundamental peak (110) is used calculation of a_0. We have, therefore, determined the lattice parameter using only that particular reflection using equation $2d \sin\theta = \lambda$ and $a_o = d\sqrt{2}$, where $\lambda = 1.54178\ \text{Å}$ for Cu-k_α radiation and a_o is the determined lattice parameter of the nanograins. For every steps of annealing temperature lattice parameter was determined with in an error estimated to be $\pm 0.0001\ \text{Å}$ and all the values are listed in Table-5.1. Fig. 5.5 shows the lattice parameter of the bcc Fe-Si phase versus annealing temperature for the alloys. The Lattice parameter of the bcc Fe-Si phase decreases with T_a increasing annealing temperature up to 675°C, again the value of

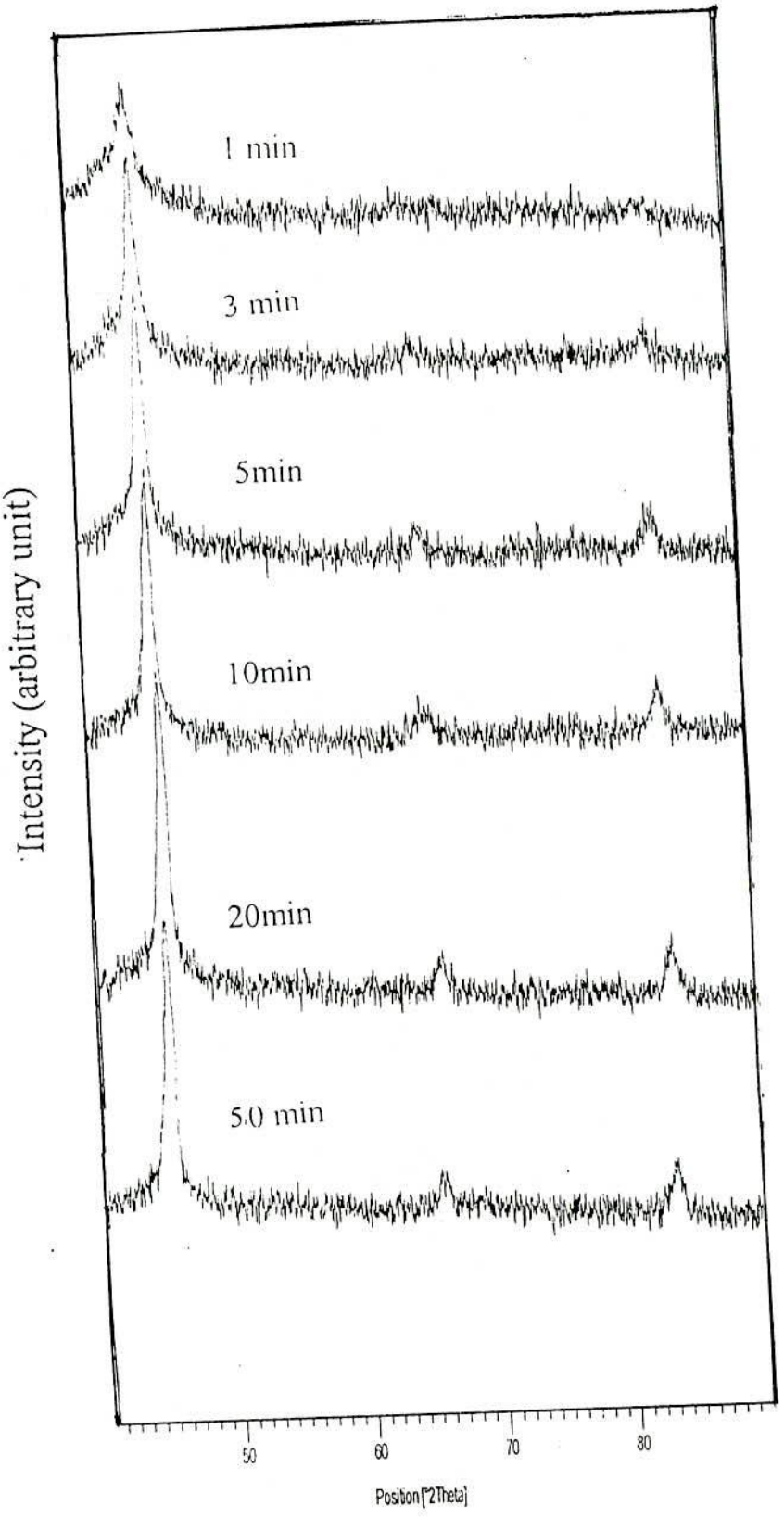

Fig. 5.4 X-ray diffraction spectra of $Fe_{73.5}Cu_1Nb_3Si_{13.5}B_9$ alloys with different annealing time annealed at 555°C

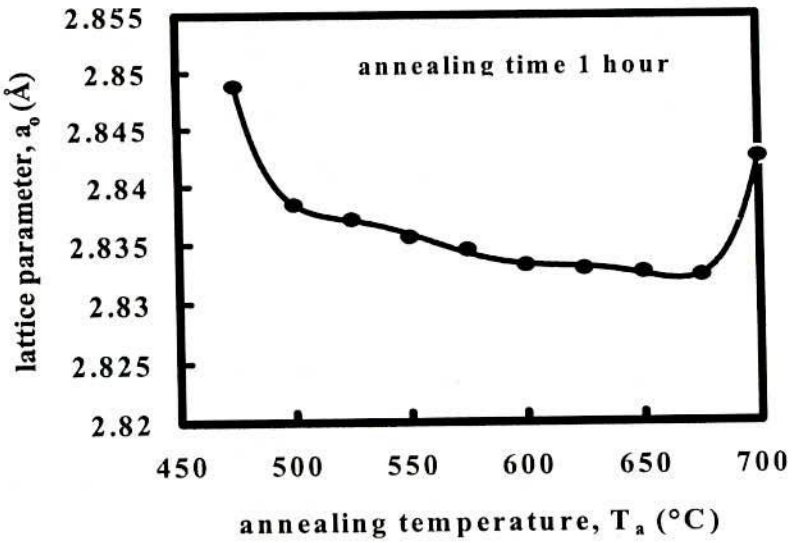

Fig. 5.5 lattice parameter, a_0 in the α-Fe(Si) phase for the $Fe_{73.5}$ Cu_1 $Nb_3Si_{13.5}B_9$ alloy versus the annealing temperature T_a.

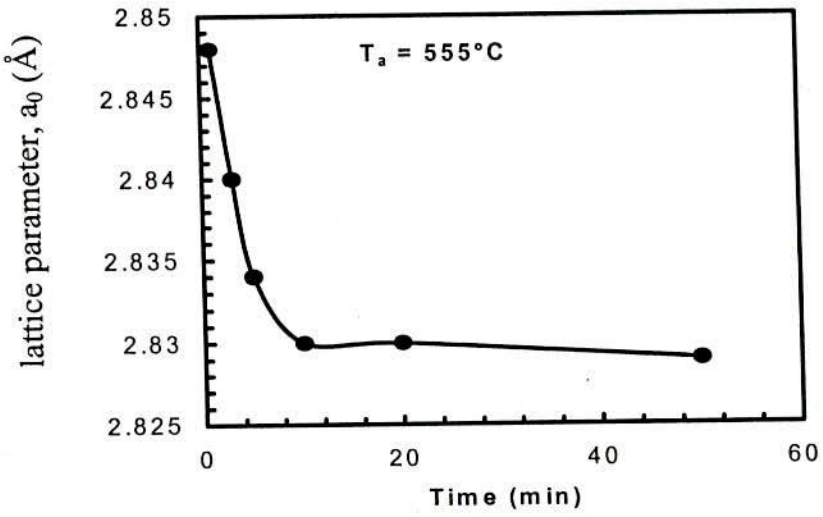

Fig. 5.5 lattice parameter, a_0 in the α-Fe(Si) phase for the $Fe_{73.5}$ Cu_1 $Nb_3Si_{13.5}B_9$ alloy versus annealing time annealed at 555^0C

Experimental XRD data of nanocrystalline $Fe_{73.5}Cu_1Nb_3Si_{13.5}B_9$ amorphous ribbon at different annealing temperatures.

Table – 5.1

Temp(T°C)	θ	d	FWHM	a_o(Å)	D_g(nm)	Si(at%)
AC						
450						
475	22.500	2.0149	2.52	2.8490	3	12.31
500	22.586	2.007	1.04	2.8380	8	17.454
525	22.597	2.0061	0.87	2.8361	10	17.87
550	22.610	2.0051	0.85	2.8356	10	18.5
575	22.620	2.0043	0.82	2.8345	11	19.08
600	22.630	2.0034	0.79	2.8332	11	19.70
625	22.633	2.0032	0.78	2.8329	11	19.84
650	22.636	2.0029	0.78	2.8326	11	19.98
675	22.638	2.0028	0.60	2.8323	14	20.1
700	22.645	2.0022	0.39	2.8425	22	14.07

Experimental XRD data of nanocrystalline $Fe_{73.5}Cu_1Nb_3Si_{13.5}B_9$ amorphous ribbon at different annealing time at 555°C.

Table – 5.2

Time	θ	**d**	**FWHM**	**a_o(Å)**	**D_g(nm)**	**Si(at%)**
1	22.50	2.0140	1.66	2.848	5	12.78
3	22.57	2.0080	0.83	2.840	11	16.52
5	22.62	2.0040	0.75	2.834	12	19.32
10	22.65	2.0017	0.67	2.830	14	21.19
20	22.65	2.0017	0.66	2.830	14	21.19
50	22.66	2.0000	0.60	2.829	14	21.65

again the value of lattice parameter increases at annealing temperature700°C.

In fig. 5.5 it is clear that with the increase of annealing temperature the lattice parameter first decrease gradually then slowly again increase sharply. Since these lattice parameters of bcc Fe phase are significantly smaller than those of $a_o = 2.8488\,\overset{0}{A}$, it can be speculated that the metalloid element B is practically insoluble in α-Fe (<< 0.01 at %), the bcc phase in the $Fe_{73.5}Nb_3Cu_1Si_{13.5}B_9$ alloy consists essentially of Fe-Si. In fig-5.6 it is clear that with the increase of annealing time the lattice parameter decreases first gradually and then very slowly at constant annealed temperature of 555°C. The values of lattice parameter, determined experimentally, were found to be in the range of $(2.848 - 2.829)\,\overset{0}{A}$ for the sample. Lattice parameter decreases gradually with the increase of annealing time due to the contraction of bcc Fe lattice as a result of diffusion of the Si with smaller atomic size into Fe lattice with higher atomic size.

The results of lattice parameter and intrinsic magnetic property measurement have evidence that the Si content in the α-Fe(Si) phase of the $Fe_{73.5}Nb_3Cu_1Si_{13.5}B_9$ alloy has a saturate value that is far higher annealing time than that of the composition of the alloy in the amorphous state. It means that, the silicon tends to dissolve in the bcc nanocrystalline phase and the Si content in the residual amorphous phase is rather low in the alloy. It is clear that the magnetic properties obviously varied within the range of the annealing temperature; the excellent properties are exhibit at 555°C. The optimum values of initial permeability (μ') and coercivity (H_c) are nearly the same as those reported by Yoshizwa [5.4].

5.2.2 Grain Size Determination

The main aim of the present study was to determine the nanocrystalline grain size. Grain size for all the annealing temperature and the annealing time of the composition was determined using Scherrer method. Fig-5.3 and Fig-5.4 shows the XRD patterns of (110) reflection for different steps of annealing temperature and annealing time of composition $Fe_{73.5}Nb_3Cu_1Si_{13.5}B_9$, from which grain size was determined using the formula,

$D_g = \frac{0.9\lambda}{\beta\cos\theta}$, where $\lambda = 1.54178\,\text{Å}$ for Cu-k_α radiation and β = FWHM (full width at half maximum) of the peak in radian. Considering Δ in degree we get the relation, $D_g = \frac{79.5}{\beta\cos\theta}$.

All The values of grain size for every steps of annealing temperature and annealing time of the composition were determined and the values are listed in Table-5.1 and Table-5.2. In Fig-5.3, it is clear that at low temperature, 475°C, the FWHM of the peak is large and with the increase of annealing temperature the value of FWHM getting smaller. The peak is, therefore, getting shaper with the shifting of peak position towards higher 2θ value. This fact indicates that at 475°C the grain size is smaller in size, 3nm, and with increase of annealing temperature grain size is getting bigger in size within the range of (8-14) nm. Above 675°C grains grow rapidly and attains a maximum value of 22 nm at 700°C. Our result corresponds well with the results of Rubinstein *et. al.*[5.5]. Fig-5.7 shows the determined crystalline grain size versus annealing temperature (T_a) of the nanocrystalline composition. The peak shifts indicates the change of the value of lattice parameter of nanograins, which were determined earlier and thus change of the value of Si content in the nanograins. At annealing temperatures 525°C to 650°C, the increase in the grain size of bcc Fe (Si) of the composition is rather small and has been attributed combined addition of Cu and Nb elements.

The nanocrystalline structure is relatively insensitive to the annealing temperature for these materials. However, the onset of crystallization and the crystallized volume fraction depends on T_a and the Nb content. Annealing at higher temperature above 650°C leads to the precipitation of Fe-borides [1.2]. The formation and the structure of nanocrystalline grains besides the chemical compositions are also strictly related to the details of the heat treatment. The crystallization occurs at higher temperature in shorter time than conventional annealing. The nanocrystalline material obtained in this way displays improved mechanical and magnetic properties in comparison to the ones achieved by conventional annealing [5.6-5.7]. In Fig. 5.8 it is clear that with the increase of annealing time the grain size of the sample increase first gradually then slowly again very sharply for the same nanocrystalline $Fe_{73.5}Nb_3Cu_1Si_{13.5}B_9$ alloy annealed at 555°C. The average grain size increases rapidly within 10 minutes attaining a limiting value of (13-14) nm. This shows that kinetics of nanocrystallization is quite fast at 555°C.

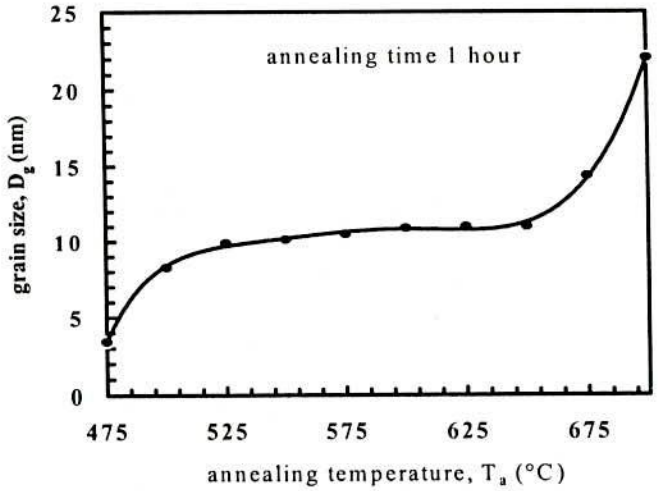

Fig. 5.7 Grain size D_g of the α-Fe(Si) phase in the $Fe_{73.5}$ Cu_1 $Nb_3Si_{13.5}B_9$ alloy versus annealing temperature T_a.

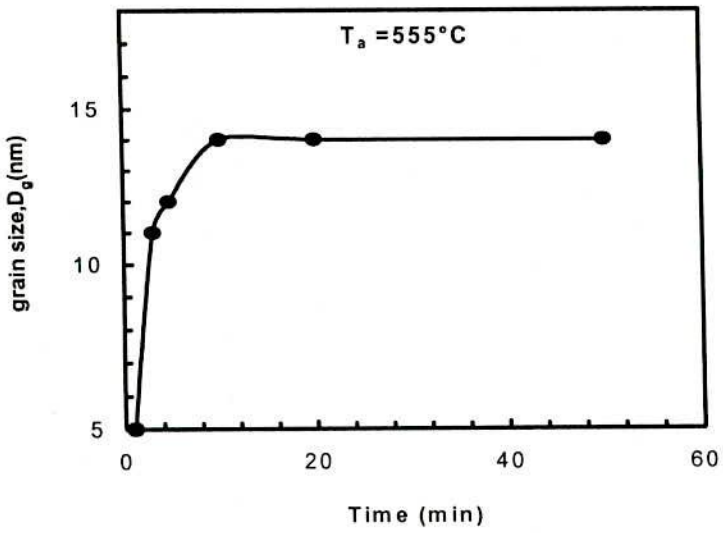

Fig. 5.8 Grain size D_g of the α-Fe(Si) phase in the $Fe_{73.5}$ Cu_1 $Nb_3Si_{13.5}B_9$ alloy versus annealing time at $T_a = 555^0$C.

5.2.3 Si Content in Nanograins

The major elements of the amorphous ribbon were Fe and Si with the concentration of 73.5 at % Fe and 13.5 at % Si. Crystalline nanograins were formed on the ribbon in the process of annealing temperature with the alloy composition of Fe-Si. It is therefore important to determine the concentration of Fe and Si in the nanograins. As because the alloy nanograins are consists of Fe and Si and we have experimentally determined the lattice parameter of the alloy nanograins for the compositions at different annealing temperatures. It is easy to calculate the Si content in the nanograins from Pearsons handbook relationship [4.2]. From the relationship we have considered a simple equation to calculate Si content from lattice parameter. The equation is $b = - 467\ a_o + 1342.8$, where b is at % Si in the nanograins, a_o is the lattice parameter of nanograins. Calculated Si content for the two compositions at different annealing temperatures were listed in Table-5.1. We have known that the lattice constant decreases by increasing the Si content in a Fe-Si alloy, and there is a corresponding relationship between the Si content and the lattice constant in Fe-Si alloys. So, according to the lattice parameter results, the Si content in the α-Fe(Si) phase for the alloys annealed at different temperatures can be determined and is shown in Fig-5.9.

It is easy to see that the Si content in the α-Fe(Si) phase increases with the annealing temperature from 475°C to 575°C, and in the range of 600°C to 675°C, it is about 20 at.% and hardly varied with the annealing temperature when Si content decreases further annealing temperature of 700°C. Annealed at higher annealing temperatures, first leads to the precipitation of borides and subsequently to grain coarsening which both deteriorates the soft magnetic properties [5.8]. The formation of Fe-B compounds such as Fe_3B leads to the disappearance of soft magnetic properties. It is very important for the achievement of good soft magnetic properties to make the grain size ultrafine to suppress the formation of Fe-B compounds and to decrease the variation of magnetic induction between grain boundary phase and grain phase. Clearly it also shows that the Si content in α-Fe(Si) phase is

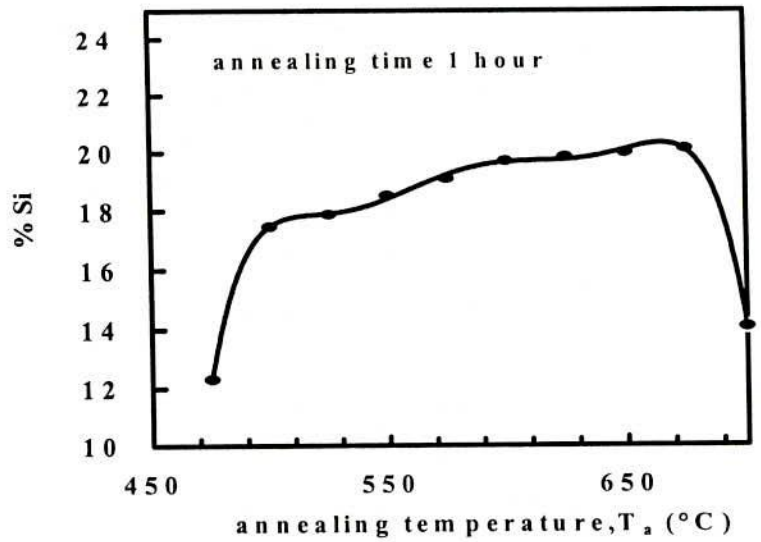

Fig. 5.9 Si content of the α-Fe(Si) phase in $Fe_{73.5}$ Cu_1 $Nb_3Si_{13.5}B_9$ alloy versus annealing temperature T_a .

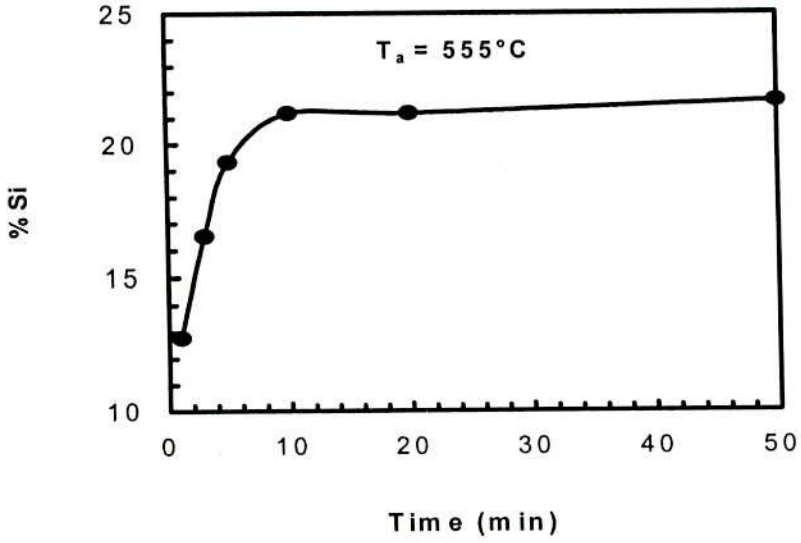

Fig. 5.10 Si content of the α-Fe(Si) phase in $Fe_{73.5}$ Cu_1 $Nb_3Si_{13.5}B_9$ alloy versus annealing time annealed at 555^0C.

about the same for the alloys annealed from 600°C to 675°C, which coincides with the results obtained from the lattice parameter determination. In the Fig-5.10 is clear that with the increase of annealing time Si content increases first gradually and then slowly. Sharp increase of Si content in α-Fe(Si) phase is observed attaining a maximum value of 21 at.% Si within10 minutes of annealing at 555°C which corresponds well with the Mössbauer study.[5.8] Lattice parameter decreases with annealing time due to the contraction of bcc Fe lattice as a result of diffusion of the Si with smaller atomic size into Fe lattice.

5.3 Dynamic Magnetic Properties of Nanocrystalline Amorphous Magnetic Materials

Dynamic magnetic properties of the nanocrystalline magnetic ribbon with composition $Fe_{73.5}Nb_3Cu_1Si_{13.5}B_9$ have been measured as a function of frequency in the range from 1kHz to 500kHz. The measurement has been done both in the as-quenched, pre-annealed and annealed condition. Permeability measurements were performed on toroidal samples at frequency of 1kHz –500kHz and an applied ac driving field (≈ 0.5 A/m) low enough to ensure the measurement of initial permeability (μ') by an impedance analyzer Wayne Kerr 3255B model. In order to avoid the experimental error due to fluctuation in ribbon thickness and thermal treatments, just on piece of each ribbon has been measured at room temperature after subsequent annealing treatments.

5.3.1 Frequency dependence of initial permeability of $Fe_{73.5}Nb_3Cu_1Si_{13.5}B_9$ Alloy with Different Annealing Temperature

The measurement has been done on as-cast specimen and also on samples annealed at 350°C to 625°C for 1hour constant annealing time. Fig-5.11 shows the frequency dependence of the real part of the complex initial permeability for as-cast and samples pre-annealed in the temperature range 350°C to 487°C at constant annealing time T_a = 1hour. It is observed that the initial permeability increases with the increase of annealing temperature attaining the maximum value at the annealing temperature of 475°C. When the pre-annealing temperature is higher than 475°C initial permeability decreases rapidly. The decrease of permeability may be attributed to the stress developed in the

amorphous matrix by the growing crystallines. This act as pinining centers for the domain wall mobility. The growing crystallites are for apart from each other representing small volume fraction that cannot be exchange coupled and the anisotropy cannot be averaged resulting in weak intergrain magnetic coupling. At this temperature the initiation of crystallization takes place. This decrease in the μ' is also observed in the sample pre-annealed for 1 hour at 487°C before nanocrystallization. Fig. 5.12 shows the frequency dependence annealing 500°C to 625°C for T_a = 1 hour. It is observed that the low frequency value of initial permeability increase with the increasing temperature attaining the maximum value at the annealing temperature 560°C, when the annealing temperature is higher than 560°C, initial permeability decreases rapidly. This spectrum evidences the real change that the nanocrystallization produces in each annealed sample, including the kinetics of the structural changes. The μ' is observed to increase during nanocrystallization of the samples, as expected, but the enhancement rate is clearly different for each annealed ribbon.

It is however important to remark that a general trend is observed and samples produced with higher μ' display a greater enhancement in the magnetic permeability compared to the as-cast sample μ' as a function of annealing temperature measured at a fixed frequency of 1 kHz is shown in Fig. 5.13. A remarkable dependence of μ_i on annealing temperature is observed. The increase of μ' up to the annealing temperature 475°C is comparatively small and may be attributed to irreversible structural relaxation of the amorphous state. While the annealing temperature exceeds 500°C a sharp increase of μ' takes place which is associated with the nanocrystallization of α-Fe(Si) phase. Fig- 5.13 shows as a consequence steep increase of μ' is observed. An enhancement of μ' by two orders of magnitude compared with its amorphous precursor is observed for the sample annealed at 560°C is evidenced which is associated with the evolution of iron-boride phase.

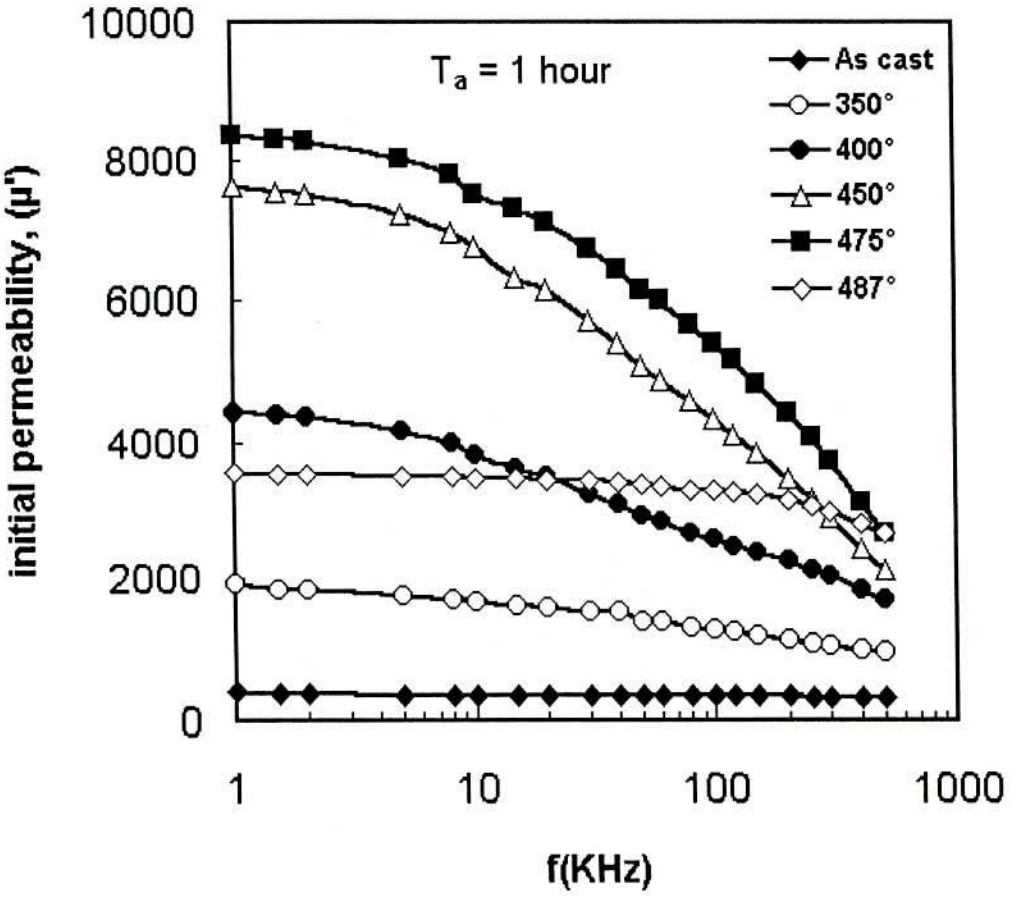

Fig. 5.11 Frequency dependence of real component of initial permeability of as-cast and annealed samples for 1hour of $Fe_{73.5}Cu_1Nb_3Si_{13.5}B_9$ alloy.

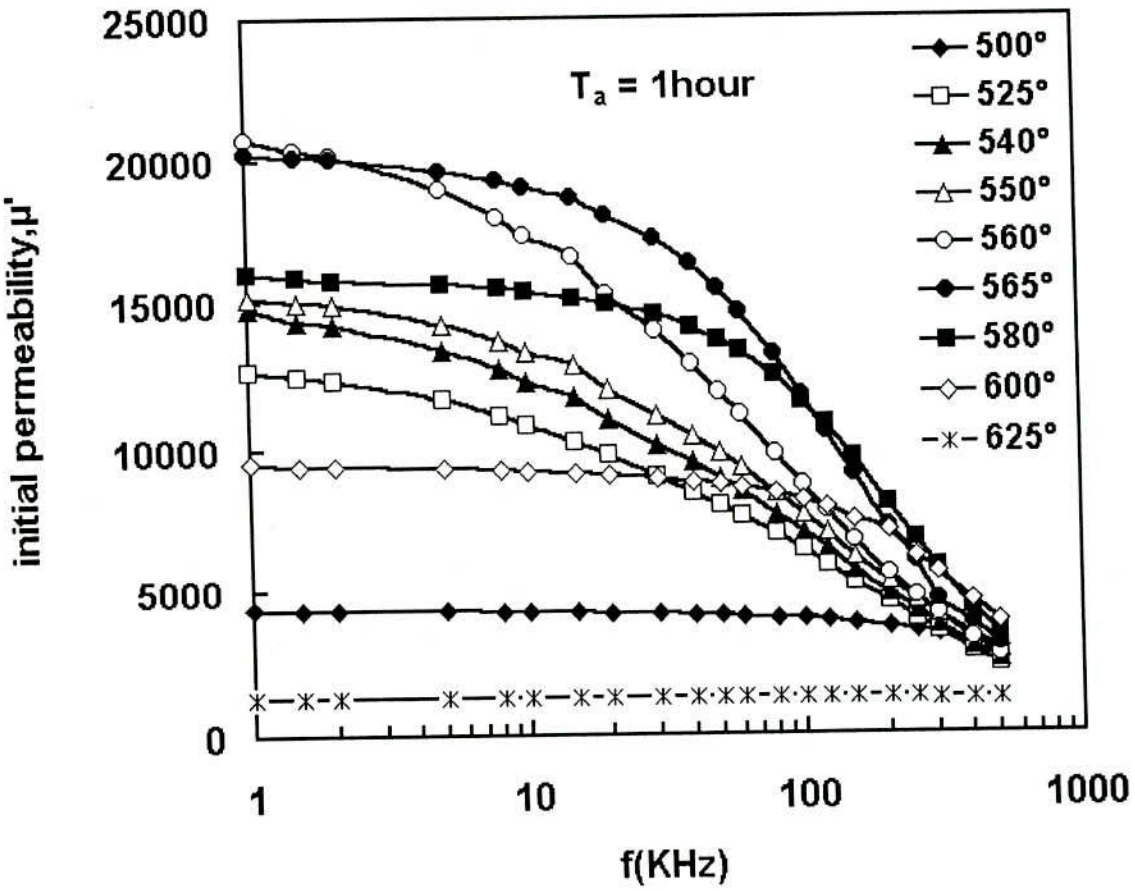

Fig. 5.12 Frequency dependence of real component of initial permeability at different annealing temperature for 1 hour of $Fe_{73.5}Cu_1Nb_3Si_{13.5}B_9$ alloy.

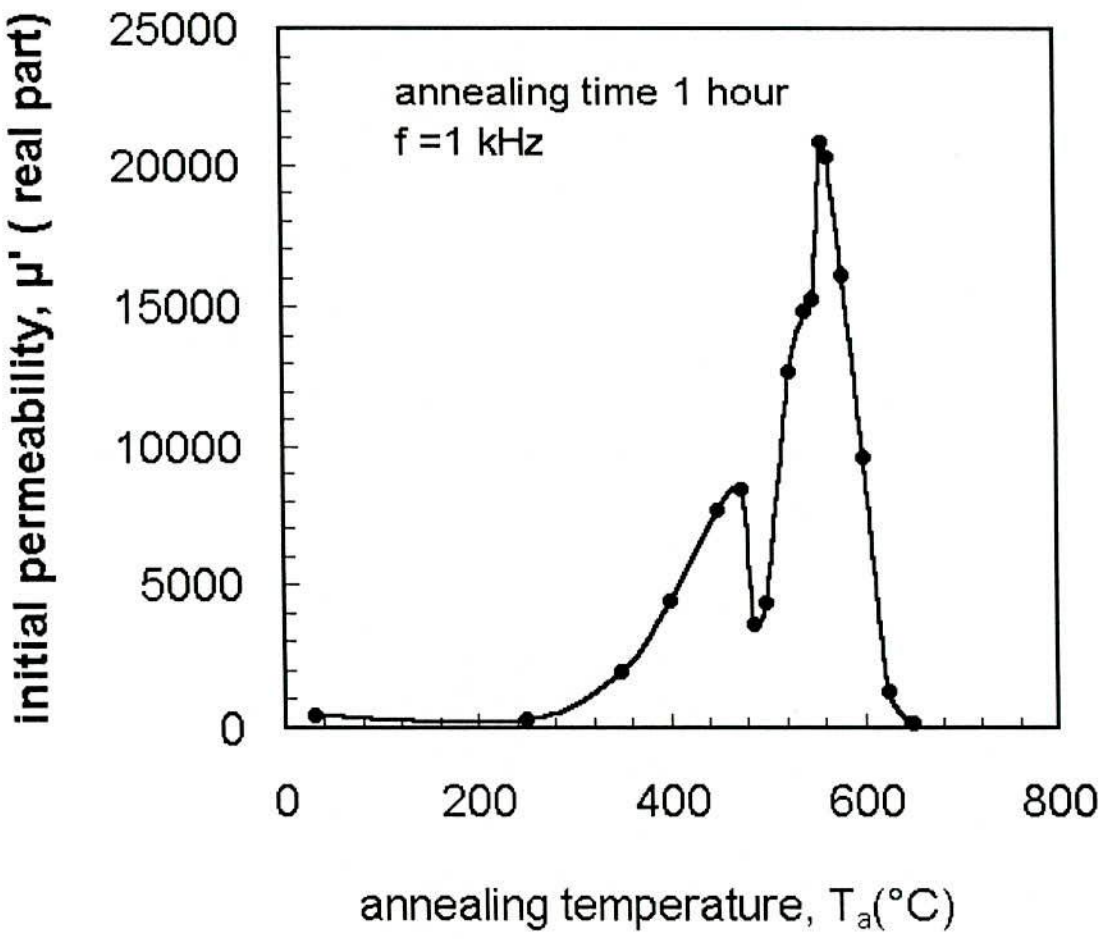

Fig. 5.13 Variation of real component of initial permeability of $Fe_{73.5}Cu_1Nb_3Si_{13.5}B_9$ alloy with annealing temperature, T_a at 1kHz.

5.3.2 Frequency Dependence of Initial Permeability of $Fe_{73.5}Nb_3Cu_1Si_{13.5}B_9$ Alloy with Step Annealing Time

The changes of initial permeability (μ') at room temperature as a function of frequency determined for samples annealed at temperature T_a = 400°C and then subsequently annealed at 555°C for different time interval and without preanneal are shown in fig-5.14 and fig-5.15. As a consequence amorphous state of the ribbon moves into a new thermodynamic equilibrium via local microvoid rearrangements. At high temperature 555°C at one hour annealing are irreversible migration causes at least a partial annealing out of microvoids which is confirmed by a decrease of magnetic after-effect intensity. In the second stage at the temperature 555°C at 1 hour annealing, the μ_i increases strongly up to maximum value. This effect can be related to three different processes

1) a formation of the α-Fe(Si) nanocrystalline structure,
2) a decrease of the effective magnetostriction constant and
3) an annealing out of microvoids.

As already shown by X-ray diffraction analysis and the formation of α-Fe(Si) nanocrystalline structure with the grain size of about 10-14nm was observed. Fig. 5.15 shows frequency spectrum with increasing annealing time at constant annealing temperature 555°C. Further increase of annealing temperature leads to the increase of α-Fe(Si) nanograins coupling via exchange interaction resulting in a reduction of anisotropy energy. An enhancement of initial permeability by two orders of magnitude was observed for the samples annealed at 560°C. For samples annealed above 560°C, μ' drops to lower value drastically. The probable reason might be the evolution of boride phase and nonmagnetic fcc Cu. This leads to the increase of magnetocrystalline anisotropy to a high value, which essentially reduces the local exchange correlation length weaking the inner-granular magnetic coupling as a results of which magnetic hardening takes place. Fig. 5.16 shows that initial permeability of the sample as a function of cumulative annealing time μ' rapidly increase at the highest value of μ' around 23500 as compared to the as-cast sample up to five minute annealing time decreases with increasing annealing time at constant frequency 1 kHz and at constant temperature T_a = 555°C.

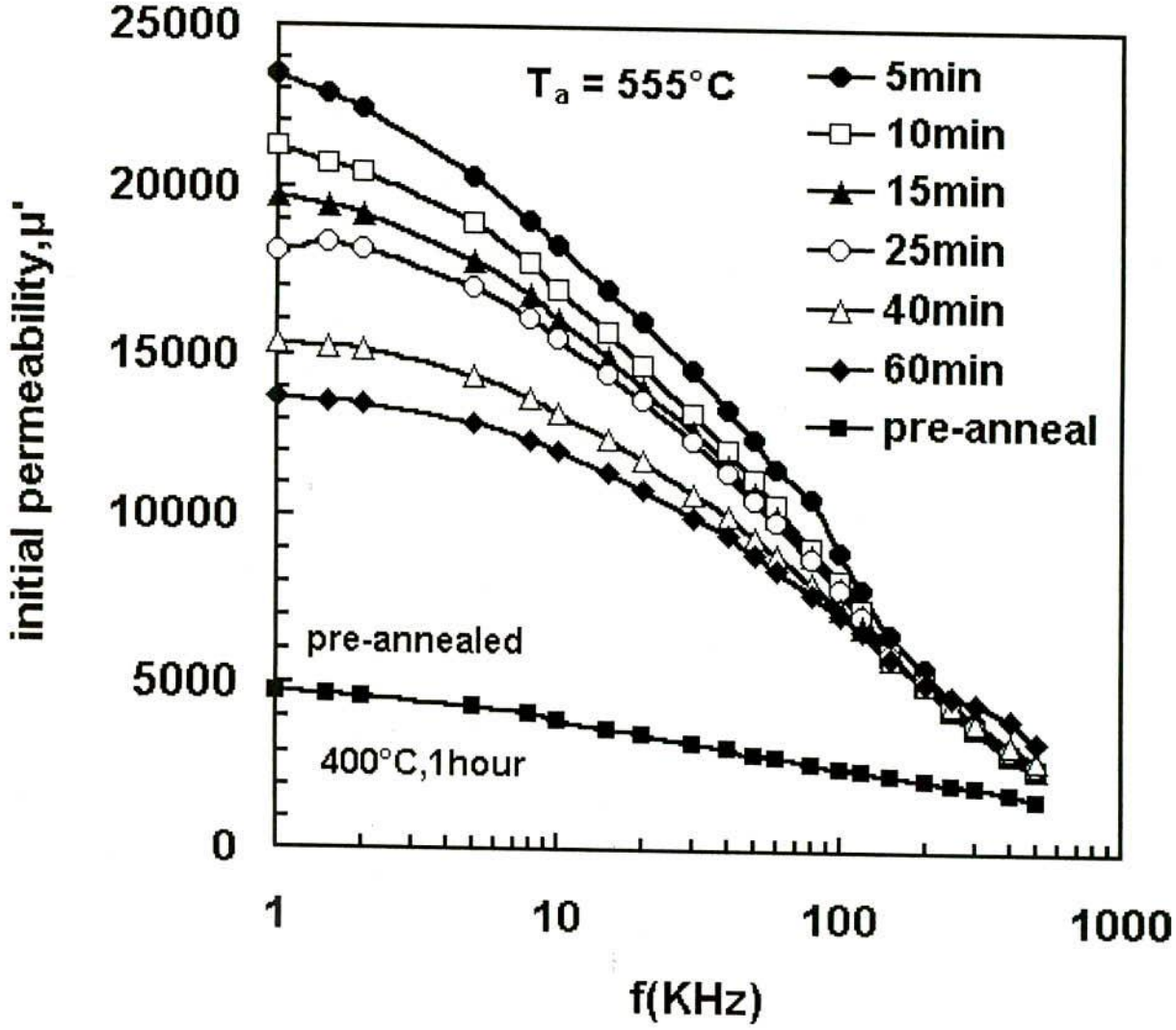

Fug. 5.14 Frequency dependency of initial permeability of $Fe_{73.5}Cu_1Nb_3Si_{13.5}B_9$ alloy with preannealed at 400°C and annealed at 555°C.

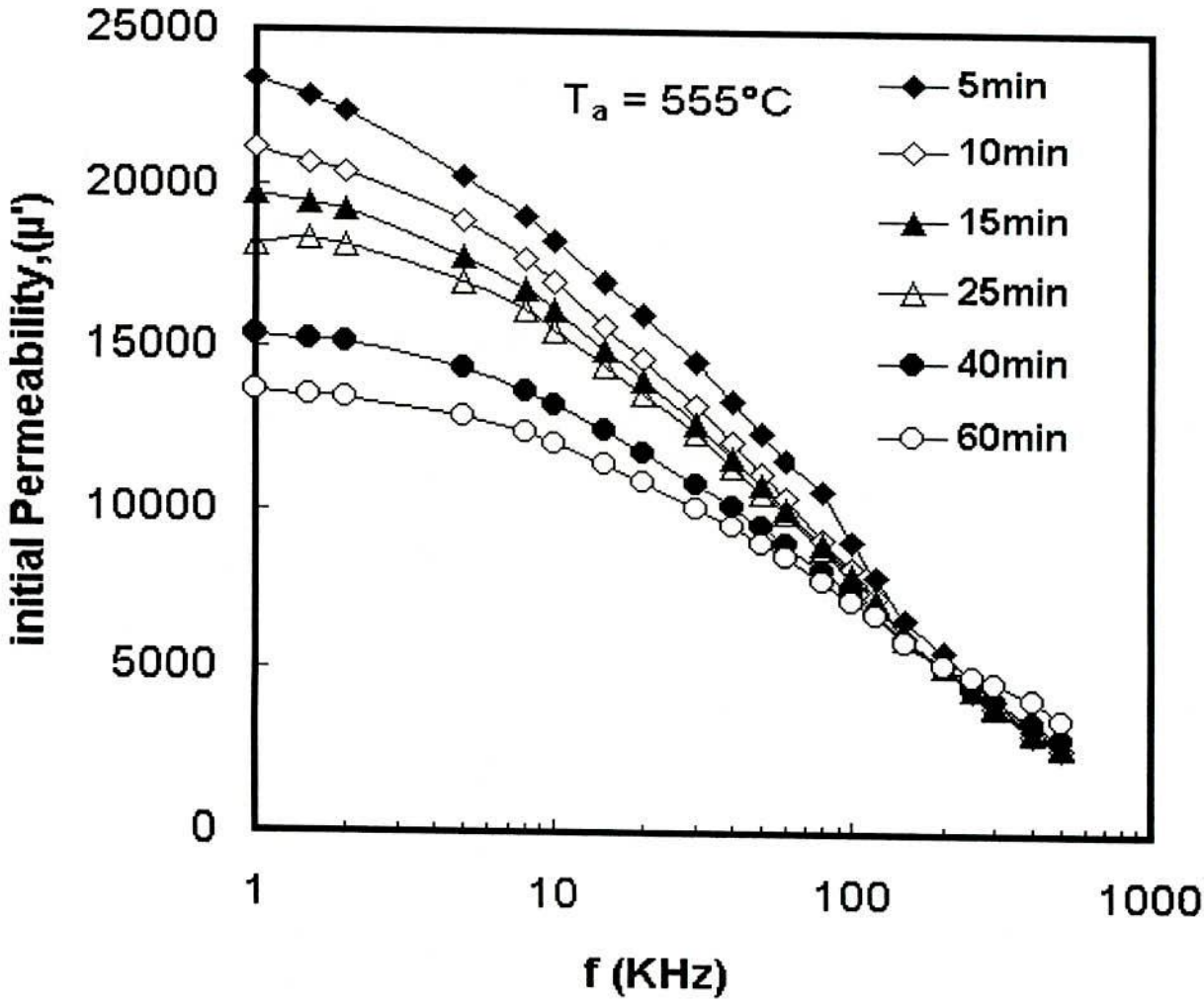

Fig. 5.15 Frequency dependence of initial permeability of $Fe_{73.5}Cu_1Nb_3Si_{13.5}B_9$ alloy with different annealing time annealed at 555°C.

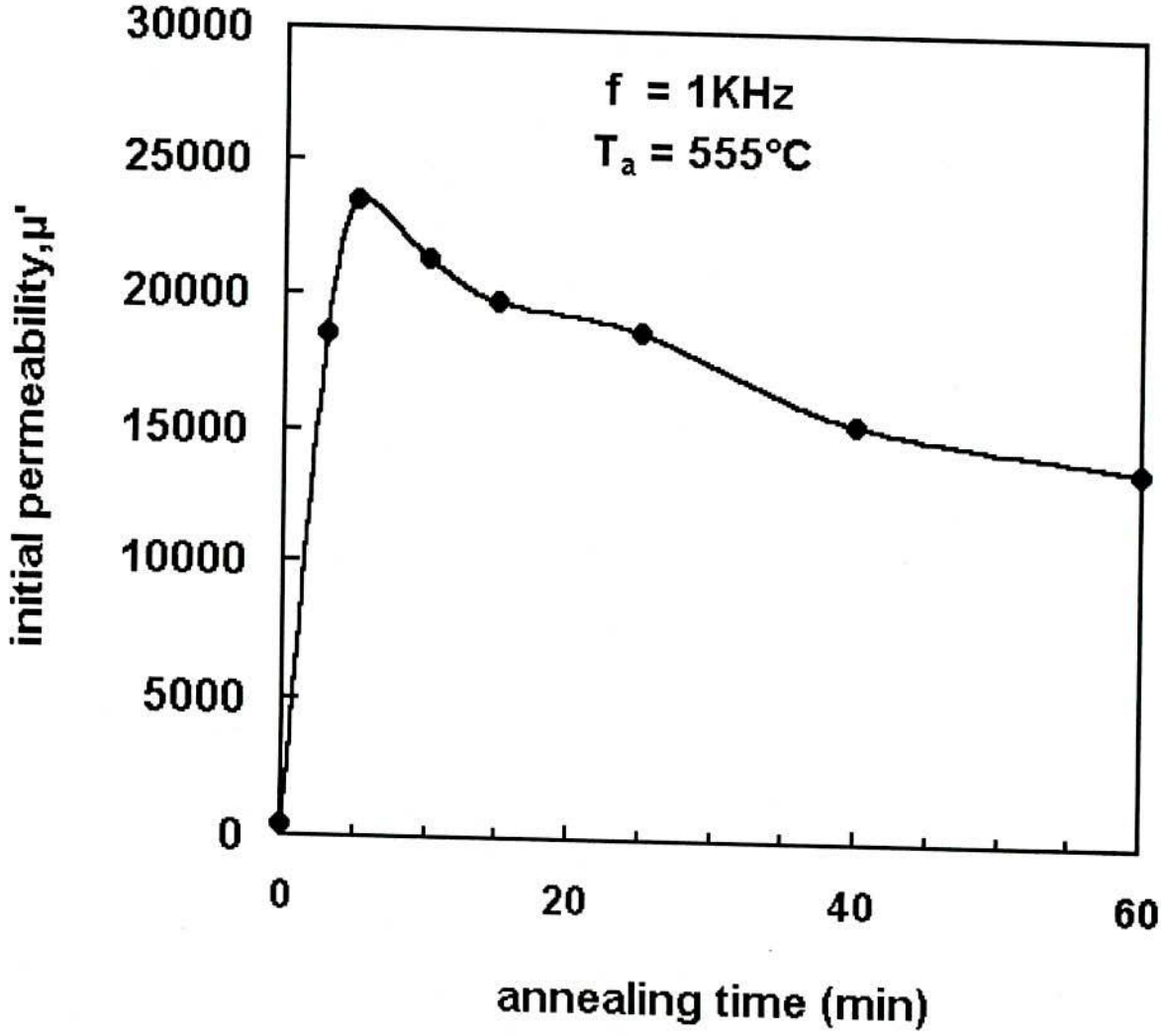

Fig. 5.16 Variation of initial permeability of $Fe_{73.5}Cu_1Nb_3Si_{13.5}B_9$ alloy with annealing time at 1kHz.

It can be observed that the permeability enhancement with short time annealing is more effective then long time annealing at the same temperature. Upon further increase of annealing time up to 60 minutes, the value of μ' does not vary significantly and maintains a plateau value of 23500-14000. It has been demonstrated that when a sample is annealed for cumulative time, the effect of induced anisotropies become dominant and the permeability is significantly reduced [5.9, 5.11]. This behavior leads to very small values for the sample annealed for a time 5 minute to a remarkable improvement of the soft magnetic properties achieved through the reduction of the magnetoelastic property. It is the actual highlight of nanocrystalline Fe-base alloys that the phases formed on crystallization can lead to low or vanishing saturation magnetostriction (λ_s) while λ_s is fairly independent of the composition in the amorphous state, it depends sensitively on the Si content in the nanocrystalline state, passing through 12 at. % at low annealing time and at high Si concentrations wound 22 at.% at high annealing time. The decrease of μ' at higher Si contents is creep induced anisotropies. μ' exhibited its maximum value within 5 minutes of annealing time and then slightly decreases toward a plateau value for longer annealing time. This may be attributed to the effect of induced anisotropy develops during the cumulative time annealing which plays a dominant role in decreasing the permeability [5.9]. The occurrence of steep rise in permeability in concomitance with the formation of the nanocrystalline grain is ascribed to the drastic reduction in magnetocrystalline anisotropy averaged out by the exchange interaction via strong intergrain coupling. It is concluded that the optimum magnetic softening takes place within a short time when annealed well above the crystallization temperature.

Fig. 5.17 shows frequency spectrum for the sample subjected to two-step annealing (The first step at 425°C and the second step at 545°C) for 30 minute. It is seen that the nanocrystalline sample obtained by the annealed of the amorphous sample, which was per-annealed at 425°C for 30 minute, exhibits an μ' equal to about 10,000 at 1kHz (at room temperature). However, the μ' of the nanocrystalline sample, obtained another step annealed at 545°C for 30 minute, reaches a low μ'equal to about 6000 at 1kHz. At the same time, from the distribution of grain sizes in the nanocrystalline samples depends on the annealing temperature.

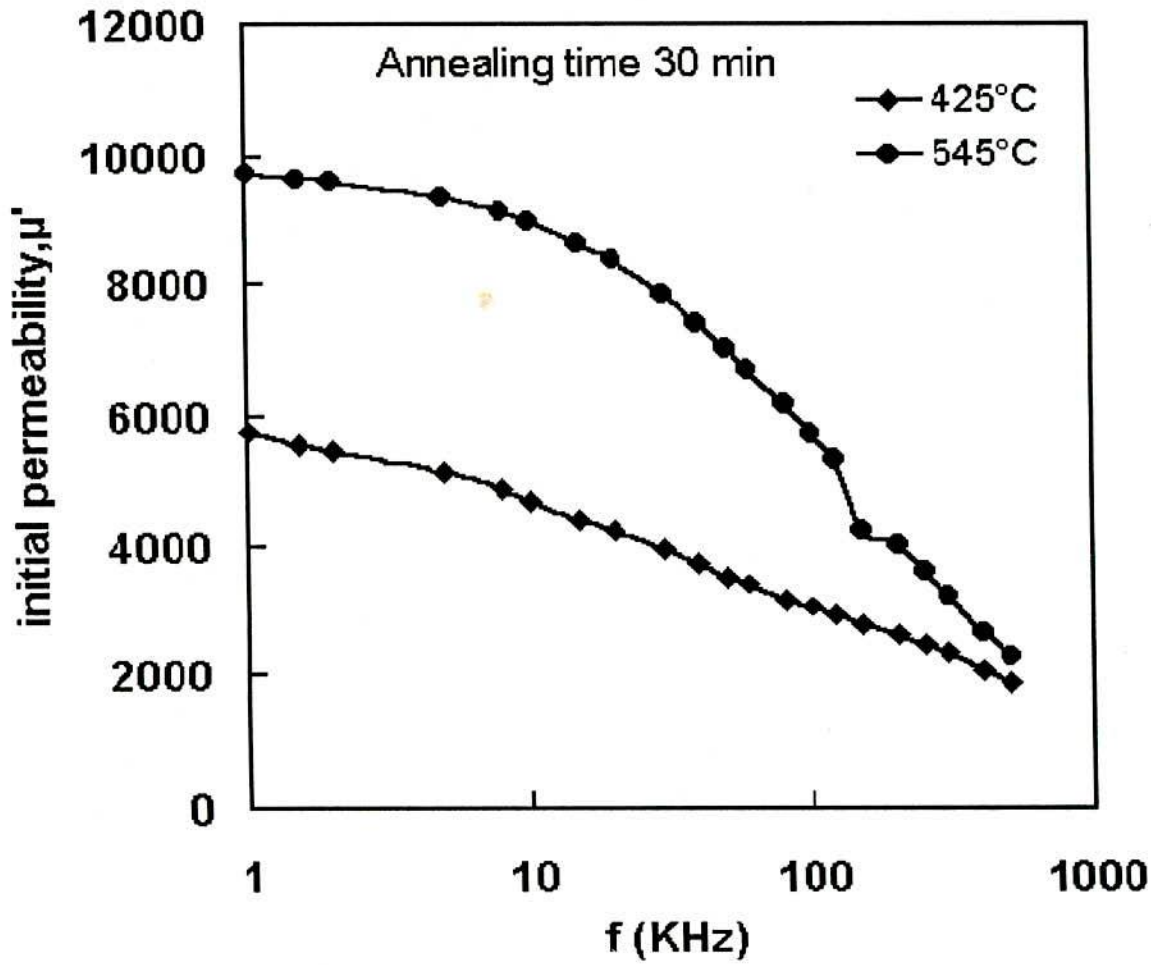

Fig. 5.17 Frequency dependence of initial permeability of $Fe_{73.5}Cu_1Nb_3Si_{13.5}B_9$ alloy obtain by two step annealed at 30 minute.

5.3.3 Frequency Dependence of Imaginary part of the Complex Permeability of Composition $Fe_{73.5}Nb_3Cu_1Si_{13.5}B_9$ Alloy

The sample with composition $Fe_{73.5}Nb_3Cu_1Si_{13.5}B_9$ annealed at 525°C, 565°C and 580°C for 1hour has been studied for its frequency dependence. The effect of annealing on the complex permeability (μ'') and its frequency dependence for the sample is shown in fig. 5.18. These results are quite complimentary to the results for the real part of the complex permeability of the sample. The usefulness of the results of complex permeability lie in the determination of the quality factor of the sample. The μ'' increases for the annealed samples indicating that higher annealing temperature causes further growth of crystallites and their stability.

5.3.4 Loss Factor

Loss factor, tanδ and relative quality factors are the important parameters for the soft magnetic materials from the application point of view. Minimum loss factor and maximum relative quality factors are the preconditions for soft magnetic materials. It is wellknown that upon optimal annealing nanocrystalline alloys display minimum loss and very high relative quality factor, $\mu'Q$ with the order of magnitude 10^5-10^6. Optimal annealing temperature is determined through successive annealing of the alloys from say 200°C to 600°C.

The annealing temperature dependence of loss factor of the samples measured at different frequency is shown in fig. 5.19. Loss factor rapidly increases with increasing annealing temperature up to 550°C. Further increase of annealing temperature 550-560°C loss factor, tanδ decreases very rapidly. Loss factor has high value at 15 kHz and decreases with the decrease of frequency. The origin of the loss factors can be attributed to various domain defects, which include non-uniform and non-repetitive domain wall motion, domain wall bowing, localized variation of the flux density and nucleation and annihilation of domain walls. At low frequencies the loss is controlled by hysteresis losses and at high frequency the flux penetration becomes low and loss is controlled mainly by interaction between the grains.

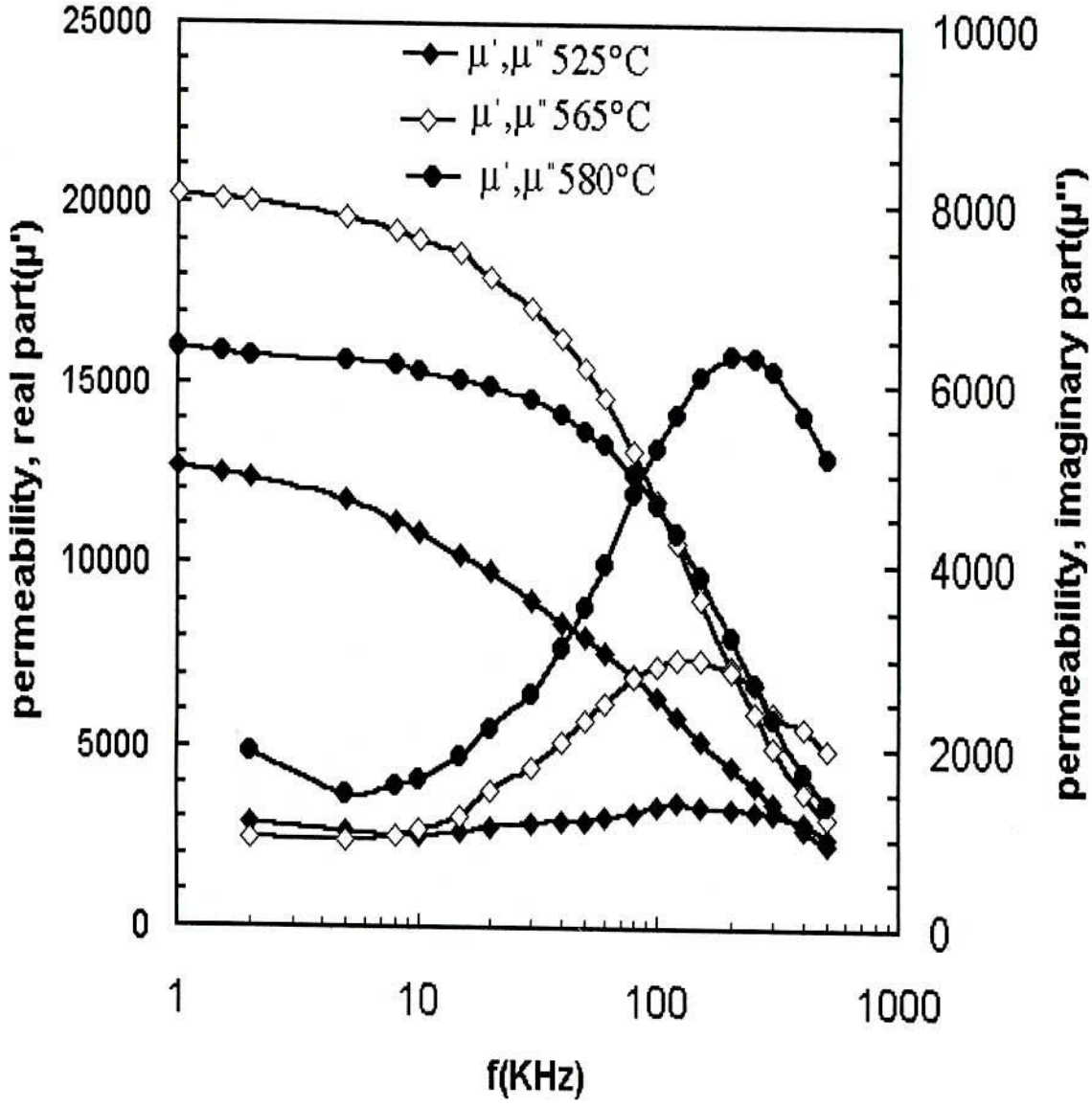

Fig. 5.18 Frequency spectrum of real and imaginary part of the complex permeability of $Fe_{73.5}Cu_1Nb_3Si_{13.5}B_9$ alloy at different annealing temperature.

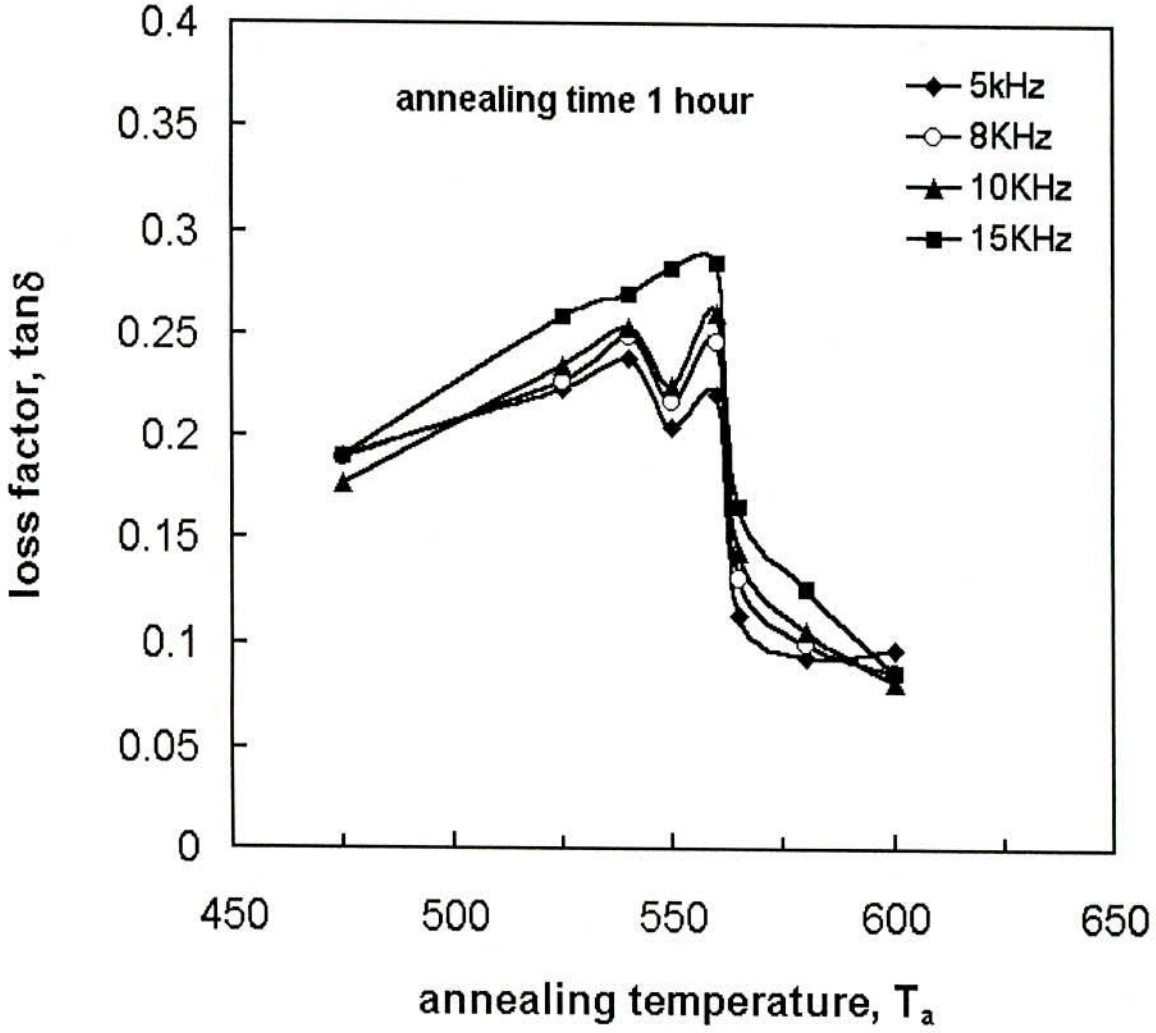

Fig. 5.19 Variation of loss factor of $Fe_{73.5}Cu_1Nb_3Si_{13.5}B_9$ alloy with annealing temperature at different frequency.

5.3.5 Relative Quality Factor

The annealing temperature dependence of relative quality factor μ'Q of the samples at different frequency are shown in fig-5.20. Relative quality factor increases with increasing annealing temperature up to 560°C. A rapid decrease of μ'Q with increasing annealing temperature above 560°C is noticed. For the sample annealed at 560°C maximum quality factor is observed for all the samples with higher μ'Q value corresponding to the lower frequency. With the increase of frequency μ'Q gradually decreases which may be attributed due to the increase of loss components. This gives a choice of optimal annealing temperature for attaining best magnetic properties.

5.3.6 Curie Temperature Measurements of $Fe_{73.5}Nb_3Cu_1Si_{13.5}B_9$ Alloy

Nanocrystalline ribbon of the sample $Fe_{73.5}Nb_3Cu_1Si_{13.5}B_9$ have been chosen for the determination of the Curie temperature (T_c), using the μ' versus T curves. Temperature dependence of ac initial permeability of the sample subjected to a heating rate of 5°c/min and the constant frequency of 10 KHz was used for exciting current from a signal generator as shown in fig. 5.21. Fig. 5.21 shows that the ac initial permeability of the nanocrystalline sample increases with increasing temperature and has the maximum value at 349°C. Beyond this point there is a rapidly decrease in the permeability. The sharp fall of the initial permeability after 354°C indicates Curie temperature. Unambiguous and sharp values of T_c, obtained from our measurements, support the fact that, in spite of chemical and structural disorder, ferromagnetic glasses have well defined magnetic ordering temperature.

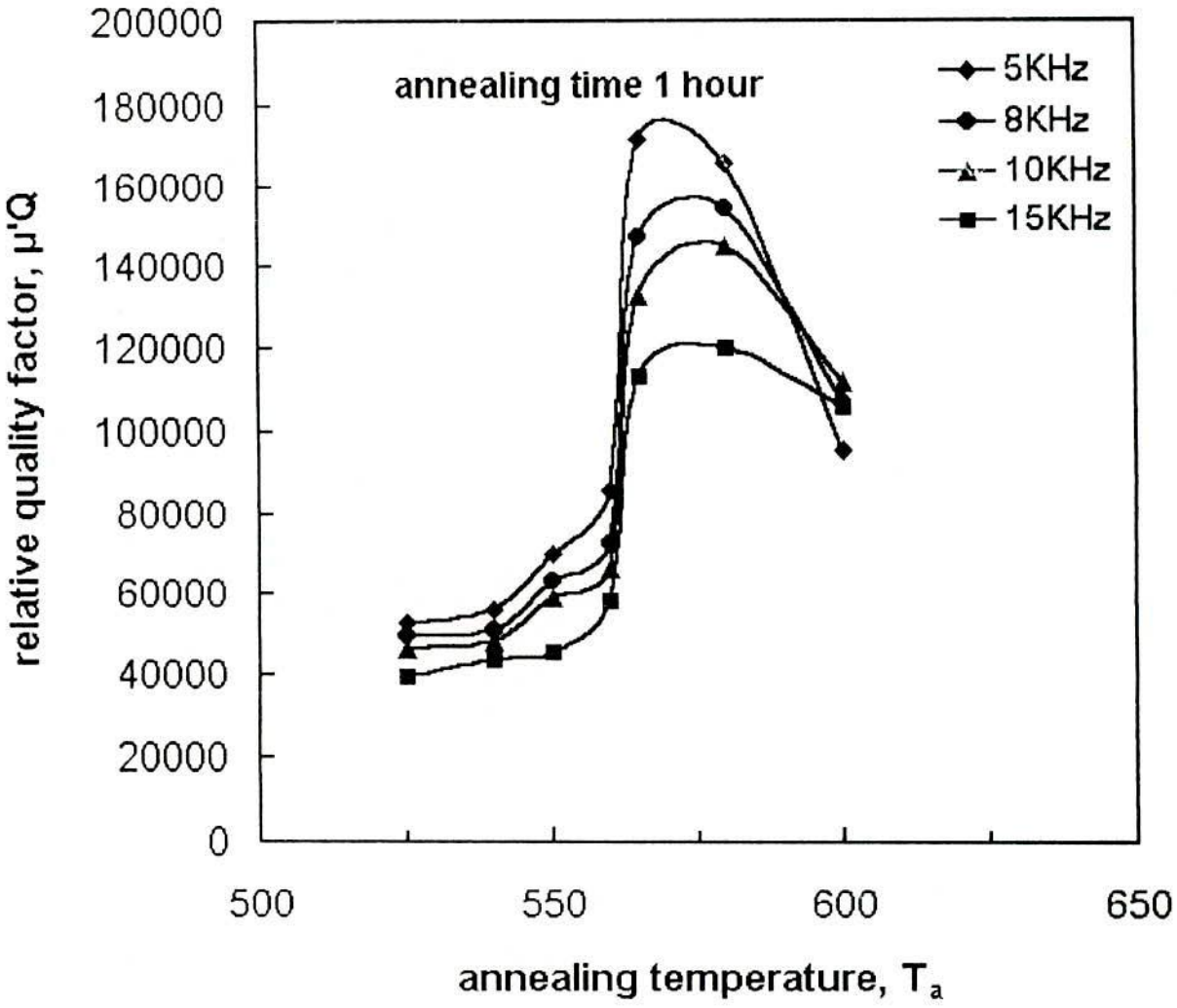

Fig. 5.20 Variation of quality factor of $Fe_{73.5}Cu_1Nb_3Si_{13.5}B_9$ alloy with annealing temperature at different frequency.

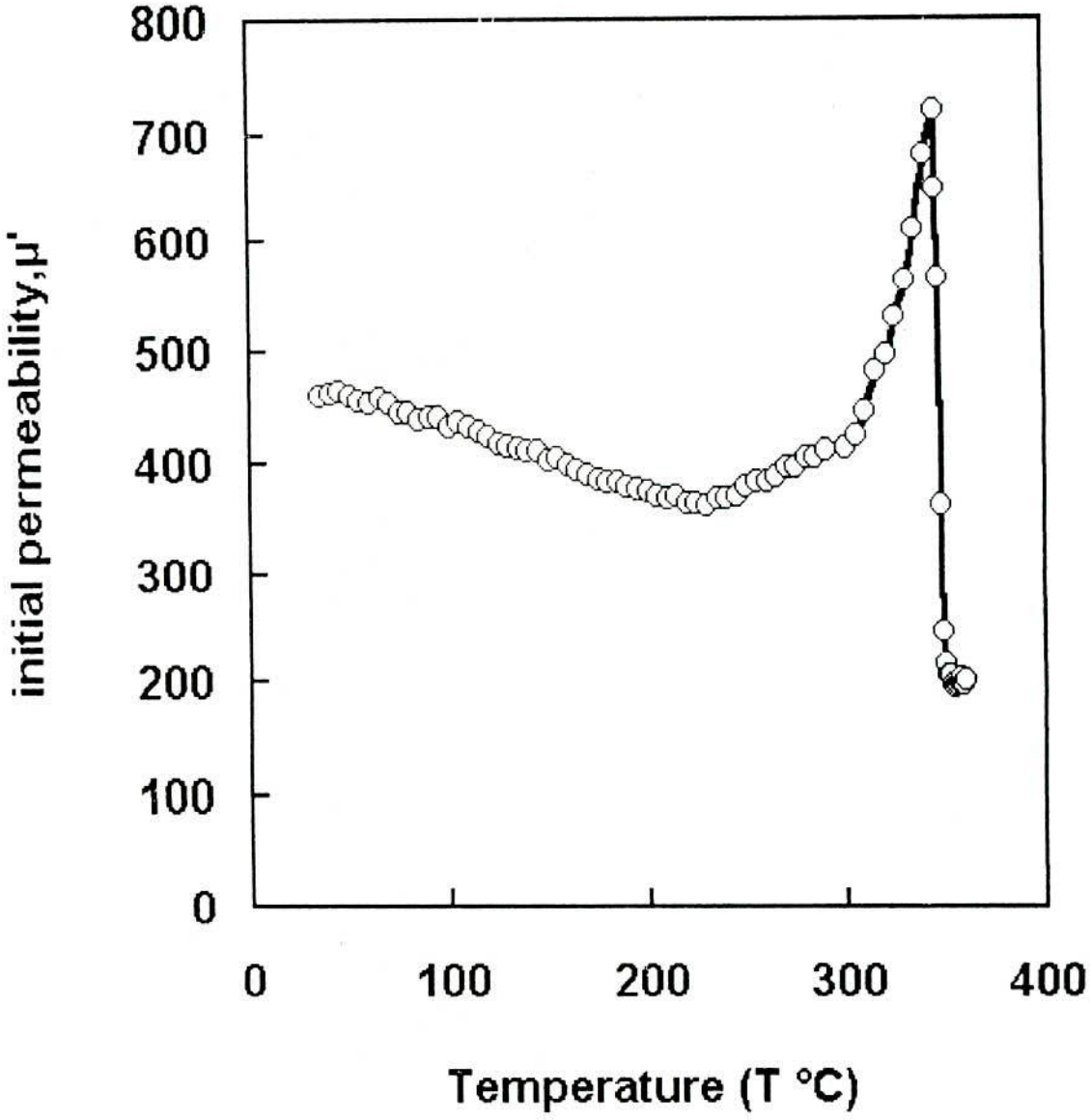

Fig. 5.21 Temperature dependence of initial permeability of as-cast amorphous nanocrystalline ribbon with composition $Fe_{73.5}Cu_1Nb_3Si_{13.5}B_9$.

5.4 Specific Magnetization Measurement of Nanocrystalline Amorphous Ribbons

The magnetization of $Fe_{73.5}Nb_3Cu_1Si_{13.5}B_9$ amorphous and samples annealed for 30minutes at varying temperatures between 400°C to550°C is measured as a function of magnetic field using a vibrating sample magnetometer (V.S.M.)[4.3]. The ribbon samples were cut into circular shapes, weighed and glued to a standard sample holder. The absolute accuracy of this system is better than 2% and the reproducibility is better than1%. Least measurable moment is $\approx 3\times10^{-3}$ Am^2. The proportionality constant accounting for the particular coil geometry and susceptibility is obtained by calibration with a high purity circular disk shaped nickel sample. The sample has a saturation magnetization of about 54.75 Am^2/kg at room temperature with an applied magnetic field of about 4 kG.

5.4.1 Effect of Annealing Temperature on Specific Magnetization at Room Temperature

Specific magnetization (M_s) has been measured on the samples is before and after annealing at different temperatures below and above the crystallization temperature. The annealing has been carried out at 400°C, 450°C, 525°C and 550°C for 30min. Fig. 5.22 shows the field dependence of specific magnetization for amorphous as-quenched and thermally treated nanocrystalline samples measured by VSM. It can be seen that with increasing annealing temperature shows magnetization increases until T_a =525°C. The maximum in saturation magnetization is reached at the early stage of nanocrystallization. An increase of M_s for the annealed samples at 400°C and 450°C compared with the amorphous state is due to the structural relaxation and changing the degree of chemical disorder of the amorphous state. The increase in M_s is evidently caused by the irreversible relaxation. The saturation magnetization are shown in Table-5.3. Note that an increase in M_s due to structural relaxation has also been detected in Fe-based glasses [5.12]. A rapidly decrease in M_s has been observed with increasing annealing temperature at 550°C. The possible reason for this decrease in M_s may be attributed to the enrichment of bcc Fe(Si) nanograins with Si

resulting in a decrease of Fe magnetic moment due to the change of local magnetic environment.

The irreversible structural relaxation in amorphous materials can be satisfactorily interpreted in terms of annihilation of compressed for p-type defects and stretched for n-type defects regions [5.13], where the later process dominates, resulting in a slightly more compact structure. The atomic volumes of Fe atoms in the p-type defects become greater during annihilation leading to the increase of their magnetic moments whereas the contrary occurs to the Fe atoms in the n-type defects. When the nanocrystallized fraction reaches detectability, the magnetization decreases. The Fe-moment decrease with annealing can be interpreted by the continuous Si diffusion into the bcc grains as well as the ordering of the Fe(Si) phase as the isothermal annealed proceeds. This diffusion results in the enrichment of Si in the nanograins. The redistribution of Si atoms requires diffusion at least over a 20nm distance. This new distribution will be completed only after formation of the bcc nanograins. Therefore, the role of the dissolved Si becomes dominant in lowering the M_s only during more prolonged nanocrystallization annealed. As nanocrystallization proceeds, the influence of Nb enrichment in the amorphous matrix on reducing M_s cannot be excluded either.

Table-5.3

The values of saturation magnetization of $Fe_{73.5}Nb_3Cu_1Si_{13.5}B_9$ alloys at different annealing temperature with annealing time 30 minutes

annealing temperature,T_a (°C)	saturation magnetization (emu/g)
as cast	132.2
400°	135.6
450°	138
525°	140.6
550°	131

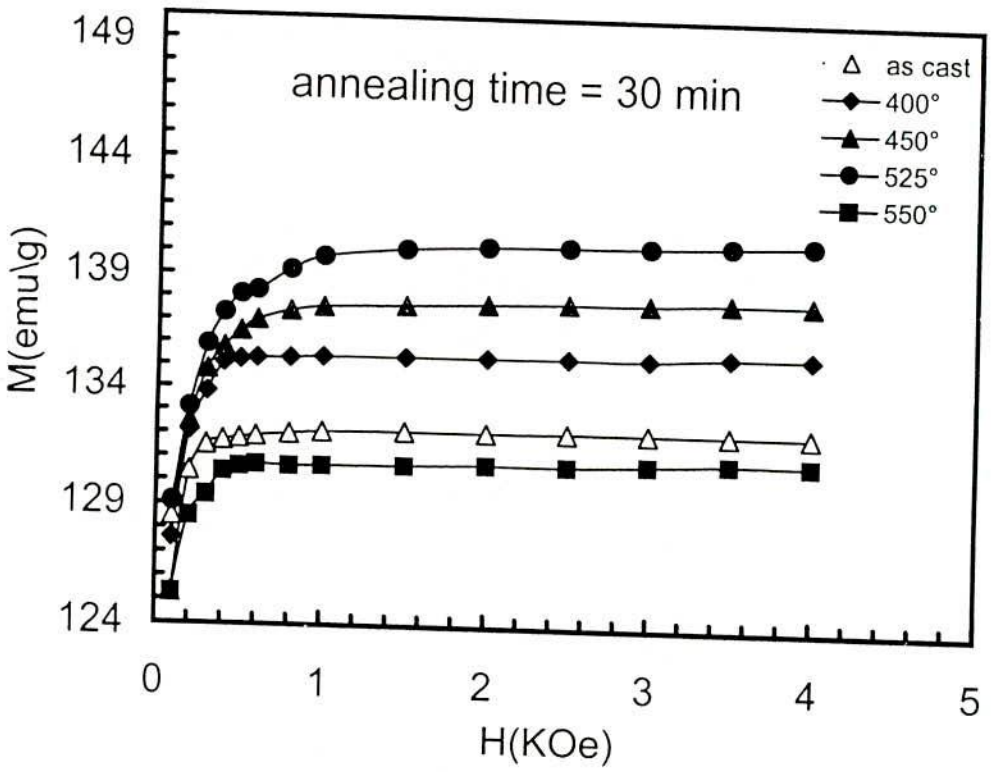

Fig. 5.22 Specific Magnetization versus magnetic field of as-cast and annealed samples of $Fe_{73.5}Cu_1Nb_3Si_{13.5}B_9$ alloys

5.4.2 Temperature Dependence of Magnetization Amorphous $Fe_{73.5}Nb_3Cu_1Si_{13.5}B_9$ Ribbon

Temperature dependence of magnetization of the Amorphous $Fe_{73.5}Nb_3Cu_1Si_{13.5}B_9$ specimens measured by V.S.M. from room temperature to 725°C is shown in fig. 5.23. The sample temperature was swept with a rate of 30°C/min. The main features are as follows:

1) a sharp fall of M_s where $\frac{dM}{dT}$ is maximum is around 330°C and corresponds to ferro-paramagnetic transition of the amorphous phase;

2) an increase of saturation magnetization at the crystallization onset, around 520°C, that corresponds to Fe(Si) ferromagnetic nano phase forming in the paramagnetic amorphous matrix, and

3) a new sharp fall in saturation magnetization (M_s), around 600°C, is associated with the ferro-paramagnetic transition of the Fe(Si) nanophase.

An enhancement of the T_c of the amorphous phase with the increasing of the volume fraction of the nanophase is observed, as a consequence of the decrease of the Fe/B ratio in the amorphous residual matrix when the Fe-Si nanophase forms. Above T_c^{amor}, ferromagnetic nanocrystaline particles exist within a paramagnetic amorphous matrix. If the size of the nanocrystals is small enough and the intergranular matrix is sufficiently thick to minimize the magnetic interaction between them, then super paramagnetic behavior of the essemble of nanocrystalline particles is expected [5.14]. This results in magnetic ordering of the particles at the temperature above T_c^{amor}. An analysis of particle ordering process in systems in which the magnetic coupling between particles prevents superparamagnetic relaxation. However, as the ordering temperature is rather high, it seems that the magnetic interaction between crystallites is strong, so the exchange contribution can be significant.

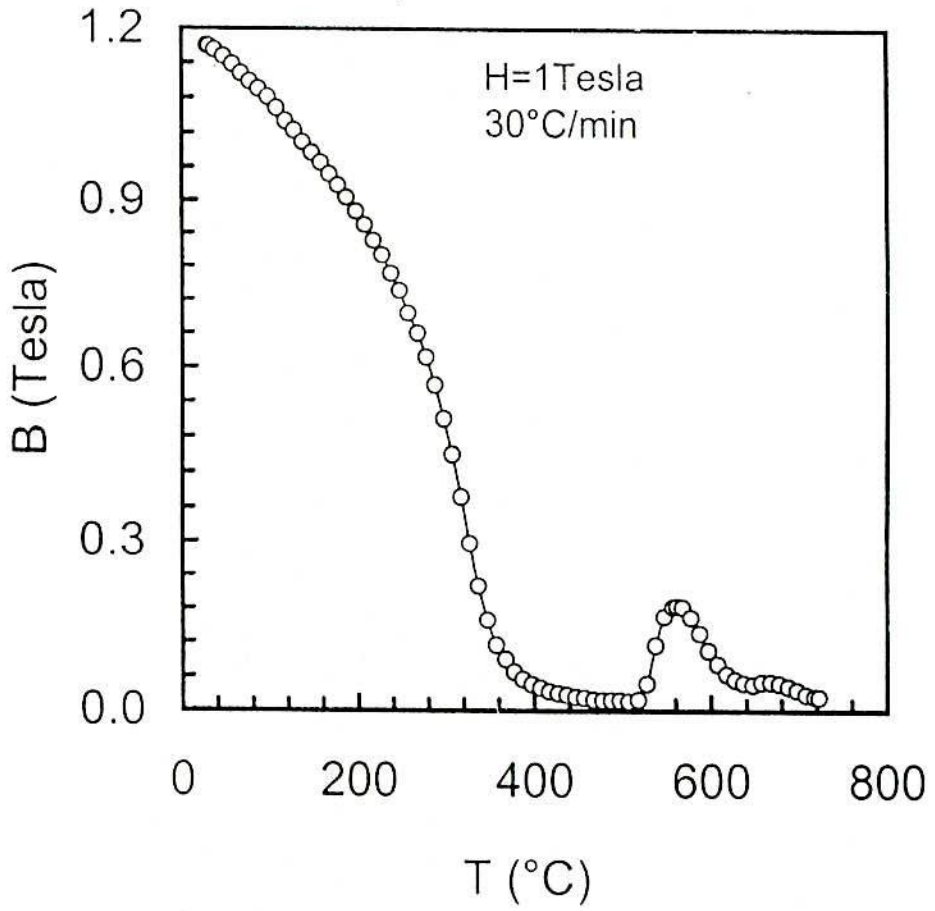

Fig. 5.23 Temperature dependence of Magnetization of nanocrystalline amorphous ribbon with composition $Fe_{73.5}Cu_1Nb_3Si_{13.5}B_9$ alloys

Chapter-6

Conclusions

6.1 Conclusions

Nanocrystalline Fe-based alloys combine the advantageous properties of various soft magnetic materials, i.e., the high saturation induction of Fe-based alloys, the high permeability and low magnetostriction of permalloys or amorphous Co-based alloys with favorable high frequency behavior. Nanocrystalline alloy as thin as 20-22μm in the amorphous state can be prepared by melt spining technique. The evolution of ultrasoft magnetic properties of $Fe_{73.5}Cu_1Nb_3Si_{13.5}B_9$ upon annealing is well correlated with the evolution of microstructural components. Nanocrystalline structures offer an interesting new possibility for tailoring good soft magnetic properties. The presence of 1% of Cu and 3% Nb additions in Fe-Si-B alloy changes the crystallization process considerably. After heating above its crystallization temperature, α-Fe(Si) nanometric crystallites with average grain size of 5-20nm grow in the amorphous matrix. The average grain size 10-13 nm, is much smaller than that of grains usually obtained by crystallizating conventional metallic glasses (100-1000nm). Fe-rich nanocrystalline state, composed of α-Fe(Si) fine grain structure resulting in a significant improvement of permeability by two orders of magnitude compared with the amorphous precursors. The improvement of magnetic properties with increase of annealing temperature is mainly connected with the microstructure i.e with the creation of fine randomly oriented bcc Fe(Si) grains of 10 to 13 nm in the residual amorphous matrix. The increase of the permeability with increasing annealing temperature is connected with more effective averaging out of the magnetocrystalline anisotropy due to the increase of the nanocrystalline phase with nanometric grains of approximately ≈ 10nm as well as decrease of the magnetostriction constant.

We have investigated the conditions for magnetic softening upon partially crystallizing heat treatment of a Finemet alloy with the composition $Fe_{73.5}Cu_1Nb_3Si_{13.5}B_9$. The crystallization in $Fe_{73.5}Cu_1Nb_3Si_{13.5}B_9$ is achieved in a two step process. The first DTA peak at 542°C corresponds to the precipitation of an ordered bcc α-Fe(Si) solid solution embedded in an amorphous phase, and the second one to the crystallization of Fe-B

compounds. At 686°C it is found that the second DTA peak seems merge with a new peak, corresponding to 726°C. The effect of a two-step annealing process on the soft magnetic properties and the microstructure of $Fe_{73.5}Cu_1Nb_3Si_{13.5}B_9$ alloy have been investigated. The two-step annealing process consists of a low temperature preannealing of 400°C and 425°C much below the crystallization onset temperature corresponding to the first peak of the DTA thermogram and a subsequent high temperature annealing for the optimum crystallization of the Fe(Si) phase. When the alloy has been preannealed at 425°C for 30 minutes and subsequently annealed at 545°C for 30 minutes; the soft magnetic properties finally obtained were considerably improved with increasing preannealing time. The improvement in the soft magnetic properties can be ascribed to the much refined grain structure obtained at temperature annealing conditions. When the alloy has been annealed for one hour at various temperatures, the maximum initial permeability (μ') were observed at T_a = 560°C. As a consequence, the two-step annealing process is found to be very effective in refining the α-Fe(Si) grain structure and in improving the soft magnetic properties of $Fe_{73.5}Cu_1Nb_3Si_{13.5}B_9$ alloy. The amount of nanocrystalline phase formed during one hour optimizing annealing at 555°C, in which magnetic initial permeability reaches the maximum value, depends on the annealing time. The greatest advantage of nanostructured magnetic material lies in the freedom of tailoring its magnetic softness and hardness depending on annealing temperature and time.

The saturation magnetization for nanocrystalline samples has slightly increased for annealing at temperature around the onset of crystallization. When annealed at higher temperature at which complete crystallization takes place, magnetization decreases again. When the annealing temperature is increased above 560°C this leads to deterioration in the magnetic softness, possibly due to the precipitation of the Fe_2B phase which causes a magnetic hardening because of the weakening of intergranular magnetic coupling and substantial increase of magnetocrystalline energy. The best magnetic properties are observed when the annealing temperature is close to 555°C. This temperature corresponds to a maximum initial permeability and to the lowest high frequency losses. It has been found that the relative initial permeability at 1kHz increases from 10,000 to 22,000 with increasing

annealing temperature. The magnetic properties of nanocrystalline materials are superior to those of its amorphous alloy.

There is much scope for further research on controlling the magnetic characteristics by changing composition and heat treatment. The magnetic permeability, saturation magnetization, Curie temperature, magnetic anisotropy, magnetization and coercivity are all controllable by choosing appropriate composition, selecting the temperature and duration of the heat treatment. Further work with finer variation of composition can be useful in detailing out the effect of nanograin forming material on magnetic characteristics. Certain important parameters like magnetic anisotropy and magnetostriction need to be studied in detail for their variations with annealing temperature.

Bibliography

Chapter-1

1.1. A lovas, L. F. Kiss. Varga, P. Kamasa, I. Balogh, I. Bakonyi; J. phys. 1V J. Inst. Met. France; 8(1998) 291.

1.2. G. Herzer; IEEE Trans. Mag 26; 1397 (1990).

1.3. A. Hernoado, M. Vazquez, T. Kulik and C. Prados; Phys. Rev.B 51 (1995) 1381.

1.4. A Hernando and T. Kulik; Phys. Rev. B 49 (1994) 7064.

1.5. R. Grossinger, D . Holzer, C. Ksshach, H. Sassik, R. Sato Turtelli, J. P. Sinnecker and E. Witting; J. Magn.Magn. Mater; in press.

1.6. R. Alben, J. J. Becker & M. C. Chi; J. Appl. Phy.49 1653 (1978).

1.7. G. Hezer; IEEE Trans. Magn. 25 (1989) 3327.

1.8. T. H. Noh. M. B. Lee. H. J. Kim, I.K. Kang; J. Appl. Phys. 67 (1990) 5568.

1.9. G. Herzer, H. Warlimont; Nanostruct. Mater. I (1992). 263.

1.10. M. Vazquez, P. Marin, A. O. Olofinjana, H. A. Davies; Mater. Sci. Forum 179-181 (1995) 521.

1.11. P. Kollar, J. Fuzer, P. Maa, T. Svec, M. Konc; J. Magn. Magn. Mater. 157/ .58 (1996) 213.

1.12. T. Kulik, A. Hernando; Magn. Magn. Mater. 160 (1996) 269.

1.13. C. F. Conde, V. Franco, A Conde, inip. Duhaj, P. Mrafko, P. Svec (Eds); Rapidly Quenched and Metastable Materials, Elsevier, Amsterdam, 1997, P. 254.

1.14. A. Hernando, M. Vazquez, T. Kulik, C. Prados; Phys. Rev. B 51 (1995) 3581.

1.15. E. C. Stoner and E. P. Wohlfarth; Phil. Trans. Roy. Soc. (London), vol. A-240, pp. 599, 1948.

1.16. A. Slawska- Waniewska, M. Gutowski, H. K. Lochowicz, T. Kulik and H. Matyja; Phys. Rev. B 46 (1992) 14594.

1.17. P.Duhaj, P.Svee, D.Janickovic and I.Matko, Meterials Scinece and Engineering, A133 (1991) 398.

1.18. Y. Yoshizawa and K. Yamauchi; Maer. Res. Soc. Proc. 232 (1991) 183.

1.19. A. Hernando and T. Kulik; Phys. Rev. B 49 (1994) 7064.

1.20. Tudeusz Kulik, Antonio Hernando and Manuel Vazquez; J.Magn.Magn.Matter.; 133, pp310-313, 1994.

1.21. G. Herzer, and H. Warlimont, Nanostructured Materials, Vol. 1 (1992) pp 263.

1.22. P. Duhaj, P. Svec, D. Jamoclpvic, I. Mako and M. Hlasnik, Mat. Sci. Eng. B 14 (1992) pp 357.

1.23. Le Minh, Bach Thanh Cong, Tran Quoc An and Nguyen Chau; Proceeding of the 2nd. International Workshop on Materials Science (IWOMS'95), Hanoi, Oct.1995.

1.24. E. Estevez Rams, J. Fidler, M. Dahlgren, R. Grössinger, M. Knobel, P. Tiberto, P. Allia and F. Vinal; J.Phys.D: Appl. Phys. 29(1996) 848-854.

1.25. S. S. Sikder & M. A. Asgar; Thermochica Acta., vol. 326, pp. 119-126, 1999.

1.26. M. A. Asgar & S. S. Sikder; Indian J. Phys., vol. 73a(4), pp. 1-10; 1999.

Chapter-2

2.1. Yoshizawa, Y. , S. Oguma and K. Yamauchi; 1988, J. Appl. Phys. 64, 6044.

2.2 Hasegawa, R., V. R. V. Ramanan and G. E. Fish; 1982, J. Appl. Phys. 53, 2276.

2.3. Herzer, G. , and H. R. Hilzinger; 1986, J. Magn. Mang. Mater. 62, 143

2.4. Alben, R. , J. J Becker and M. C. Chi ; 1978, J. Appl. Phys. 49, 1653.

2.5 T. Mizoguchi ; IBM Research Report , Rc 6054, 1976.

2.6. R. Alben, J. I. Budnick & G. S. Gargill ; α_{III} Metalic Glasses ", American SOC. for Metals , pp. 304, 1978.

2.7. Yoshizawa , y . and K .Yamauchi ; 1990a , Mater . Trans . JIM 31, 307 .

3.10. Hitachi Metals Ltd ., 1993, New materials from the nano-world, Magnetic cores, Data sheet Y- 930415.

3.11. Vacuumschmelze Gmbit, 1993, Toroidal cores of VITROPERM, Data Sheet PW-014.

3.12. J.T.S. Irvise, E, Amano, A. Huanosta, R. Valenzuela and A. R. Wesf; Solid State Ionies 40/ 41, 220, (1990)

3.13. E. Amano, R. Valenzuela , J. T. S. Irivne and A. R .West ; J . Appl . Phys . 67, 5589 (1990)

3.14. J. T. S Irvine, E. Amano and R. Valenzuela; Matewer. Sci. Eng. A133, 140 (1991)

3.15. Bozorth , R; 1951 Ferromagnetism (D .Van Nostrand ,princeton N .J .) p. 76 .

3.16. Kupfmulle, K; 1990 , Einfxhrng in die theoretische Elektrotechnik

(Springerver lag, Berlin) P. 314.

3.17. Haris, R., M. Phischke and M. J. Zuchermar; Phys. Rev .Lett ., vol. 31, pp. 160,1973.

3.18. Handrich , K.; Phys .Stat .Sol .(b) , vol . 53, pp. k17, 1972 .

3.19. Keffer , F . ; In Ferromagnetism , ed . H .P .J . Wijn (Springer, Berlin), vol XVIII .2, pp.1, 1966

3.20. Harris, R., M . plisehke and M .J. Zuckorman ; Phys Rev . Lett ., vol . 31, pp . 160, 1973.

Chapter-4

4.1. Chatelier, H. Le.; Bull SOC . Franc . Mineral, vol. 10, pp. 204, 1887.

4.2. W. B. Pearson; A Handbook of lattice spacings and Structures of Metals and Alloys (Oxford: Pergamon) 1958.

4.3. M.A. Mazid and M.A. Chowdhury; " Design and construction of a former type vibration sample magnetometer", AECD/MMD/1, June 1986(Bangladesh).

4.4. S. Forner; Rev . Sci. Instr. vol. 27, pp. 548, 1956.

Chapter-5

5.1. C. L. Chen and R. S. Hasegwa; ibid, vol. 49, pp. 1721, 1978.

5.2. K. Moorjani, S. K. Chatak, K. V. Rao, B. Kramer and H. S. Chen; Int. Conf. on Liquid and Amorphous Metals, Grenomle, France, 1980.

5.3. M. A. Willard *et. al.*; J. Appl. Phys., vol. 85, No. 8, April 1999.

5.4. Y.Yoshizawa, S. Oguma, K. Yamachi; J. Appl. Phys. 64, 6044, (1988);Y.Yoshizawa and K. Yamauchi, Mat. Sci. and Engg., A133, 176-179 (1991).

5.5. M. Rubinstein, V. G. Harris, P. Lubitz; J. Magn. Magn. Mat. 234 30(2001).

5.6. P. Allia, M. Baricco, M. Knobel, P. Tiherto and. Vanai; J. Magn. Magn. Mater. 133(1994) 243

5.7. M. Dahlgren, R. Grossiger, M. Knobel, H. Sassik, P. Tiberto and G. Wiesinger; EMMA. Conference, 1995, Vienna, Austria.

5.8. K. Brozozka, A. Slawska- Waniewska *et al.* ; IEEE, Trans. Mag. 29 (1993) 2628.

5.9. M. Knobel, J. P. Sinnecker *et al.*; J. Magn. Magn. Mat. 133 (1994) 255.

5.10. J. Zbroszczyk, J. Olszewki, W. Cirzynska & K. Naria; J. Mag. Mag. Maer 140-144 (1995) 445.

5.11. F.E. Luborsky; Amorphous Maeallic Alloys, ed. F. E. Luborsky, Buterworth, London, 1983, p.360.

5.12 A.E. Berkowitz, J. L. walter & K. f. Wall; Phys. Rev. Le. 46(1681) 1484.

5.13. D. Srolovitz, T. Egami & V. Vitek; Phys. Rev. B 24 (1981) 6936.

5.14. A. Slawska-Waniewska, M. Gutowski, H. Lachowicz, T. Kulik & H. Matyja; Phys. Rev. B. 46 (1992) 14594.